Numerical Schemes and Well-Posedness in Nonlinear Aeroelasticity

Ralf Massjung

Numerical Schemes and Well-Posedness in Nonlinear Aeroelasticity

Von der Fakultät für Mathematik, Informatik
und Naturwissenschaften
der Rheinisch-Westfälischen Technischen Hochschule Aachen
zur Erlangung des akademischen Grades eines
Doktors der Naturwissenschaften
genehmigte Dissertation

vorgelegt von

Diplom–Mathematiker Ralf Massjung

aus Rastatt

Berichter: Universitätsprofessor Dr. Wolfgang Dahmen
Universitätsprofessor Dr. Josef Ballmann

Tag der mündlichen Prüfung: 28. August 2002

Diese Dissertation ist auf den Internetseiten
der Hochschulbibliothek online verfügbar.

Acknowledgements

This thesis is a result of a project I worked on in the *Sonderforschungsbereich 401* ”*Strömungsbeeinflussung und Strömungs–Struktur–Wechselwirkung an Tragflügeln*” at the *RWTH Aachen* from 1997 to 2002. During that period I held a position at the *Institut für Geometrie und Praktische Mathematik*. I want to thank my project coordinators Prof. Dr. Josef Ballmann and Prof. Dr. Wolfgang Dahmen for supporting my ideas throughout this period. Further, I'm deeply grateful to Volker Elling, for his commitment to the project in the course of his Diplom thesis, implementing a lot and checking numerous possibilities in the first half of the code development. A thanks goes also to my colleagues for their help and understanding, to mention a few, Dr. Volker Reichelt for support when struggling with computers, Frank Bramkamp for CFD-discussions, and my project fellow Dr. Jörg Hurka for the good collaboration and many good laughs.

Contents

1 Introduction **1**

1.1 Panel flutter, aircraft wing flutter and nonlinearities . . . 2
1.2 Two simple aeroelastic problems . . . 4
  1.2.1 A square prism in incompressible flow . . . 5
  1.2.2 Supersonic panel flutter . . . 6
1.3 Computational Aeroelasticity . . . 9
1.4 Aims, achievements and chapter guide . . . 12

2 The Continuous Problem **15**

2.1 Panel flutter . . . 15
  2.1.1 Fluid . . . 15
    2.1.1.1 Moving impermeable boundaries . . . 16
    2.1.1.2 Restriction to a finite domain . . . 16
  2.1.2 Structure . . . 17
  2.1.3 Fluid–structure interaction . . . 18
2.2 Dimensionless equations . . . 19
2.3 Energy considerations . . . 20
2.4 Parameter space . . . 21

3 On Well-Posedness of an Aeroelastic Problem **25**

3.1 The IBVP . . . 29
3.2 A uniqueness theorem . . . 30

4 The Discrete Equations **43**

4.1 Finite Volume Discretization on moving grids . . . 43
  4.1.1 The finite volume approach . . . 43
  4.1.2 Grid movement and cells with polygonal boundaries . . . 44
  4.1.3 The Geometric Conservation Law (GCL) . . . 45
  4.1.4 The numerical flux . . . 47
  4.1.5 General representation of numerical fluxes over moving edges . . . 48
    4.1.5.1 Rotational invariance . . . 49
    4.1.5.2 Galilean invariance . . . 49
  4.1.6 The numerical flux at impermeable and artificial boundaries . . . 51

4.1.7 Linear reconstruction and limiter 51
4.1.7.1 Modification at impermeable boundaries 52
4.2 FEM for the von–Kármán panel 54
4.3 Coupling schemes 56
4.4 Energy transfer on the discrete level 59
4.4.1 Connectivity 59
4.4.2 Load transfer 59
4.4.3 Construction of a scheme with correct energy transfer 60

5 The Solution Algorithm **65**
5.1 Newton–GMRes for the discrete fluid system 65
5.1.1 Iterating with low and high order spacial resolution 67
5.1.2 Preconditioning 67
5.2 Newton–GMRes for the discrete structural system 69
5.3 Newton–GMRes for the discrete fluid-structure system 69
5.4 Convergence criterion for tight coupling 70

6 Numerical Experiments **71**
6.1 Parameters of numerical schemes 72
6.2 Typical computations and convergence in Δt 75
6.2.1 Transonic flutter at $M_\infty = 1$ 76
6.2.2 Supersonic flutter at $M_\infty = 1.2$ 78
6.2.3 Supersonic flutter near the stability boundary 82
6.3 Convergence of tight coupling algorithms 87
6.3.1 Supersonic flutter 88
6.3.2 Transonic flutter at $M_\infty = 0.95$ 88
6.3.3 Transonic flutter at $M_\infty = 1$ 90
6.4 Bifurcations depending on coupling schemes 90
6.4.1 A bifurcation at $M_\infty = 1$ 96
6.4.2 A bifurcation at $M_\infty = 0.95$ 96
6.5 Stability chart 96

7 Summary **103**

Chapter 1

Introduction

Summary

This thesis considers the *panel–$flutter$–problem* to study issues of numerical schemes and well–posedness that appear in aeroelastic models. Apart from its own relevance concerning the stable performance of aircraft skin, panel–flutter is a valuable model problem of aeroelasticity showing phenomena similar to those observed at aircraft wings.

Simulating numerically the time–dependent processes of aeroelastic systems becomes an increasingly important tool in designing elastic structures such that they can savely be exposed to interaction with environmental fluid flows. The possible conditions under which the structure has to perform have to lie in the stable regime of the fluid–structure system.

Mathematically, time–dependent processes are formulated as initial boundary value problems (IBVP). In the present application two continuum fields are involved, the fluid and the structure and at their interface coupling conditions have to be posed. The most important mathematical properties of an IBVP are those concerning its well–posedness. Here an IBVP is formulated, describing a clamped plate which is in contact over the whole of its top side with a given amount of fluid material. A function space is given in which only one solution to the IBVP can exist. This uniqueness theorem is proven using as the fluid model the compressible Navier–Stokes equations (in Lagrangian coordinates) and as the structural model a variant of the von–Kármán plate equation. The theorem is a short time statement allowing large data. Since the proof uses the energy method it also contains stability estimates to some extent. The question of the existence of a solution is still open.

When simulating an aeroelastic process, typically existing fluid and structure codes are called by a master program to advance the separate media in time. A time–step–wise decoupling of the fluid–structure–equations underlies these methods. This is a very economic approach, but one has to be aware of possibly having lost something through the decoupling procedure. Additional stability restrictions and loss of the time integration order present in the separate fluid and structure codes may result, as one violates on the discrete level such important properties as the correct energy transfer between fluid and structure. Further, the underlying physical stability problem of detecting bifurcations of the aeroelastic system in parameter space may lead to a confusion of numerical and physical instabilities or at least poses the question, how sharp the bifurcations can be caught by the decoupling strategies.

In contrast to these decoupling strategies, here we have implemented a matrix–free Newton–GMRes iteration on the coupled set of discrete fluid–structure equations to achieve a so–called *tight coupling*. It is compared with other schemes, in particular with a fixed–point–iteration, that tries to achieve a tight coupling by iterating between the decoupled codes within each time step. The implementation solves the panel flutter problem modelled with the 2D Euler equations of gas dynamics and a strip of the von–Kármán plate.

Furthermore, we have constructed a scheme that guarantees a correct energy transfer between fluid and structure on the discrete level. It is implicit in time over the coupled fluid–structure system. Using the common finite element discretizations for the structure and finite volume methods on polygonal cells for the fluid, the scheme combines the time integration scheme, the load transfer from fluid to structure and the fluid boundary movement due to structural deflections such that the correct energy transfer is given. Its residual may be diminished by the matrix–free Newton–GMRes within in each time step.

The following sections of this introductory chapter put the work presented in the later chapters in a broader context: First we discuss physical and modelling issues of panel flutter and the relevance of panel flutter as a valuable model problem for aeroelasticity. Then we give two very simple aeroelastic models to envision the appearance of aeroelastic instabilities. Further, the methodologies of Computational Aeroelasticity used to simulate aeroelastic processes with tools from Computational Fluid Dynamics and Computational Structural Dynamics are discussed, stressing the issues relevant to this thesis. Finally, we state the aims and achievements of the thesis and give a guide to the following Chapters.

1.1 Panel flutter, aircraft wing flutter and nonlinearities

The panel flutter problem consists of a clamped or simply supported plate (*panel*) over which a compressible fluid (air) flows. Here we reduce the space dimensions by one, assuming the panel to be long in direction perpendicular to the inflow. More precisely, we assume constant behaviour in the direction of the long panel side (spanwise direction), so that a 2D flow passes over a strip of the plate, which is clamped or simply supported at the leading and the trailing edge, compare Fig. 1.1. Disturbing the panel with an impulse, the fluid–structure–interaction is triggered and in the long time behaviour this system may fall into a time periodic oscillation with *large* amplitudes, called *flutter*. Other observed long time behaviours are a steady state with either deflected panel (*divergence*) or an undeflected panel (*damped* or *stable* behaviour). These phenomena can also be found in the aeroelastic behaviour of aircraft wings. Further, both aeroelastic systems exhibit a *transonic dip*. This means that the dynamic pressure (kinetic energy of the inflow) needed to obtain unstable behaviour (flutter or divergence) drops considerably to a minimum at an inflow Mach number near unity. Another common feature of panel flutter and wing flutter is that shock movements play a significant role in the unstable mechanisms when the flow is transonic [4], [14].

Thus, panel flutter can serve as an important model with a simple 2D flow geometry to study numerical schemes for aeroelasticity, which have become an important tool in designing aircrafts [20]. The major aeroelastic design criterion is to avoid unstable behaviour, which may be destructive or lead to long time failure due to material fatigue. The aircraft design has to ensure that the aircraft operates considerably away from its aeroelastically unstable regime.

If one wants to observe the unstable phenomena, which exhibit large structural deflections, one has to take these into account in the panel model. This can be done by employing the von–Kármán plate model in its 1D variant, as done by Dowell [18], who combined it with simple aerodynamic models to describe panel flutter. In particular, in the 1D von–Kármán model a third order nonlinearity is present, which is typical for a large class of structural nonlinearities appearing in aeroelastic problems [41]. The nonlinearity activates a restoring force when the panel is stretched due to large deflections.

The activation of nonlinearities either in the structure or in the fluid or in both media causes the appearance of *limit cycle oscillations*. In general dynamical systems, limit cycle oscillations typically appear when nonlinearities become significant at large amplitudes, preventing the infinite growth in amplitudes that is predicted by corresponding linear models [48].

Being interested in the transonic regimes, one has to resolve nonlinearities governing the flow field around shocks. As long as flow separation is not present, shocks are very well captured by inviscid flow models. In the steady transonic case, the resolution of these nonlinearities, employing the Euler equations is exhibited in [31], comparisons with reduced models and experimental data are also made. In our unsteady case, the need to employ nonlinear flow models, associated with the presence of shocks, arises as follows. In the unsteady case, the *reduced frequency* $k = \omega\, l / 2\, u_\infty$ is an important similarity parameter, where ω is the frequency of an obstacle in the fluid oscillating in one degree of freedom. Here l is a typical length scale of the problem and u_∞ the inflow velocity, as for example in Fig. 1.1. Experimental results of an airfoil section oscillating in pitch in transonic flow are presented in [62]. It is shown that at quasi–steady situations up to moderate reduced frequencies, the nonlinear effects of unsteady transonic flow are fully developed with the largest amplitudes in shock motion. In particular, this range includes the range of interest for flutter phenomena ($k \lesssim 0.5$). For sufficiently high reduced frequencies, the flow behaviour becomes linear. The *phase lag* between the shock motions and the motion of the airfoil, which increases with k is also discussed in [62]. In a case measured in [4] it already reaches its maximum value at $k = 0.5$. This phase lag is attributed to play an important role in the meachanisms of transonic flutter [4]. Already at low k, the influence of the phase lag is reported to be significant. As an

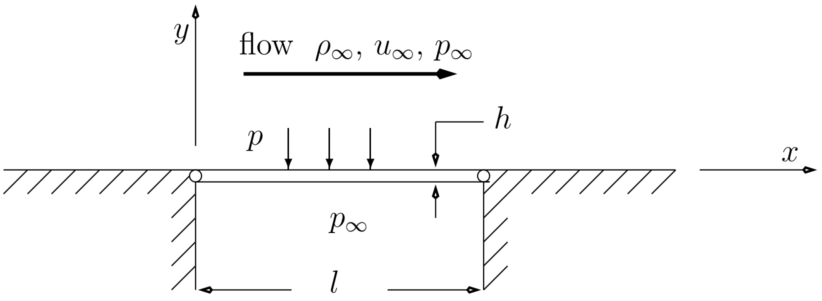

Figure 1.1: Geometry of the 2D panel–flutter–problem.

example, for the panel flutter problem, a reduced frequency of 0.015 was identified for a transonic flutter case in [27]. In [35] airfoil flutter was studied and the differences between the nonlinear transonic small disturbance equations as flow model and a linear aerodynamic model was seen to be severe, as the linear model even misses to indicate the existence of the transonic dip. [2] airfoil flutter is treated using the Euler equations as flow model and the authors say that an accurate prediction of the phase lag cannot be assured with a transonic small disturbance model, and clearly the validity of a small disturbance model degrades compared to the Euler equations when thickness effects are pronounced. Modelling panel–flutter with the von–Kármán and the Euler equations was introduced in [14].

Flow separation was already mentioned above. It can create another important nonlinear aerodynamic effect that can only be captured with a viscous flow model. Due to shock–boundary–layer interaction or high angles of attack the flow may separate. In particular, structural vibrations may cause the flow to alternately separate and reattach, a highly nonlinear process, which creates highly unsteady aerodynamic loads on the structure, and the interplay leads to very challenging aeroelastic phenomena [20].

1.2 Two simple aeroelastic problems

We want to illustrate some elementary features of aeroelastic problems with two simple examples. In these examples only one, respectively two, degrees of freedom suffice to obtain dynamic aeroelastic instabilities. Three common causes of aeroelastic instabilities are aerodynamic forces that induce a *negative damping* for the structure (Sec. 1.2.1), the aerodynamic *coupling of* structural *modes* (Sec. 1.2.2) and the *resonance* of unsteady periodic aerodynamic phenomena with natural frequencies of the structure.

The last case may occur when the shape of the structure can create a time periodic flow field. E.g. assuming the structure as rigid and fixed in space, a flow passing it may shed vortices periodically, inducing periodic forces on the structure. If the natural frequency of the structure and the shedding frequency coincide, we have a resonance that causes the structural motions to grow. Such examples can be found in [9]. Let us mention the most famous aeroelastic catastrophe, the failure of the Tacoma Narrows Bridge, which is mainly attributed to vortex resonance [9]. One day in 1940 this suspension bridge started

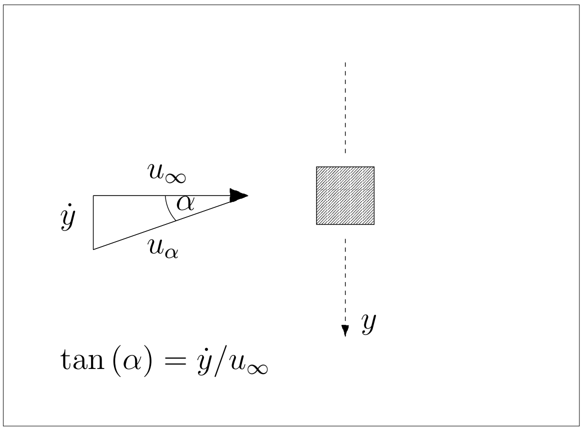

Figure 1.2: Prism in wind

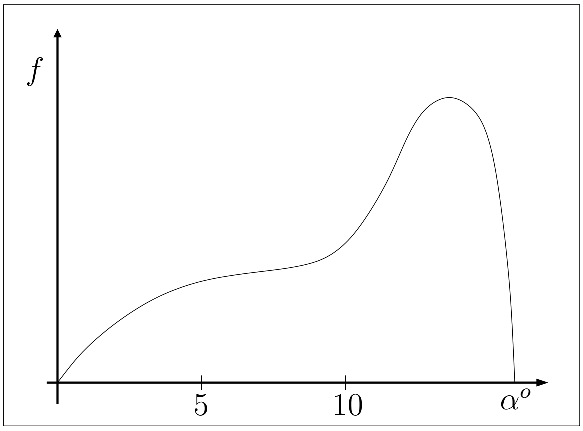

Figure 1.3: Steady aerodynamic forces

oscillating when a wind of 42 miles per hours blew against it and it finally broke after 30 minutes of violently growing motions [25].

In any case, structural (Sec. 1.2.2) or aerodynamic (Sec. 1.2.1) nonlinearities may cause the structural motions to be finite in the unstable aeroelastic regime, so that limit cycle oscillations are observed. These oscillations are *self–excited* ones, since no excitation oscillation is imposed from outside the aeroelastic system, in particular not from the incoming flow.

1.2.1 A square prism in incompressible flow

Let us look at a long undeformable straight rod with a square cross-section. Let it be directed along the z–axis and let us look at its cross-section in the xy–plane. Let the rod have mass m and only one degree of freedom, namely to move into y–direction and let its suspension be subject to a (linear) stiffness and a (linear) friction force. Further let a constant wind of velocity u_∞, directed into x–direction, blow against the rod; compare the sketched situation in Fig. 1.2.

Modelling this situation with stiffness k and friction r and a quasi–steady approach to obtain the force of the wind onto the rod, we obtain the equation

$$m\,\ddot y \;+\; r\,\dot y \;+\; k\,y \;=\; f(\dot y/u_\infty)\,.$$

From a quasi–steady point of view, the forces $f(\dot y/u_\infty)$ induced by the wind, depend on the wind velocity relative to the rod, which can be determined from a measurement with a fixed rod in a wind of velocity u_α and angle of attack α, compare Fig. 1.2. The sensitivity with regard to Reynolds number is reported to be small in the considered range [50], so that the exclusive dependence of f on $\dot y/u_\infty$ is reasonable. In [50] conditions for the validity of the quasi–steady approach are given. From a set of measurements the relation $f(\dot y/u_\infty)$ may be fitted. In Fig. 1.3 the qualitative form of a *good* fit of the measurements made in [50] is shown.

In any case, the simplest fit, valid only for a limited range of rod movements, is the linear one, $f(\dot{y}/u_\infty) \approx c\,\dot{y}$. This allows an immediate stability analysis for the system:

$$m\,\ddot{y} + (r - c)\,\dot{y} + k\,y = 0 \quad \text{has} \begin{cases} \text{infinitely growing solutions for} & r - c < 0 \\ \text{damped solutions for} & r - c > 0 \end{cases}$$

We see that the aerodynamic forces may induce a negative damping for the structure. Recasting the above in the aerodynamicist's terminology, introducing the steady lift and drag forces in terms of the coefficients C_L, C_D,

$$F_L(\alpha) = \frac{1}{2}\rho_\infty\, u_\infty\, A\, C_L(\alpha)\,, \quad F_D(\alpha) = \frac{1}{2}\rho_\infty\, u_\infty\, A\, C_D(\alpha)\,,$$

where A is the area of a long side of the rod, the linear aerodynamic model is given by [9]

$$c = -\frac{1}{2}\rho_\infty\, u_\infty\, A \left(\frac{\partial C_L}{\partial \alpha} + C_D \right) \Big|_{\alpha=0} .$$

Thus the system is definitely stable for

$$\left(\frac{\partial C_L}{\partial \alpha} + C_D \right) \Big|_{\alpha=0} > 0$$

and the critical wind velocity for unstable behaviour is

$$u_\infty^{crit} = -\frac{2\,r}{\rho_\infty\, A \left(\frac{\partial C_L}{\partial \alpha} + C_D \right) \Big|_{\alpha=0}} .$$

The linear fit captures only a single aspect of the true dynamics, it finds the onset of instability but cannot resolve the true behaviour of the system at and beyond this point, since nonlinearities are activated.

The true form of f is nonlinear, activating forces at large α that prevent an infinite growth in deflection. A fit of f with an odd polynomial of degree seven, corresponding to Fig. 1.3, captures the measurements in a wide range. Using such a nonlinear representation of f and applying the method of slowly varying amplitudes and phase angles, the appearances of limit cycles and their basins of attraction in phase space could be determined in [50]. This reveals the stability behaviour found in the experiments of [50], with a very accurate coincidence in amplitudes and bifurcation points. The amplitudes $\overline{y}$ of the limit cycles appearing at a given u_∞ are shown in Fig. 1.4 which is qualitatively reproduced from [50]. At some values of u_∞ three limit cycles appear. Two of these are stable and the one corresponding to the dotted line section is unstable.

1.2.2 Supersonic panel flutter

A reasonable aeroelastic model with a nonlinear structural behaviour and linear aerodynamic loads is given by the panel flutter problem when the flow is in the high supersonic

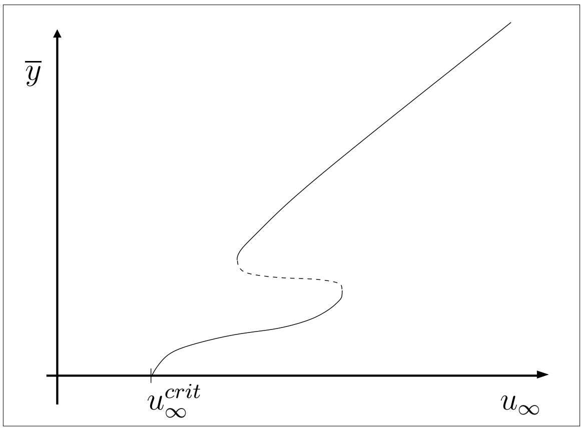

Figure 1.4: Limit cycle amplitudes

range. We let the panel be simply supported at the leading and the trailing edge. As mentioned in Sec. 1.1, the panel dynamics may be described by the von–Kármán model,

$$D\,w_{xxxx} - N\,w_{xx} + m\,w_{tt} \quad = \quad -p\ , \quad \text{with} \quad N = \frac{E\,h}{2\,l}\int_0^l w_x^2\,dx$$

where $w(t,x)$ is the panel deflection and $p(t,x)$ is the load on the panel. The material constants and panel dimensions are given by the stiffness D, the modulus of elasticity E, the panel thickness h, the panel length l, the panel mass per unit length m, compare section 2.1.2. The nonlinearity N introduces a restoring force due to the panel stretching.

If the inflow Mach number M_∞ is considerably greater than 1, a good model for the local aerodynamic loads is given by [6]

$$p \quad = \quad \frac{\rho_\infty u_\infty^2}{M_\infty}\left[w_x + \frac{1}{u_\infty}\,w_t\right] .$$

Here ρ_∞, u_∞ are the inflow density and velocity. Plugging the aerodynamic load into the above equation we have the aeroelastic model which reads in non–dimensional form (ν is the Poisson ratio, see Sec. 2.1.2)

$$w_{xxxx} \;-\; 6\,(1-\nu^2)\,w_{xx}\int_0^1 w_x^2\,dx \;+\; w_{tt} \;+\; \lambda\left[w_x + \sqrt{\frac{\mu}{M_\infty\lambda}}\,w_t\right] \quad = \quad 0\ , \qquad (1.1)$$

where we have introduced

$$\begin{aligned} \lambda &= \rho_\infty\,u_\infty^2\,l^3/(M_\infty\,D), \\ \mu &= \rho_\infty\,l/m, \end{aligned}$$

the nondimensional dynamic pressure and the mass ratio. We employ Galerkin's method, using modes that satisfy the panel boundary conditions, i.e.

$$w(t,x) \quad = \quad \sum a_n(t)\,\sin\left(n\,\pi\,x\right)$$

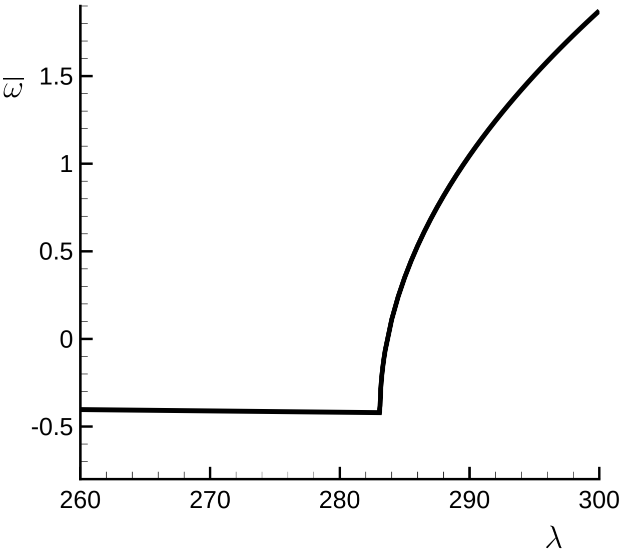

Figure 1.5: Stability at $\mu/M_\infty = 0.01$

and obtain a system of ODE's. Using *only the first* mode, we obtain an ODE for a_1, and we see that we have a positive damping coefficient and the system is always stable. Instabilities only occur, when the modes interact: Using Galerkin's Method with the *first two* modes we obtain the system

$$\begin{aligned}\frac{\pi^4}{4}\,a_1 \,+\, 3\,\pi^4\,(1-\nu^2)\,(a_1^2/2 \,+\, 2\,a_2^2)\,a_1 \,+\, 2\,\ddot{a}_1^2 \,-\, \frac{4}{3}\,\lambda\,a_2 + \sqrt{\frac{\lambda\,\mu}{M_\infty}}\,\dot{a}_1 &= 0\,,\\ 8\,\pi^4\,a_2 \,+\, 12\,\pi^4\,(1-\nu^2)\,(a_1^2/2 \,+\, 2\,a_2^2)\,a_2 \,+\, 2\,\ddot{a}_2^2 \,+\, \frac{4}{3}\,\lambda\,a_1 + \sqrt{\frac{\lambda\,\mu}{M_\infty}}\,\dot{a}_2 &= 0\,.\end{aligned}$$

We see that the damping term

$$\sqrt{\frac{\lambda\,\mu}{M_\infty}}\;I\begin{pmatrix}\dot{a}_1\\ \dot{a}_2\end{pmatrix}$$

has a positive definite damping factor. The coupling term that is created by the aerodynamic loads,

$$\frac{4}{3}\lambda\begin{pmatrix}0 & -1\\ 1 & 0\end{pmatrix}\begin{pmatrix}a_1\\ a_2\end{pmatrix}\,,$$

has a *circulatory matrix factor* and is responsible for the flutter instability [60].

Looking at the linearized system $\dot{\boldsymbol{z}} = A\,\boldsymbol{z}$, with $\boldsymbol{z} \equiv (a_1, \dot{a}_1, a_2, \dot{a}_2)^T$ that is valid near $\boldsymbol{z} = 0$, from the eigenvalues of the matrix A we can see when the origin in phase space is unstable. This is the case when an eigenvalue of A has positive real part. Denoting by $\overline{\omega}$ the maximum real part of A's eigenvalues and plotting it over λ at fixed μ and M_∞, we can see at which dynamic pressure the aeroelastic system becomes unstable. This is done in

Fig. 1.5 for $\mu/M_\infty = 0.01$, and we see that the instability appears at $\lambda \approx 284$. In [19] and [15] it was shown that using the first 6 modes suffices to obtain an accurate description of the phenomena. The resulting system of ODE's was integrated numerically for various λ. It was also seen that employing only the first two modes results in a qualitatively correct picture.

Two–mode–coupling also occurs in the *classical flutter* of airfoil sections, where the plunge and the torsion mode interact [9].

1.3 Computational Aeroelasticity

As explained in Sec. 1.1, the necessity to resolve 2D or 3D nonlinear flow fields interacting with elastic structures is given. The development of the corresponding flow solvers and structural solvers have separate histories, and in each field distinct techniques have prevailed over the years. When simulating an aeroelastic process one obviously wants to use these far developed tools. This poses difficulties when trying to satisfy physical properties of the aeroelastic problem on the discrete level, in order to improve stability, accuracy and robustness characteristics of the aeroelastic scheme.

One point of imperfection is that the fluid–structure–interfaces have *non–matching* discrete representations in fluid and structure. For example, in the 2D panel–flutter–problem a finite volume fluid solver typically works with a piecewise linear representation of the (moving) boundary. Part of the fluid boundary is given by the panel deflection which is a piecewise cubic polynomial stemming from the structural Finite Element Method. Additionally the fluid typically needs a finer spacial resolution than the structure. The connectivity of fluid and structure is usually imposed at the fluid vertices, which are enforced to stick to the structure, compare Fig. 1.6. A more significant difficulty is to carry over the *time–accuracy* present in the separate fluid and structural solvers to the aeroelastic solver. The simplest and most popular way to couple fluid and structural solvers is the so called *loose coupling* which takes the fluid pressure from the beginning of the time step to advance the structure in time and then to advance the fluid due to the obtained structural movement. Obviously this scheme has only first order time accuracy due to the "lagged action" of the fluid pressure on the structure. Still one of the early successful implementations of this type is due to Guruswamy [29], where the aeroelastic behaviour of a wing–body structure in a flow modeled by the compressible Navier–Stokes equations was simulated.

Let us use some illustrative formulas for the case when an inviscid flow model is employed. We denote by p_F^n the discrete pressure distribution in the fluid code at time level n. The superscripts are always related to a time level in this section. In a high order fluid code an intermediate value $p_F^{n+1/2}$ is used in the surface force to advance the fluid from time level n to $n+1$. Let similarly $p_S^{n+1/2}$ denote the discrete load distribution that enters the structural equations. Let a projection of p_F^n onto the structural grid be denoted by $(p_F^n)_S$. Let us further introduce the structural deflection w^n, which defines a

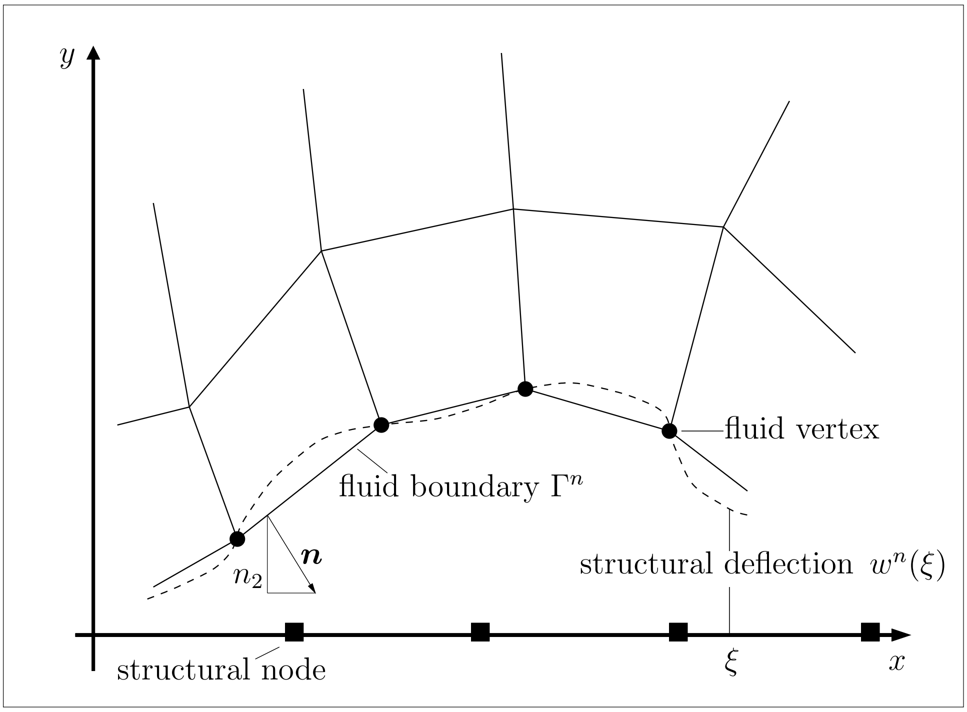

Figure 1.6: Representation of the interface in fluid and structure

fluid grid configuration $\boldsymbol{x}^n$. Let the grid velocities during the time step from level n to $n+1$ be denoted by $\dot{\boldsymbol{x}}^{n+1/2}$. In the loose coupling one sets

$$p_S^{n+1/2} \quad := \quad (p_F^n)_S \ . \tag{1.2}$$

A *conservative load transfer* for the forces in y–direction (n_2 is the normal component in this direction as indicated in Fig. 1.6 and its value is negative),

$$\int_{\Gamma^{n+1/2}} -p_F^{n+1/2}\, n_2 \; ds \quad = \quad \int_0^l p_S^{n+1/2} \; dx \ , \tag{1.3}$$

is therefore not satisfied for the loose coupling. Here $\Gamma^{n+1/2}$ is the interface belonging to the grid configuration $\boldsymbol{x}^{n+1/2}$ and associated with the time level corresponding to the pressure distribution $p_F^{n+1/2}$. Note that all formulas in this section are on the discrete level and thus in this section the integrals stand for the corresponding quadrature rules employed in the scheme.

In [11] strategies to employ global *load conservation in the projection step* are discussed, i.e. quadrature formulas are required to satisfy

$$\int_{\Gamma^n} -p_F^n\, n_2 \; ds \quad = \quad \int_0^l (p_F^n)_S \; dx \ . \tag{1.4}$$

In [11] numerical experiments were made with a loose coupling, but the time discretizations employed were not discussed. It seems that no efforts were made to satisfy (1.3).

Still, drastic improvements over projections obtained from traditional interpolation methods are found. In the corresponding examples, loads with sharp peaks are present, where interpolation violates the conservation properties immensely.

Apart from the load transfer, the *connectivity* of the two media is imposed by an exchange of discrete interface locations between fluid and structure, which additionally defines the fluid grid velocities $\dot{\boldsymbol{x}}^{n+1/2}$. The sum of all tranfers governs the energy exchange of the two media on the discrete level. Global *conservation of the energy*,

$$\int_{\Gamma^{n+1/2}} -p_F^{n+1/2}\,(\dot{\boldsymbol{x}}^{n+1/2})^T\boldsymbol{n}^{n+1/2}\;ds \quad = \quad \int_0^l p_S^{n+1/2}\,w_t^{n+1/2}\;d\xi \tag{1.5}$$

is the most important property to hold on the interface. Here, $w_t^{n+1/2}$ represents the discrete structural velocity that contributes in the energy balance. Satisfaction of (1.5) is the subject of [24], but again the discussion circumvents the time discretization. Comparisons with traditional interpolation methods brought no improvement for smooth pressure distributions and minor improvements in the presence of shocks.

Other researchers tackle an improvement of the loose coupling by iteration between fluid and structural solver to achieve converged states of higher order time discretizations at the interface, a so–called *tight coupling*. This is done in [2] and [46] without attributing properties such as (1.3) or (1.5) to the proposed schemes. Further, the actual *convergence* in each time step and comparisons with simpler coupling schemes are rarely documented. In [2] an airfoil section with plunge and pitch degree–of–freedom in transonic flow is considered. The iteration method is Jameson's dual time–stepping, where a data–transfer between fluid and structure takes place at each pseudo time step. In [46] a low Mach number flow interacting with an elastically mounted cylinder, where vortex shedding plays an important role, is simulated and considerable improvements over the loose coupling are obtained for large time step sizes. Here the iteration is a straight forward fixed–point–iteration, alternating several times between fluid and structural solver within one time step, using as data for each medium the most recent obtained in the other medium.

An entirely different approach, that relies on explicit time–integration–schemes, was proposed by Bendiksen [7]. An explicit 5–stage Runge–Kutta–Scheme was applied to the spacially discretized fluid–structure system, exchanging data at each Runge–Kutta stage. This seems to be a rather consistent treatment in time. It was applied in the transonic regime to the flutter of wing sections and to panel flutter [14], [8]. In particular it improved considerably the earlier version, where the 5–stage Runge–Kutta–Scheme was only used in the fluid and was stage–wise coupled to a separate structural code. In [7] evidence is given through numerical tests, showing that the energy transfer properties are very good, in contrast to the earlier version. The main draw back of Bendiksen's method is that it is not applicable when the time step limitations of an explicit scheme are prohibitive, as is often the case, especially in applications involving viscous flow effects.

Other strategies to improve the loose coupling are *predictions* of either the fluid state [33] or the structural state [52] by interpolating to the end of the time step, or *staggering* strategies [38] that place the time levels of one media in the middle of two consecutive time levels of the other media. An approach that drives the loose coupling even further is *subcycling* [52], where a structural time step contains several fluid time steps.

A stability analysis of a comparably simple aeroelastic problem, a 1D fluid model attached to a spring, was made in [10]. Stability limits of several coupling scheme were compared by considering the eigenvalues of the linearizations. For the problem considered, the improvements from the loose to stronger coupling schemes are clearly observed in the obtained stability limits of the schemes.

Alltogether we may group the schemes into

A Scheme with time lag (loose and subcycling),

B Schemes that aim to remove the time lag without a convergence criterion (staggered and predictions),

C Schemes that diminish the residual of the coupled system such that higher orders are achieved at the interface and hopefully a conservative energy transfer (tight coupling).

A comparison of schemes of type A and B in transonic and supersonic aeroelastic problems were conducted by Farhat and Lesoinne [23], noting that the violation of a correct energy transfer may lead to a *confusion* of *numerical instabilities* with *physical instabilities*, whereas we are interested in accurately predicting the physical instabilities. In [23], the term *partitioned schemes* is used, containig all the schemes of type A and B, further the term *monolithic schemes* is introduced, which seems to coincide with our class C.

1.4 Aims, achievements and chapter guide

The aim of the present work was to develop a scheme of type C, to observe its convergence properties and to carve out its influences on the numerical solutions in comparison with other schemes. Further, it was intended to keep the implementation most relevant for practical purposes, though not to optimize it in every respect but rather to observe its principle feasibility. Prior to the numerical work, analytical investigations to give a well–posed mathematical formulation of an aeroelastic initial boundary value problem were conducted. In the course of these studies the interest in the afore given numerical aims were motivated, especially to have on the discrete level a formulation that corresponds in significant issues to the well–posed continuous formulation. The major issue is a conservative energy transfer which, of course, is an at least equally fundamental physical property.

In Chapter 2 the continuous formulation of the 2D panel flutter problem is given, employing the 2D Euler equations interacting with a strip of a plate, where the von–Kármán plate model is used. The aeroelastic stability problem and the parameters of the problem are discussed.

A result of the work on the well–posedness is given in Chapter 3. Further related work can be found in the author's technical report [45]. A fluid–structure–interaction problem is formulated with the 3D compressible Navier–Stokes equations and a variant of the von–Kármán plate model. It is proved that it admits no more than one solution in a given function space. The proof is based on the proof of Secchi and Valli [55] on a free–boundary value problem for the flow equations and results on the plate equation from the book of Lions [39]. Similar analytical results on the fluid–structure–interaction are not known to the author.

Chapter 4 presents the discretization techniques introduced to solve numerically the problem of Chapter 2. The high–resolution finite volume method is used for the flow equations and the finite element method for the structural equations to perform the spacial discretizations. In time, classical schemes of second order are used. Since the fluid grid moves, issues like the geometric conservation law and the treatment of numerical fluxes for moving edges are discussed. In particular, a new method was developed in coordination with V. Elling, in the course of his Diplom–thesis [21], to transform an arbitrarily given numerical flux function from its formulation for fixed grids to the case of a moving grid. This makes use of the Galilean invariance of the Euler equations, see Sec. 4.1.5. Further, a multidimensional reconstruction is proposed in Sec. 4.1.7 and a technique to impose the slip condition exactly at the quadrature points of edges on impermeable boundaries, compare Sec. 4.1.7.1. The coupling schemes that have been categorized in type A, B, C above, are discussed in more detail in Sec. 4.3. In Sec. 4.4 a discretization of the coupled fluid–structure–problem with a correct energy transfer is constructed. For this purpose appropriate data transfer formulas are added to the afore developed non–matching discretizations of the separate media. In particular, this is a scheme that is implicit in time over the coupled spacially discretized fluid–structure system. This kind of construction is also not available in the literature.

In Chapter 5 the solution algorithms to diminish the residuals in the implicit time discretizations of fluid, structure and the coupled fluid–structure system are presented. In all cases a matrix–free Newton–GMRes methodology, motivated by the one for compressible flow problems in [43], [44], was implemented. The very important issue of preconditioning to obtain acceptable convergence speeds for GMRes is implemented in a decoupled fashion for fluid–structure–problems. This means that the fluid components, respectively the structural components, of the coupled fluid–structure system are preconditioned by the separate fluid, respectively structural, preconditioner. Still, the Jacobian of the coupled equations steers the iteration in the Newton steps. This new kind of algorithmic implementation of a tight coupling and its comparison with other schemes is the major achievement of the thesis. In particular, it is still in a form that can use largely independent fluid and structural codes.

The comparisons are found in Chapter 6. Here the significant numerical parameters and the numerical problems associated with physical phenomena are discussed. Coupling schemes of type A, B, C are compared. In particular, a tight coupling via a fixed–point–iteration is compared with the Newton–iteration. In Sec. 6.4 we present, how bifurcations in parameter space depend on the coupling scheme.

Chapter 2

The Continuous Problem

2.1 Panel flutter with a 1D nonlinear panel and 2D inviscid flow

2.1.1 Fluid

The balance equations for a moving domain $\Omega(t)$ in a 2D compressible inviscid flow of a perfect gas are given by

$$\frac{d}{dt}\int_{\Omega(t)} U\,dx\,dy \;+\; \int_{\partial\Omega(t)} U\,(\boldsymbol{v}-\dot{\boldsymbol{x}})^T\,\boldsymbol{n}\,ds \quad=\quad \int_{\partial\Omega(t)} \begin{pmatrix} 0 \\ -p\,n_1 \\ -p\,n_2 \\ -p\,\boldsymbol{v}^T\boldsymbol{n} \end{pmatrix} ds\;. \tag{2.1}$$

Here the conservative state vector $U = (\rho, \rho\,u, \rho\,v, \frac{1}{2}\,\rho\,|\boldsymbol{v}|^2 + \frac{p}{\gamma-1})^T$ is made up of the density ρ, the velocity vector $\boldsymbol{v} = (u,v)^T$ and the pressure p. The latter quantities give the primitive state vector $\mathcal{U} = (\rho, u, v, p)$. The only material parameter in the inviscid perfect gas model is the adiabatic exponent γ which we set 1.4 throughout, the value of a diatomic gas such as air. On a point of the boundary $\partial\Omega(t)$, $\boldsymbol{n} = (n_1, n_2)^T$ is the outward unit normal of $\Omega(t)$ and $\dot{\boldsymbol{x}}$ is the velocity of a boundary point $\boldsymbol{x}(t)$. Moving all boundary integrals on one side, the integrand contains the so called flux of the 2D Euler equations multiplied by $\boldsymbol{n}$. The flux, here for the case of a moving grid, is given by

$$f(U,\dot{\boldsymbol{x}}) \quad\equiv\quad U\,(\boldsymbol{v}-\dot{\boldsymbol{x}})^T + \begin{pmatrix} 0 & 0 \\ p & 0 \\ 0 & p \\ p\,u & p\,v \end{pmatrix}. \tag{2.2}$$

Another important quantity in the polytropic gas model is the speed of sound c, given by $c = \sqrt{\gamma\,p/\rho}\,$.

2.1.1.1 Moving impermeable boundaries

At a point on a moving impermeable boundary an inviscid flow should have the same normal velocity as the boundary, i.e. at a boundary point we want $\boldsymbol{v}^T\boldsymbol{n} = \dot{\boldsymbol{x}}^T\boldsymbol{n}$. We see that given such a boundary part $\Gamma(t) \subset \partial\Omega(t)$, the corresponding part of the boundary integral reduces to

$$\int_{\Gamma(t)} f(U, \dot{\boldsymbol{x}})\, \boldsymbol{n}\; ds \quad = \quad \int_{\Gamma(t)} \begin{pmatrix} 0 \\ p\, n_1 \\ p\, n_2 \\ p\, \dot{\boldsymbol{x}}^T \boldsymbol{n} \end{pmatrix} ds\ . \tag{2.3}$$

2.1.1.2 Restriction to a finite domain

Restricting the infinite domain to a finite domain, a necessary step before discretizing the fluid equations, one has to pose boundary conditions at the newly created artificial boundary. These have to be chosen such that the solution on the finite domain is the restriction of the solution on the infinite domain. This sounds impossible. One can merely formulate the so called non-reflecting boundary conditions which work well in many applications. See [61] for a case in which they don‘t bring satisfactory results. The general idea is to argue as follows:

Due to the hyperbolic nature of the Euler equations, one may also write them in characteristic form, in which the characteristic velocities and the quantities transported with these velocities (waves) become visible, see [31]. Now one wants the boundary condition to be such that waves moving outwards at the artificial boundary are not reflected into the interior of the domain. This is accomplished by cancelling any kind of wave movement that is directed inward at the boundary. A modification of the Euler equations with this property is given by

$$U_t \ +\ A_n^+(U)\, \frac{\partial U}{\partial n} \ +\ \frac{\partial f(U)\, \boldsymbol{\tau}}{\partial \tau} \quad = \quad 0\ . \tag{2.4}$$

Let us shortly explain this equation and show how to derive it: We assume that the artificial boundary does not move. Thus, using $f(U) \equiv f(U, 0)$ we can write (2.1) as a PDE,

$$U_t + \nabla f(U) \quad = \quad 0\, .$$

Transforming locally to the normal ($\boldsymbol{n}$) and tangential ($\boldsymbol{\tau}$) directions of the boundary, as in [57], one has

$$U_t \ +\ \frac{\partial f(U)\, \boldsymbol{n}}{\partial n} \ +\ \frac{\partial f(U)\, \boldsymbol{\tau}}{\partial \tau} \quad = \quad 0\ .$$

Here $\partial/\partial n$ and $\partial/\partial \tau$ are the spacial derivatives in normal, respectively tangential, direction. Then, we write the normal flux derivative in non-conservative form, see [31], page 139,

$$\frac{\partial f(U)\, \boldsymbol{n}}{\partial n} \quad \equiv \quad A_n(U)\, \frac{\partial U}{\partial n}$$

and replace the Jacobian $A_n(U)$ by $A_n^+(U)$, which forces the velocity of the inward moving waves to be zero, i.e. inward moving waves do not exist. $A_n^+(U)$ is commonly used in upwinding strategies; it is constructed by transforming $A_n(U)$ to diagonal form, then setting all negative eigenvalues (the speeds of the waves moving against the normal direction) to 0 and transforming back to obtain the matrix A_n^+, for details see [31], [42]. In [31] the corresponding boundary treatment for the one-dimensional case is proposed and equation (2.4) may also be derived directly from equation (34) in [61].

2.1.2 Structure

Here we consider a geometrically nonlinear thin elastic plate (modelling assumptions). It is in fact a von–Kármán plate model with infinite width to chord ratio, where variations in width direction are neglected and therefore a strip of unit width suffices to describe the deformation. This elastic strip may be regarded as a beam with a rectangular cross section. And we call it a plate or a panel in the sequel. We want the panel to be simply supported at the two fixed ends, therefore introducing the space $V := H^2(0,l) \cap H_0^1(0,l)$. $H^2(0,l)$ is a well–known Sobolev space, see [5], consisting of all measurable functions on the interval $(0,l)$ with distributional derivatives up to second order lying in $L_2(0,l)$. Accordingly, the functions in $H_0^1(0,l)$ have derivatives up to first order lying in $L_2(0,l)$ and homogeneous boundary values in the sense of traces. Below, the boundary conditions are discussed further. The variational formulation is to find $w \in C^2(\mathbb{R}, V)$ satisfying

$$D\,(w_{xx}, \varphi_{xx}) \; + \; N(w) \cdot (w_x, \varphi_x) \; + \; m\,(w_{tt}, \varphi) \;\; = \;\; -\,(p_1 - p_2, \varphi) \qquad \forall\, \varphi \in V \tag{2.5}$$

where the nonlinear term models a restoring force due to the panel stretching, with

$$N(w) \;=\; \frac{E\,h}{2\,l} \int_0^l w_x^2 \; dx \; .$$

Neglecting the nonlinearity, $N = 0$, the Bernoulli beam model remains. Here $(\cdot,\cdot)$ is the L_2-inner product; w is the panel deflection and p_1, respectively p_2, are the pressure on the upper and the lower surface of the panel. All other quantities appearing are constants defining the panel material and dimensions. Since we consider only aluminium panels later, we give the material constants for aluminium, taken from [37]:

$$\left.\begin{array}{rcll}
\rho_s & = & 2700\ kg/m^3 & \text{density of the panel material (aluminium)} \\
h & & & \text{panel thickness} \\
l & & & \text{panel chord length} \\
m & = & \rho_s h & \text{mass per unit area (unit width} \times \text{unit chord)} \\
E & = & 7.1 \cdot 10^{10}\ Pa & \text{Young's modulus of elasticity (aluminium)} \\
\nu & = & 0.34 & \text{Poisson's ratio (aluminium)} \\
D & = & Eh^3/12(1-\nu^2) & \text{panel stiffness} \\
h_{rel} & = & h/l &
\end{array}\right\} \tag{2.6}$$

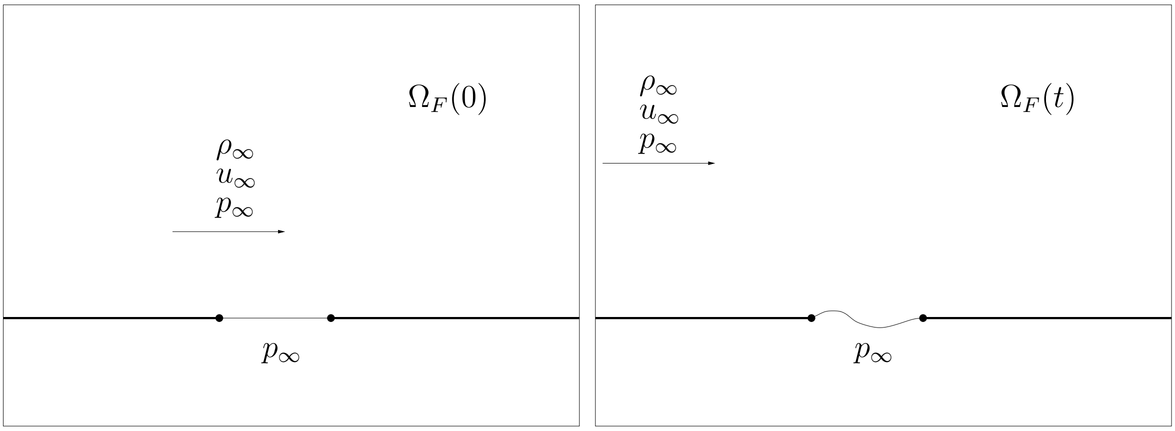

Figure 2.1: Fluid-structure-interaction at $t = 0$ and $t > 0$.

The mathematical conditions characterizing a beam which is simply supported at the two ends are

$$w(t,0) = w(t,l) = 0\,, \tag{2.7}$$

$$w_{xx}(t,0) = w_{xx}(t,l) = 0\,. \tag{2.8}$$

Since $V \subset \{f \in C^1[0,l] : f(0) = f(l) = 0\}$, the conditions (2.7) are satisfied by a solution of the variational formulation. (2.8) are natural boundary conditions. Assuming the solution to be smooth, $w(t) \in C^4[0,l] \cap V$, partial integration of the variational equation yields that w satisfies also (2.8) and for all $x \in [0,l]$ the PDE

$$D\,w_{xxxx} - N(w)\,w_{xx} + m\,w_{tt} = -\,(p_1 - p_2)\,. \tag{2.9}$$

2.1.3 Fluid–structure interaction

Now we define the physical problem we want to solve. Geometrically we consider a 2D cartesian coordinate system and place a panel, as introduced in Sec. 2.1.2, on the x-axis. It simply supported at its fixed endpoints at $x = 0$ and $x = l$. The remaining part of the x-axis constitutes a solid wall. At time $t = 0$ the plate is in its undeflected position and the halfspace $x > 0$ is filled with an inviscid gas slipping over panel and wall in a stationary state with density ρ_∞, x-velocity u_∞, y-velocity 0 and pressure p_∞ at infinity. A velocity distribution is assigned to the panel at $t = 0$, causing the panel to move, triggering the fluid-structure-interaction. Below the panel we assign p_∞ as a constant pressure. In Fig. 2.1 the two dots are the panel endpoints, the line between the dots is the undeflected panel at $t = 0$ in the left picture and the deflected panel at $t > 0$ in the right picture.

With the given initial conditions we can formulate the conditions under which the system evolves in time. The following have to be satisfied for all times.

- the fluid domain at time t is defined as the space above the deflecting panel and solid wall and is denoted by $\Omega_F(t)$, i.e. for each fluid interface point $\boldsymbol{x}(t)$ associated with a panel point $\xi \in [0, l]$,

$$\boldsymbol{x}(0) \;=\; (\xi, 0)^T , \quad \boldsymbol{x}(t) \;=\; (\xi, w(t,\xi))^T \tag{2.10}$$

- for all moving domains $\Omega(t) \subseteq \Omega_F(t)$ (2.1) holds,
- (2.5) holds with the r.h.s determined from the fluid pressure on top and p_∞ on the bottom,

$$\begin{aligned} p_1(t,\xi) \quad &\equiv \quad p(t,\xi,w(t,\xi)) && (2.11) \\ p_2 \quad &\equiv \quad p_\infty \end{aligned}$$

- at infinity we have $\rho = \rho_\infty$, $u = u_\infty$, $v = 0$, $p = p_\infty$,
- on the remaining boundary of $\Omega_F(t)$ the fluid velocity in direction $\boldsymbol{n}$ equals the velocity of the boundary in direction $\boldsymbol{n}$, i.e. on the fluid-structure interface

$$\boldsymbol{v}^T \boldsymbol{n} \;=\; \dot{\boldsymbol{x}}^T \boldsymbol{n} \;=\; w_t \, n_2 \tag{2.12}$$

2.2 Dimensionless equations

The dimensionless form of the fluid-structure system is obtained using the reference values from the fluid:

$$\begin{aligned} x^* &= l \\ v^* &= u_\infty \\ t^* &= u_\infty / l \\ \rho^* &= \rho_\infty \\ p^* &= \rho_\infty \, u_\infty^2 \\ w^* &= l \end{aligned}$$

With these reference values the dimensionless form of the Euler equations is exactly the same as the original one (2.1). The dimensionless form of the panel equation (2.9) becomes

$$\begin{aligned} w_{xxxx} - \frac{6\,(1-\nu^2)}{h_{rel}^2}\, w_{xx} \int_0^1 w_x^2 \, dx + \frac{12\,(1-\nu^2)}{E}\, \rho_s \, h_{rel} \, u_\infty^2 \, w_{tt} \quad &= \\ = \quad \frac{12\,(1-\nu^2)}{E}\, \rho_\infty \, u_\infty^2 \, (p_2 - p_1) \; . & \qquad (2.13) \end{aligned}$$

2.3 Energy considerations

Let us now look at the energy transfer between fluid and structure as an argument to reconfirm the coupling conditions (2.10), (2.11), (2.12). The energy argument will be considered in another light in the next Chapter to prove analytically a uniqueness theorem for an initial-boundary-value-problem of fluid-structure-interaction.

The energy transfer is correct if there is no energy production on the fluid-structure-interface. The energy equations for fluid and structure are given by

$$\frac{d}{dt}E_F \quad + \quad \int_{\partial\Omega_F(t)} \left(\frac{1}{2}\rho\,\boldsymbol{v}^2 + \frac{p}{\gamma-1}\right)(\boldsymbol{v}-\dot{\boldsymbol{x}})^T\boldsymbol{n}\;ds \quad = \quad \int_{\partial\Omega_F(t)} -p\,\boldsymbol{v}^T\boldsymbol{n}\;ds\;,$$

$$\frac{d}{dt}E_S \quad = \quad \int_0^l (p_2 - p_1)\,w_t\;dx\;,$$

where we have denoted the energy in fluid and structure by

$$E_F(t) \quad \equiv \quad \int_{\Omega_F(t)} \frac{1}{2}\rho\,\boldsymbol{v}^2 + \frac{p}{\gamma-1}\quad d\boldsymbol{x}\;,$$

$$E_S(t) \quad \equiv \quad \int_0^l \frac{m}{2}\,w_t^2 + \frac{D}{2}\,w_{xx}^2\;dx \quad + \quad \frac{E\,h}{2\,l}\left(\frac{1}{2}\int_0^l w_x^2\;dx\right)^2 \;.$$

Here the energy equation of the fluid is simply the last component of (2.1), taken over the whole fluid domain. The energy equation of the panel is obtained by multiplying the PDE (2.9) by w_t and integrating. The energy equation of the fluid-structure-system is obtained by adding the separate energy equations and plugging in the coupling conditions (2.10), (2.11), (2.12). No energy production within the system should occur, i.e. after dividing the fluid boundary into its interface part and the remaining part, $\partial\Omega_F = \Gamma_{FS}\cup\Gamma_F$, we want the production terms on the interface to cancel,

$$\begin{aligned}\int_{\Gamma_{FS}(t)} -\left(\frac{1}{2}\rho\,\boldsymbol{v}^2 + \frac{p}{\gamma-1}\right)(\boldsymbol{v}-\dot{\boldsymbol{x}})^T\boldsymbol{n} \;-\; p\,\boldsymbol{v}^T\boldsymbol{n}\;ds & \\ +\;\int_0^l -\,p_1\,w_t\;dx \quad \overset{!!!}{=} \quad 0\;. &\end{aligned} \tag{2.14}$$

Using the interface condition in the first integral and the parametrization of the interface $\boldsymbol{x}(t)\in\Gamma_{FS}(t)$ by $\boldsymbol{x}(t) = (\xi, w(t,\xi))^T$, $\xi\in[0,l]$, we get

$$\int_{\Gamma_{FS}(t)} -\left(\frac{1}{2}\rho\,\boldsymbol{v}^2 + \frac{p}{\gamma-1}\right)(\boldsymbol{v}-\dot{\boldsymbol{x}})^T\boldsymbol{n} \;-\; p\,\boldsymbol{v}^T\boldsymbol{n}\;ds \quad = \quad \int_{\Gamma_{FS}(t)} -p\;\dot{\boldsymbol{x}}^T\boldsymbol{n}\;ds \quad =$$

$$= \quad \int_0^l -p\;\dot{\boldsymbol{x}}^T\boldsymbol{n}\sqrt{1+w_x^2}\;d\xi$$

and further from $\dot{\boldsymbol{x}}^T \boldsymbol{n} = w_t n_2$ and $w_x = -n_1/n_2$ we obtain

$$\int_0^l -p \; \dot{\boldsymbol{x}}^T \boldsymbol{n} \sqrt{1+w_x^2} \; d\xi \quad = \quad \int_{\Gamma_{FS}(t)} -p \; w_t \, n_2 \, \sqrt{1+(n_1/n_2)^2} \; ds \quad =$$

$$= \quad \int_0^l -\mathrm{sign}(n_2) \; p \; w_t \; d\xi \quad = \quad \int_0^l p \; w_t \; d\xi \ .$$

Thus the cancellation (2.14) occurs, when (2.11) is used.

2.4 Parameter space

Let us summarize here all the parameters appearing in the above problem and discuss which dimensionless parameters are of importance to the fluid-structure-interaction. In the fluid we have the conditions at infinity ρ_∞, u_∞, p_∞, and the only parameter in the gas model is $\gamma = 1.4$ and the Mach-number at infinity is given by $M_\infty = u_\infty / \sqrt{\gamma \, p_\infty / \rho_\infty}$.

The panel is defined through its geometrical dimensions, the panel height h and the panel length l or $h_{rel} = h/l$; further we have the material constants, the panel density ρ_s, its modulus of elasticity E and its Poisson ratio ν. From these we have all other panel parameters, see (2.6).

Nondimensional parameters of an aeroelastic problem are:

- mass ratio

$$\mu \equiv \frac{\rho_\infty \, l}{\rho_s \, h} \equiv \frac{\rho_\infty}{\rho_s \, h_{rel}}$$

- nondimensional dynamic pressure

$$\lambda \equiv \frac{\rho_\infty \, u_\infty^2 \, l^3}{D} \equiv \frac{\rho_\infty \, u_\infty^2 \, 12 \, (1-\nu^2)}{E \, h_{rel}^3}$$

- reduced frequency

$$k \equiv \frac{\omega \, l}{2 \, u_\infty}$$

Actually the reduced frequency k is more appropriate in the context of unsteady aerodynamics, i.e. when considering the flow around a body oscillating in some degree of freedom with the frequency ω, e.g. [62]. In our case ω may be extracted from the data if the solution is known and a frequency can be identified.

The standard stability chart of an aeroelastic problem is given in the $M_\infty\lambda$-plane, showing regions of the systems qualitative behaviour, dividing stable from unstable behaviour. In our case this is achieved in the following way: We consider a panel with given ρ_s, E, ν and h_{rel}, which are all panel parameters needed in the dimensionless form

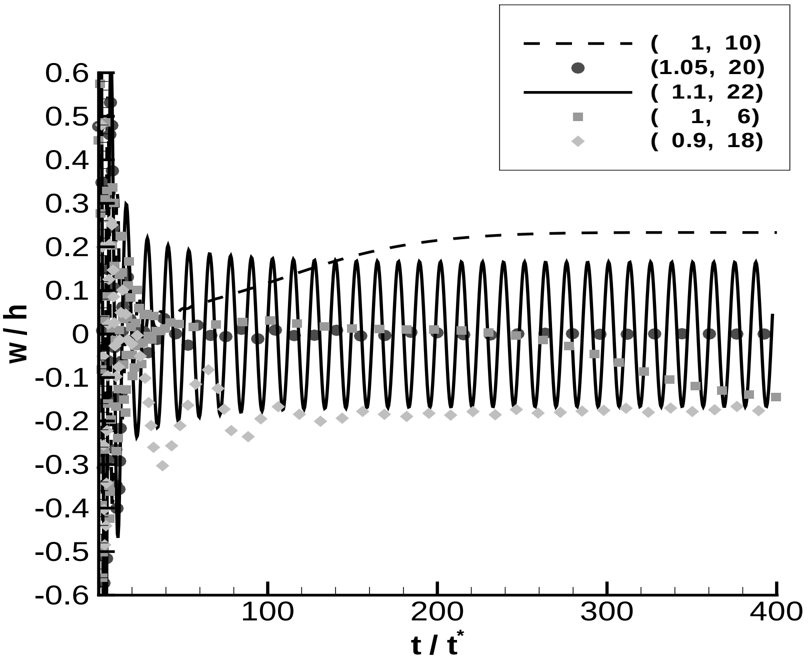

Figure 2.2: Panel mid–point deflections of an aluminium panel with $h_{rel} = 0.004537$, $\mu = 0.1$ for various (M_∞, λ) pairs, as given in the box.

(2.13). Further, we fix a value for μ and vary M_∞ and λ in the area of interest and get the remaining fluid parameters as

$$\rho_\infty = \mu \, \rho_s \, h_{rel} \ , \quad u_\infty = \sqrt{\frac{\lambda \, E \, h_{rel}^3}{12 \, (1 - \nu^2) \, \rho_\infty}} \ , \quad p_\infty = \frac{u_\infty^2 \, \rho_\infty}{\gamma \, M_\infty^2} \ . \tag{2.15}$$

Selecting some parameter pairs (M_∞, λ), for an aluminium panel with $h_{rel} = 0.004537$ and using $\mu = 0.1$, numerical simulations result in the time histories of the panel midpoint deflections w/h shown in Fig. 2.2.

The typical long time behaviours that can be observed are

- stable behaviour, a stationary state with undeflected panel,
- divergence, a stationary state with deflected panel,
- flutter, a limit cycle oscillation.

These may be charted in M_∞, λ–space. The stability boundary separates the stable behaviour from the others. In Fig. 2.3 we show a stability chart from [33]. The symbols are results produced in [33] and the solid line is the stability boundary obtained in [14], dividing the stable from the unstable regime.

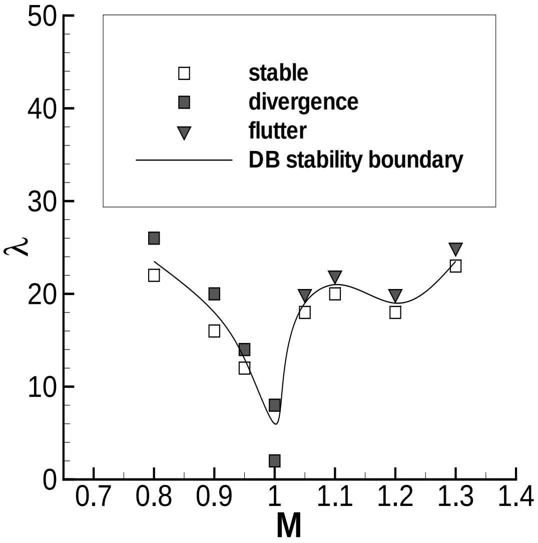

Figure 2.3: Stability chart of a simply supported aluminium panel with $h_{rel} = 0.004537$, $\mu = 0.1$, from [33] and [14].

Chapter 3

On Well-Posedness of an Aeroelastic Problem

Here we consider the question of well-posedness of the PDE-System describing an aeroelastic problem. The fluid and structure models used in the previous Chapter pose analytical difficulties. The difficulties attributed to the Euler equations are believed to be of technical nature, i.e. although the Euler equations are intensively investigated upon, their analysis is not developed satisfactorily yet. On the other hand, for the von-Kármán model non-unique solutions are present [32].

Thus we change the physical models, going to a higher level of modelling, obtaining equations with more complete analytical results. Including viscosity and heat-conduction in the flow model, we consider the (3D) compressible Navier-Stokes equations. The classical von-Kármán model plate model is the one, from which the strip model can be derived, that was used in the previous Chapter. Here we use a refined version of the von-Kármán model plate model, by taking the rotational energy of the cross-sections into account. Still the cross-sections are assumed to remain orthogonal to the deforming mid-plane of the plate. This plate model appeared in [47].

A classical approach in the analysis of PDE's is to obtain energy estimates for solutions of the PDE or the differential operator. Here we tackle the question of the uniqueness of assumed solutions for the aeroelastic system. The essential steps in the proof of the following theorem originate from the proof of theorem A in the paper of Secchi and Valli [55], who's basic idea stems from Serrin's paper [59]. Secchi and Valli have shown uniqueness and — for small times — existence of a solution for a free boundary value problem for the compressible Navier-Stokes equations; they considered the expansion of a gas with given environmental pressure.

We use a material fixed approach in the fluid, which means that we have a given amount of fluid material that is in contact with the plate. This is not completely satisfactory, since a true inflow or outflow as typical for our application of Chapter 2 is not present, one may merely generate a fluid movement by imposing a movement on the fluid's boundary particles. A uniqueness proof for the aeroelastic problem with a finite fluid domain with inflow and outflow boundaries could not yet be found. Also, the question of the existence of a solution is still open.

Some notation and differentiation rules

In this Chapter we use an overbar for all expressions represented in Eulerian coordinates and we remove the bar when changing to the Lagrangian representation. This choice was simply made to make the proof below more readable, since it uses Lagrangian coordinates throughout. For the same reason we make some more notational conventions:

Let $\Omega \in \mathbb{R}^n$ be a domain and $b : \Omega \to \mathbb{R}^n$, $A, C : \Omega \to \mathbb{R}^{n\times n}$ vector fields with components b_i and matrix fields with components a_{ij}, c_{ij} respectively, A_i the rows of A:

$$b = \begin{pmatrix} b_1 \\ b_2 \\ \vdots \\ b_n \end{pmatrix}, \quad A = \begin{pmatrix} a_{11} \cdots a_{1n} \\ a_{21} \cdots a_{2n} \\ \vdots \\ a_{n1} \cdots a_{nn} \end{pmatrix} = \begin{pmatrix} A_1 \\ A_2 \\ \vdots \\ A_n \end{pmatrix}$$

We use

$$A : C \equiv trace(A \cdot C) \equiv \sum_{i,j=1}^{n} a_{ji} c_{ij}\,, \quad \text{i.e.} \quad A^T : A = \sum_{i,j=1}^{n} a_{ij}^2\,.$$

The differentiation operator ∇ is considered as a vector

$$\nabla = \begin{pmatrix} \partial/\partial x_1 \\ \partial/\partial x_2 \\ \vdots \\ \partial/\partial x_n \end{pmatrix}$$

and we multipy it with matrices from the left and the right, as we usually multiply vectors and matrices, but instead of the multiplication of the components we always carry out the corresponding differentiation of the matrix component. For example

$$grad\; b = b\nabla^T = \begin{pmatrix} b_{1x_1} & \cdots & b_{1x_n} \\ b_{2x_1} & \cdots & b_{2x_n} \\ & \vdots & \\ b_{nx_1} & \cdots & b_{nx_n} \end{pmatrix}$$

$$div\; b = b^T\nabla = \nabla^T b$$

$$\nabla^T A = (a_{11x_1} + a_{21x_2} + \cdots + a_{n1x_n}\,, \quad a_{12x_1} + a_{22x_2} + \cdots + a_{n2x_n}\,, \\ \cdots\,, \quad a_{1nx_1} + a_{2nx_2} + \cdots + a_{nnx_n})$$

Later on, vectors of the form

$$\begin{pmatrix} (A_1^T\nabla^T) : C^T \\ (A_2^T\nabla^T) : C^T \\ \vdots \\ (A_n^T\nabla^T) : C^T \end{pmatrix}$$

will appear; symbolically we denote them by $[A\nabla^T] \substack{\circ \\ \circ} C^T$. (Note, that $A\nabla^T$ wouldn't make sense and we don't intend to define it as an n-array of $n \times n$-matrices, as it only appears in the form given above.) Therefore we have the following product rules:

$$(b^T C)\nabla \;=\; b^T(C\nabla) \;+\; (b\nabla^T)^T : C \;=\; b^T(C\nabla) \;+\; (b\nabla^T) : C^T$$

$$(AC)\nabla \;=\; A(C\nabla) \;+\; [A\nabla^T] \substack{\circ \\ \circ} C^T \;,$$

where the second rule is obtained by applying the first in every component.

Fluid equations in Eulerian coordinates

We first give a well–known form of the Navier-Stokes equations in Eulerian coordinates.

$$\frac{D}{Dt}\,\overline{\rho} \;+\; \overline{\rho}\,(\overline{\nabla}^T \overline{\boldsymbol{v}}) \;=\; 0$$

$$\overline{\rho}\,\frac{D}{Dt}\,\overline{\boldsymbol{v}} \;=\; \overline{S}\,\overline{\nabla}$$

$$\overline{\rho}\,c_v(\overline{\theta})\,\frac{D}{Dt}\,\overline{\theta} \;=\; \overline{S} : \overline{D} + \kappa\,(\overline{\theta}\,\overline{\nabla}^T)\,\overline{\nabla}$$

$$\text{with}\quad \overline{D} \;=\; 1/2 \cdot (\overline{\boldsymbol{v}}\,\overline{\nabla}^T + \overline{\nabla}\,\overline{\boldsymbol{v}}^T)\,,\; \overline{S} \;=\; -p(\rho,\theta)I + 2\mu\,\overline{D} + (\zeta - \frac{2}{3}\mu)\,(\overline{\boldsymbol{v}}^T\,\overline{\nabla})\cdot I$$

Here $\overline{\nabla}$ is the gradient with respect to Eulerian coordinates and D/Dt is the substantial derivative. The uniqueness proof will depart from the corresponding fluid equations in Lagrangian coordinates. In the equations the following quantities appear:

ρ	density
$\boldsymbol{v}$	velocity vector
$\boldsymbol{\eta}$	particle path vector
θ	absolute temperature
κ	constant heat conduction coefficient
μ, ζ	constant viscosity coefficients
D	deformation tensor
S	stress tensor
p	$= p(\rho,\theta)$ the state equation for the pressure
c_v	$= c_v(\theta)$ the specific heat capacity of the (thermodynamically) ideal gas, i.e. we have for the specific internal energy $e = e(\theta)$, compare [58], page 174

Transformation to Lagrangian coordinates

The transformation to Lagrangian coordinates is defined via the particle paths $\boldsymbol{\eta}$:

$$\boldsymbol{\eta}_t(t,\boldsymbol{x}) \;=\; \overline{\boldsymbol{v}}(t,\boldsymbol{\eta}(t,\boldsymbol{x}))\,,\quad \boldsymbol{\eta}(0,\boldsymbol{x}) \;=\; \boldsymbol{x} \qquad for \quad \boldsymbol{x} \in \Omega_F$$

Then, for example, the density in Lagrangian coordinates is given by

$$\rho(t,\boldsymbol{x}) \,:=\, \overline{\rho}(t,\boldsymbol{\eta}(t,\boldsymbol{x}))\ .$$

Further we introduce an abbreviation for the determinant of the particle path gradient, which is to appear frequently in the sequel,

$$\mathcal{D}(t,\boldsymbol{x}) \,:=\, det(\boldsymbol{\eta}\nabla^T)\ .$$

Next we discuss how boundary integrals transform to Lagrangian coordinates, which enables us to formulate boundary conditions in Lagrangian coordinates. For a moving volume $\Omega(t) = \{\boldsymbol{\eta}(t,\boldsymbol{x}) : \boldsymbol{x} \in \Omega\}$ of fluid material with $\Omega \subset \Omega_F$ let $\overline{\boldsymbol{n}}(t,\boldsymbol{\xi})$ denote the outward normal in $\boldsymbol{\xi} \in \partial\Omega(t)$. Then we have the following relation for the surface forces:

$$\int_{\Gamma(t)} \overline{S}(t,\boldsymbol{\xi})\,\overline{\boldsymbol{n}}(t,\boldsymbol{\xi})\,d\sigma \quad = \quad \int_{\Gamma} \mathcal{D}(t,\boldsymbol{x})\cdot\overline{S}(t,\boldsymbol{\eta}(t,\boldsymbol{x}))\cdot(\boldsymbol{\eta}(t,\boldsymbol{x})\nabla^T)^{-T}\,\boldsymbol{n}\,ds$$

for all pieces $\Gamma \subseteq \partial\Omega\,,\ \Gamma(t) := \{\boldsymbol{\eta}(t,\boldsymbol{x}) : \boldsymbol{x} \in \Gamma\}$, compare [28], pages 178 and 184. In the continuum mechanics of large deformations, after defining $S(t,\boldsymbol{x}) := \overline{S}(t,\boldsymbol{\eta}(t,\boldsymbol{x}))$, the tensor

$$\mathcal{D}(t,\boldsymbol{x})\cdot S(t,\boldsymbol{x})\cdot(\boldsymbol{\eta}(t,\boldsymbol{x})\nabla^T)^{-T}$$

is referred to as the first Piola-Kirchhoff-stress-tensor, [28], page 178, and it will appear in our formulation of the interface conditions below.

Particular terms transform as follows from Eulerian to Lagrangian coordinates:

$$\rho(t,\boldsymbol{x}) := \overline{\rho}(t,\boldsymbol{\eta}(t,\boldsymbol{x})),\ \boldsymbol{v}(t,\boldsymbol{x}) := \overline{\boldsymbol{v}}(t,\boldsymbol{\eta}(t,\boldsymbol{x})),\ \theta(t,\boldsymbol{x}) := \overline{\theta}(t,\boldsymbol{\eta}(t,\boldsymbol{x})), \quad \boldsymbol{x} \in \Omega_F$$

Hence

$$\frac{\partial}{\partial x_i}\rho(t,\boldsymbol{x}) = \frac{d}{dx_i}\overline{\rho}(t,\boldsymbol{\eta}(t,\boldsymbol{x})) = \sum_{j=1}^{3}\overline{\rho}_{\xi_j}\cdot(\boldsymbol{\eta}_j)_{x_i} = (\overline{\rho}\overline{\nabla}^T)\cdot\boldsymbol{\eta}_{x_i}\,,$$

and therefore

$$\rho\nabla^T = (\overline{\rho}\cdot\overline{\nabla}^T)(\boldsymbol{\eta}\nabla^T) \quad \text{and} \quad (\rho\nabla^T)\cdot(\boldsymbol{\eta}\nabla^T)^{-1} = \overline{\rho}\cdot\overline{\nabla}^T\,,$$

and in the last identity, $(t,\boldsymbol{x})$ appears as argument on the left, and ∇ is the gradient with respect to $\boldsymbol{x}$; the argument on the right is $(t,\boldsymbol{\xi})$ with $\boldsymbol{\xi} = \boldsymbol{\eta}(t,\boldsymbol{x})$, and $\overline{\nabla}$ is taken with respect to $\boldsymbol{\xi}$. Similarly, we have

$$(\boldsymbol{v}\nabla^T)\cdot(\boldsymbol{\eta}\nabla^T)^{-1} \,=\, \overline{\boldsymbol{v}}\cdot\overline{\nabla}^T \tag{3.1}$$

$$\overline{\nabla}^T\overline{\boldsymbol{v}} \,=\, \overline{div}(\overline{\boldsymbol{v}}) \,=\, tr(\overline{\boldsymbol{v}}\cdot\overline{\nabla}^T) \,=\, (v\nabla^T):(\boldsymbol{\eta}\nabla^T)^{-1} \tag{3.2}$$

$$\frac{D}{Dt}\overline{\rho}(t,\boldsymbol{\xi}) \,=\, \overline{\rho}_t + (\overline{\rho}\cdot\overline{\nabla}^T)\overline{\boldsymbol{v}} \,=\, \frac{d}{dt}\overline{\rho}(t,\boldsymbol{\eta}(t,\boldsymbol{x})) \,=\, \rho_t\ . \tag{3.3}$$

3.1 The IBVP

With the above explanations we are ready to state an initial boundary value problem describing the interaction of a plate with a given amount of fluid material. Our second interface condition, which corresponds to the boundary condition at the free boundary in [55], is completely formulated in the reference configuration, in contrast to [55]. We consider this the natural formulation for a material fixed fluid description. It is obtained by transforming the Navier–Stokes equations from Eulerian coordinates with the aid of the relations (3.2), (3.3) to Lagrangian coordinates.

Fluid (in Lagrangian coordinates)[1]:

$$\begin{aligned} \rho_t &= -\rho(\boldsymbol{v}\nabla^T) : (\boldsymbol{\eta}\nabla^T)^{-1} && for \quad \boldsymbol{x} \in \Omega_F \\ \rho\boldsymbol{v}_t &= S\nabla^T \mathbin{\scriptstyle 8} (\boldsymbol{\eta}\nabla^T)^{-1} && for \quad \boldsymbol{x} \in \Omega_F \\ \rho c_v\theta_t &= S : D + \kappa \cdot ([(\boldsymbol{\eta}\nabla^T)^{-T}(\theta\nabla)]\nabla^T) : (\boldsymbol{\eta}\nabla^T)^{-1} && for \quad \boldsymbol{x} \in \Omega_F \\ \boldsymbol{v}(t,\boldsymbol{x}) &= \boldsymbol{u}_t^w(t,\boldsymbol{x}) && for \quad \boldsymbol{x} \in \partial\Omega \setminus \Gamma_{FS} \\ \theta(t,\boldsymbol{x}) &= \theta^w(t,\boldsymbol{x}) && for \quad \boldsymbol{x} \in \partial\Omega_F \\ \rho(0,\boldsymbol{x}) = \rho_o(\boldsymbol{x}), \quad \boldsymbol{v}(0,\boldsymbol{x}) = \boldsymbol{v}_o(\boldsymbol{x}), \quad \theta(0,\boldsymbol{x}) &= \theta_o(\boldsymbol{x}) && in \quad \Omega_F \end{aligned}$$

where $S(t,\boldsymbol{x}) := \overline{S}(t,\boldsymbol{\eta}(t,\boldsymbol{x}))$ and $D(t,\boldsymbol{x}) := \overline{D}(t,\boldsymbol{\eta}(t,\boldsymbol{x}))$, which for example leads to

$$\begin{aligned} S \quad = \quad & -\pi(\rho,\theta) \cdot I \quad + \quad \mu \cdot [(\boldsymbol{v}\nabla^T)(\boldsymbol{\eta}\nabla^T)^{-1} + (\boldsymbol{\eta}\nabla^T)^{-T}(\boldsymbol{v}\nabla^T)^T] \quad + \\ & + \quad (\zeta - \frac{2}{3}\mu) \cdot (\boldsymbol{v}\nabla^T) : (\boldsymbol{\eta}\nabla^T)^{-1} \cdot I \end{aligned}$$

Particle paths:

$$\begin{aligned} \boldsymbol{\eta}_t(t,\boldsymbol{x}) &= \boldsymbol{v}(t,\boldsymbol{x}) && for \quad \boldsymbol{x} \in \overline{\Omega}_F \\ \boldsymbol{\eta}(0,\boldsymbol{x}) &= \boldsymbol{x} && for \quad \boldsymbol{x} \in \overline{\Omega}_F \end{aligned}$$

Interface condition:

$$\begin{aligned} -w_t(t,x_1,x_2) \cdot \boldsymbol{n} &= \boldsymbol{v}(t,\boldsymbol{x}) && for \quad \boldsymbol{x} = (x_1,x_2,0) \in \Gamma_{FS} && (i) \\ -p_1(t,x_1,x_2) &= \boldsymbol{n}^T \cdot \left[\mathcal{D} \cdot S \cdot (\boldsymbol{\eta}\nabla^T)^{-T}\right](t,\boldsymbol{x}) \cdot \boldsymbol{n} && for \quad \boldsymbol{x} = (x_1,x_2,0) \in \Gamma_{FS} && (ii) \end{aligned}$$

---

[1] Here, the continuity equation can be replaced by $\rho(t,\boldsymbol{x}) \cdot \mathcal{D}(t,\boldsymbol{x}) = \rho_o(x)$ which is a direct consequence of the conservation of mass in integral form and, on the other hand, implies the continuity equation obtained from the transformation to Lagrangian coordinates ([28], S. 89).

Plate:

$$\begin{aligned}
w_{tt} - \alpha \cdot \Delta w_{tt} + \beta \cdot \Delta^2 w - [w,\psi] &= p_2 - p_1 \quad for \quad (x_1,x_2) \in \Omega_S \\
\gamma \cdot \Delta^2 \psi + [w,w] &= 0 \quad for \quad (x_1,x_2) \in \Omega_S \\
w(t,x_1,x_2) = 0, \quad \frac{\partial w(t,x_1,x_2)}{\partial n^S} &= 0 \quad for \quad (x_1,x_2) \in \partial\Omega_S \\
\psi(t,x_1,x_2) = 0, \quad \frac{\partial \psi(t,x_1,x_2)}{\partial n^S} &= 0 \quad for \quad (x_1,x_2) \in \partial\Omega_S \\
w(0,x_1,x_2) = 0, \quad w_t(0,x_1,x_2) &= 0 \quad for \quad (x_1,x_2) \in \Omega_S
\end{aligned}$$

In the plate equation the so–called Airy function ψ, which characterizes the in–plane stress distribution, appears as an unknown besides the deflection w. α, β, γ are positive material constants. On the boundary of the two dimensional structural domain the normal is n^S. Further, the Laplace operator (in 2D) is defined by $\Delta w \equiv (w\nabla^T)\nabla$ according to the introduced notation. The bracket abbreviates

$$[w,\psi] \quad \equiv \quad w_{x_1x_1}\psi_{x_2x_2} - 2w_{x_1x_2}\psi_{x_1x_2} + w_{x_2x_2}\psi_{x_1x_1} \ .$$

Further, the following data is assumed to be given:

$p_2(t,x)$	external pressure on the lower surface of the plate
$\boldsymbol{u}^w(t,x)$	movement of the fluid boundary, except for the interface
$\theta^w(t,x)$	temperature at the fluid boundary
$\rho_o(x)$	initial density
$\boldsymbol{v}_o(x)$	initial velocity
$\theta_o(x)$	initial temperature

3.2 A uniqueness theorem

First, some notation: $Q_T := (0,T) \times \Omega_F$, and $\mid \cdot \mid$ denotes the norm of a scalar, vector or matrix. For vectors (b) and matrices (A), we use

$$\mid b \mid = (b^T b)^{1/2}, \quad \mid A \mid = (A^T : A)^{1/2} = (trace(A^T A))^{1/2}.$$

Further, in this chapter $\| \cdot \|$ is reserved for norms in function spaces and equipped with the corresponding subscript. For example, for a measurable and integrable matrix field $A(t,\boldsymbol{x})$ on Q_T, we have

$$\| A \|_{L^1(0,T;L^\infty(\Omega_F))} = \int_0^T \| A(t,\boldsymbol{x}) \|_{L^\infty(\Omega_F)} \, dt \ = \int_0^T ess.sup_{\,\boldsymbol{x}\in\Omega_F} \mid A(t,\boldsymbol{x}) \mid \ dt.$$

Theorem 1: Let Ω_F and Ω_S be bounded domains with Lipschitz boundary, and let the constants $\mu,\ \zeta,\ \kappa > 0$ and the thermodynamic relations $p(\rho,\theta) \in C^1$ and $c_v(\theta) \in C^1$, so that there is a $c_{v*} > 0$ with $c_v \geq c_{v*}$. Further, let the constants $\alpha, \beta, \gamma > 0$

and $p_2 \in L^2(0,T;L^2(\Omega_S))$. Then the initial boundary value problem has at most one solution in the following class of functions.

$$\begin{aligned}
w \in C(0,T;W^{2,2}(\Omega_S)),\ \psi \in L^\infty(0,T;W^{2,2}(\Omega_S)) &\quad \textit{and} \quad w_t \in C(0,T;W^{1,2}(\Omega_S)),\\
\rho \in L^\infty(Q_T),\ D\rho \in L^2(0,T;L^\infty(\Omega_F)) &\quad \textit{and} \quad \exists \rho_* > 0 :\ \rho \geq \rho_* \ \textit{in}\ Q_T,\\
\boldsymbol{v} \in L^\infty(Q_T),\ D\boldsymbol{v} \in L^2(0,T;L^\infty(\Omega_F)) &\quad \textit{and} \quad D^2\boldsymbol{v} \in L^2(0,T;L^\infty(\Omega_F)),\\
\theta \in L^\infty(Q_T),\ D\theta \in L^2(0,T;L^\infty(\Omega_F)) &\quad \textit{and} \quad D^2\theta \in L^2(0,T;L^\infty(\Omega_F)),\\
\boldsymbol{\eta} \in L^\infty(Q_T),\ D\boldsymbol{\eta} \in L^\infty(Q_T) &\quad \textit{and} \quad D^2\boldsymbol{\eta} \in L^\infty(Q_T)
\end{aligned}$$

$$\text{and}^2 \quad \exists \mathcal{D}_* > 0 :\ \mathcal{D} \equiv det(\boldsymbol{\eta}\nabla^T) \geq \mathcal{D}_* \quad in \quad Q_T$$

$$\text{and} \quad \boldsymbol{\eta}(t,\cdot\,) :\ \overline{\Omega}_A \longrightarrow \mathbb{R}^n \quad \text{is injective for every} \quad t \in [0,T]\ .$$

Before giving the proof we discuss some points related to the smoothness demanded for the solution:

After separating the fluid equations such that only the time derivatives ρ_t, $\boldsymbol{v}_t$, θ_t stand on the left-hand sides of the equations, for a function with the required regularity, all right-hand sides (these contain all partial derivatives in the space directions) in the differential equations are in $L^1(0,T;L^2(\Omega_F))$ resp. $L^1(0,T;L^2(\Omega_S))$, and the solution can be interpreted in the $\mathcal{D}((0,T);L^2(\Omega_F))$- resp. $\mathcal{D}((0,T);L^2(\Omega_S))$-distribution sense. Further, the continuity of the solution in the time direction in the sense $\rho, \boldsymbol{v}, \theta, \boldsymbol{\eta}, \boldsymbol{\eta}\nabla^T \in C([0,T];L^2(\Omega_F))$ follows [68] (theorem 25.5). Besides determining that way the sense in which the initial values are satisfied, the quantity $E(0)$ (introduced below, after Gronwall's Lemma) is also well-defined. For that reason we demanded a "slightly" higher smoothness for v and θ compared to [55] [3]. On the other hand, this smoothness for $\boldsymbol{v}$ is also important since it determines the smoothness of the right hand side of the plate equation through the interface condition.

All boundary and interface conditions can be interpreted in the trace sense ($H^{1/2}(\Gamma)$ or $L^2(\Gamma)$ almost everywhere (a.e.) on $[0,T]$).

As a preview of the proof we show the type of estimate we need in order to apply Gronwall's Lemma, here given in the version of [13], page 559:

Gronwall's Lemma: Given $E \in L^\infty(0,T)$ and $c \in L^1(0,T)$ with $E(t) \geq 0$ and $c(t) \geq 0$ a.e. on $[0,T]$ then for an arbitrary constant E_o the inequality

$$E(t) \quad \leq \quad E_o \; + \int_0^t c(\tau)\, E(\tau)\, d\tau \quad \text{a.e. on } [0,T]$$

---

[2] According to earlier remarks on the various forms of the continuity equation in Lagrangian coordinates, if we require $\rho_o(x) \geq \rho_{o*} > 0$, we have: existence of the lower bound $\mathcal{D}_*$ for $\mathcal{D}(t,\boldsymbol{x}) \Leftrightarrow$ existence of an upper bound for ρ.

[3] In [55], only L^1 rather than L^2 was demanded for $D^2v, D^2\theta$, which leads to $\boldsymbol{v}_t, \theta_t \in L^1(0,T;L^\infty(\Omega_F))$. However, according to [13], Chapter XVIII, section 3, especially page 483, prop. 9, this is not sufficient for $v, \theta \in C([0,T];L^\infty(\Omega_F))$.

implies the inequality

$$E(t) \quad \leq \quad E_o \cdot exp\left(\int_0^t c(\tau)\,d\tau\right) \quad \text{a.e. on } [0,T]\,.$$

Now, we assume there exist two solutions which satisfy the regularity conditions of the theorem and the same initial value and boundary conditions: $\tilde{w}, \tilde{\psi}, \tilde{\rho}, \tilde{\boldsymbol{v}}, \tilde{\theta}, \tilde{\boldsymbol{\eta}}$ and $w, \psi, \rho, \boldsymbol{v}, \theta, \boldsymbol{\eta}$. The differences are defined as $w' := \tilde{w} - w, \psi' := \tilde{\psi} - \psi, \rho' := \tilde{\rho} - \rho, ...$ Then in the proof we will find the time dependent coefficient $c(t)$ with the choice

$$\begin{aligned} E(t) \;=\; & \frac{1}{2}\int_{\Omega_S} {w'_t}^2 \;+\; \alpha\,|\nabla w'_t|^2 \;+\; \beta\,(\Delta w')^2\,dx\,dy \quad + \\ & \int_{\Omega_F} |\boldsymbol{\eta}'|^2 + \;|\boldsymbol{\eta}'\nabla^T|^2 \;+\; |\rho'|^2 \;+\; \frac{1}{2}\tilde{\mathcal{D}}\,\tilde{\rho}\,|\boldsymbol{v}'|^2 \;+\; \frac{1}{2}\tilde{\rho}\,\tilde{c}_v\,\tilde{\mathcal{D}}\,|\theta'|^2\,d\boldsymbol{x}\;. \end{aligned}$$

$E(t)$ is related to the energy in the physical sense, and we will have $E_o = E(0)$ which vanishes due to the initial conditions [4] . Thus $E(t) \equiv 0$ from Gronwall's Lemma, i.e. uniqueness will follow.

Proof: Let the two solutions and their difference be defined as above.

Energy estimate for the plate: In the book of Lions [39] (pages 50-53) we find the identity

$$\begin{aligned} \frac{1}{2}\int_{\Omega_S} {w'_t}^2 + \alpha|w'_t\nabla|^2 + \beta(\Delta w')^2\,d(x_1,x_2) \quad &= \\ = \quad \int_0^t\int_{\Omega_S}\Big([\tilde{w},\tilde{\psi}] - [w,\psi]\Big)\cdot w'_t \quad - \quad (\tilde{p}_1 - p_1)\cdot w'_t \quad d(x_1,x_2)\,d\tau\;, \end{aligned}$$

and further integral estimates for the term $\Big([\tilde{w},\tilde{\psi}] - [w,\psi]\Big)\cdot w'_t$ from [39] (compare the step "Unicité", pg. 52) result in the *energy estimate for the plate*:

$$\begin{aligned} \frac{1}{2}\int_{\Omega_S} {w'_t}^2 + \alpha|w'_t\nabla|^2 + \beta(\Delta w')^2\,d(x_1,x_2) \quad &\leq \\ \leq \quad \int_0^t\int_{\Omega_S} c_0\cdot\big(\,|w'_t\nabla|^2 + (\Delta w')^2\,\big) \quad - \quad w'_t\cdot(\tilde{p}_1 - p_1) \quad d(x_1,x_2)\,d\tau \end{aligned}$$

for almost all $t \in [0,T]$ *with a constant* $c_0 > 0$

Energy estimates for the fluid: The nonlinearity in the fluid equations is tackled with the simple relations

$$\tilde{a}\tilde{b} - ab = ab' + a'\tilde{b}, \quad \tilde{a}\tilde{b}\tilde{c} - abc = a'\tilde{b}\tilde{c} + ab'\tilde{c} + abc',$$

---

[4] As already discussed above, $E(0)$ is well-defined due to the regularity of the solutions. We have to add that $D\eta \in L^2(0,T;H^{1,\infty}(\Omega_F))$, $(D\eta)_t \in L^2(0,T;L^\infty(\Omega_F))$ i.e. $D\eta \in C([0,T];L^2(\Omega_F))$ and similarly we get that $Du \in C([0,T];L^2(\Omega_S))$, so that $\int_{\Omega_S}\frac{1}{2}D^{E'} : S^{E'}\,d\boldsymbol{x} \in C[0,T]$.

where $\tilde{a}, \tilde{b}, \tilde{c}, a, b, c \in \mathbb{R}$ *and* $a' := \tilde{a} - a,\ b' := \tilde{b} - b,\ c' := \tilde{c} - c$

yield $\rho', \boldsymbol{v}', \theta'$ after subtracting the differential equations of both solutions. We will refer to the "$\tilde{a}\tilde{b}$-rule" whenever we apply one of these relations.

Estimates for the particle paths: First, we have $\boldsymbol{\eta}'_t = \boldsymbol{v}'$ and $\boldsymbol{\eta}'^T_t \boldsymbol{\eta}' = \boldsymbol{v}'^T \boldsymbol{\eta}'$, hence

$$\frac{d}{dt} \int_{\Omega_F} \frac{1}{2} |\boldsymbol{\eta}'|^2 \, d\boldsymbol{x} \quad = \quad \int_{\Omega_F} \boldsymbol{v}'^T \boldsymbol{\eta}' \, d\boldsymbol{x} \quad \leq \quad \frac{1}{2} \int_{\Omega_F} |\boldsymbol{v}'|^2 + \, |\boldsymbol{\eta}'|^2 \, d\boldsymbol{x} \; .$$

The regularity required in the theorem allows for $(\boldsymbol{\eta}'_t)\nabla^T = (\boldsymbol{\eta}'\nabla^T)_t = \boldsymbol{v}'\nabla^T$, hence

$$\frac{d}{dt} \int_{\Omega_F} \frac{1}{2} |\boldsymbol{\eta}'\nabla^T|^2 \, d\boldsymbol{x} \quad = \quad \int_{\Omega_F} (\boldsymbol{v}'\nabla^T)^T : (\boldsymbol{\eta}'\nabla^T) \, d\boldsymbol{x} \quad \leq$$

$$\leq \quad \frac{1}{2c} \int_{\Omega_F} |\boldsymbol{\eta}'\nabla^T|^2 \, d\boldsymbol{x} \quad + \quad \frac{c}{2} \int_{\Omega_F} |\boldsymbol{v}'\nabla^T|^2 \, d\boldsymbol{x}$$

for arbitrary $c > 0$. The sum of both inequalities gives us the *estimate for the particle paths*:

For each $\bar{c}_1 > 0$ *there exists a constant* $c_1 > 0$, *such that*

$$\frac{d}{dt} \int_{\Omega_F} |\boldsymbol{\eta}'|^2 + \, |\boldsymbol{\eta}'\nabla^T|^2 \, d\boldsymbol{x} \quad \leq$$

$$\leq \quad c_1 \int_{\Omega_F} |\boldsymbol{v}'|^2 + \, |\boldsymbol{\eta}'|^2 + \, |\boldsymbol{\eta}'\nabla^T|^2 \, d\boldsymbol{x} \quad + \quad \bar{c}_1 \int_{\Omega_F} |\boldsymbol{v}'\nabla^T|^2 \, d\boldsymbol{x} \; .$$

Later, we choose a particular $\bar{c}_1$; this choice will depend on the constant c_o appearing in the energy estimate for the momentum equation.

Estimate for continuity equation: Subtraction of the continuity equations provides

$$\tilde{\rho}_t - \rho_t = -\tilde{\rho}(\tilde{\boldsymbol{v}}\nabla^T) : (\tilde{\boldsymbol{\eta}}\nabla^T)^{-1} + \rho(\boldsymbol{v}\nabla^T) : (\boldsymbol{\eta}\nabla^T)^{-1} \; .$$

Applying the $\tilde{a}\tilde{b}$-rule in combination with $Q' := (\tilde{\boldsymbol{\eta}}\nabla^T)^{-1} - (\boldsymbol{\eta}\nabla^T)^{-1}$ yields

$$\rho'_t = -\rho'(\tilde{\boldsymbol{v}}\nabla^T) : (\tilde{\boldsymbol{\eta}}\nabla^T)^{-1} + \rho(\tilde{\boldsymbol{v}}\nabla^T) : Q' + \rho(\boldsymbol{v}'\nabla^T) : (\boldsymbol{\eta}\nabla^T)^{-1}.$$

Thus

$$\frac{d}{dt} \int_{\Omega_F} |\, \rho' \,|^2 \;\; d\boldsymbol{x} \quad = \quad 2 \int_{\Omega_F} \rho' \rho'_t \;\; d\boldsymbol{x} \quad =$$

$$= \quad -\, 2 \int_{\Omega_F} \rho' \cdot [\rho'(\tilde{\boldsymbol{v}}\nabla^T) : (\tilde{\boldsymbol{\eta}}\nabla^T)^{-1} + \rho(\tilde{\boldsymbol{v}}\nabla^T) : Q' + \rho(\boldsymbol{v}'\nabla^T) : (\boldsymbol{\eta}\nabla^T)^{-1}] \quad d\boldsymbol{x}$$

$$\leq \quad \int_{\Omega_F} 2|\rho'|^2 \cdot |\tilde{\boldsymbol{v}}\nabla^T| \cdot |(\tilde{\boldsymbol{\eta}}\nabla^T)^{-1}| \; + \; |\rho| \cdot |\tilde{\boldsymbol{v}}\nabla^T| \cdot (|\rho'|^2 + |Q'|^2) \, +$$

$$+ \, 2|\rho'| \cdot \|\rho\|_{L^\infty(Q_T)} \cdot \|(\boldsymbol{\eta}\nabla^T)^{-1}\|_{L^\infty(Q_T)} \cdot |\boldsymbol{v}'\nabla^T| \quad d\boldsymbol{x} \; .$$

$\alpha := \|\rho\|_{L^\infty(Q_T)} \cdot \|(\boldsymbol{\eta}\nabla^T)^{-1}\|_{L^\infty(Q_T)}$ is, according to the assumptions, larger than zero, and via Cramer's rule we get[5] $(\boldsymbol{\eta}\nabla^T)^{-1} \in L^\infty(Q_T)$. This yields, for all $\bar{c}_2 > 0$,

$$2\alpha|\rho'| \cdot |\boldsymbol{v}'\nabla^T| \; = \; \alpha \cdot 2 \cdot |\rho'|(\frac{4\alpha}{\bar{c}_2})^{1/2} \cdot |\boldsymbol{v}'\nabla^T|(\frac{\bar{c}_2}{4\alpha})^{1/2} \; \leq \; \frac{4\alpha^2}{\bar{c}_2}|\rho'|^2 \; + \; \frac{\bar{c}_2}{4}|\boldsymbol{v}'\nabla^T| \, ,$$

$$\frac{d}{dt}\int_{\Omega_F} |\; \rho' \;|^2 \; d\boldsymbol{x} \quad \leq \quad \int_{\Omega_F} 2|\rho'|^2 \cdot \|\tilde{\boldsymbol{v}}\nabla^T\|_{L^\infty(\Omega_F)} \cdot \|(\tilde{\boldsymbol{\eta}}\nabla^T)^{-1}\|_{L^\infty(Q_T)} +$$

$$+ \; \|\rho\|_{L^\infty(Q_T)} \cdot \|\tilde{\boldsymbol{v}}\nabla^T\|_{L^\infty(\Omega_F)} \cdot (|\rho'|^2 + |Q'|^2) \; + \; \frac{4\alpha^2}{\bar{c}_2}|\rho'|^2 \; + \; \frac{\bar{c}_2}{4}|\boldsymbol{v}'\nabla^T| \quad d\boldsymbol{x} \, .$$

Using the Lipschitz continuity of the matrix inversion, we obtain[6]

$$|Q'| \; = \; |(\tilde{\boldsymbol{\eta}}\nabla^T)^{-1} - (\boldsymbol{\eta}\nabla^T)^{-1}| \quad \leq \quad c_2 \cdot |\tilde{\boldsymbol{\eta}}\nabla^T - \boldsymbol{\eta}\nabla^T| \; = \; c_2 \cdot |\boldsymbol{\eta}'\nabla^T| \quad .$$

This implies the *estimate for the continuity equation*, where a time dependent coefficient appears due to the term $\|\tilde{\boldsymbol{v}}\nabla^T\|_{L^\infty(\Omega_F)}$ and the assumption $Dv \in L^2(0,T;L^\infty(\Omega_F))$ of the theorem:

For each $\bar{c}_2 > 0$ *there exists a constant* $c_3(t) \in L^2(0,T)$, *such that*

$$\frac{d}{dt}\int_{\Omega_F} |\; \rho' \;|^2 \; d\boldsymbol{x} \quad \leq \quad c_3(t)\int_{\Omega_F} |\rho'|^2 \; + \; |\boldsymbol{\eta}'\nabla^T|^2 \, d\boldsymbol{x} \quad + \quad \bar{c}_2\int_{\Omega_F} |\boldsymbol{v}'\nabla^T|^2 \, d\boldsymbol{x}$$

As mentioned for the energy estimate of the particle path equation, we will later choose a particular $\bar{c}_2$.

Energy estimates for the momentum equation: The time variation of the expression $\int_{\Omega_F} \frac{1}{2}\tilde{\mathcal{D}}\tilde{\rho} \mid \boldsymbol{v}' \mid^2 \, dx$ is estimated, which is obviously related to the kinetic energy of the particles in $\Omega_F(t)$ at time t. As already introduced, $\mathcal{D}(t,\boldsymbol{x}) = det(\boldsymbol{\eta}\nabla^T)$.

$$\frac{d}{dt}\int_{\Omega_F} \frac{1}{2}\tilde{\mathcal{D}}\tilde{\rho} \mid \boldsymbol{v}' \mid^2 \; d\boldsymbol{x} \quad = \quad \int_{\Omega_F} \frac{1}{2}\tilde{\mathcal{D}}_t\tilde{\rho} \mid \boldsymbol{v}' \mid^2 + \frac{1}{2}\tilde{\mathcal{D}}\tilde{\rho}_t \mid \boldsymbol{v}' \mid^2 + \tilde{\mathcal{D}}\tilde{\rho} \cdot \boldsymbol{v}'^T\boldsymbol{v}'_t \quad d\boldsymbol{x} \qquad (3.4)$$

The first two terms on the right side are easily controlled by the methods already used for the continuity equation. In the sequel, we focus on the third term, for which we obtain (using the $\tilde{a}\tilde{b}$-rule) the following expression for $\tilde{\rho}\boldsymbol{v}'_t$ from the momentum equation:

$$\tilde{\rho}\tilde{\boldsymbol{v}}_t - \rho\boldsymbol{v}_t = \tilde{S}\nabla^T \mathbin{8} (\tilde{\boldsymbol{\eta}}\nabla^T)^{-1} - S\nabla^T \mathbin{8} (\boldsymbol{\eta}\nabla^T)^{-1} \quad \text{and} \quad \tilde{\rho}\tilde{\boldsymbol{v}}_t - \rho\boldsymbol{v}_t = \tilde{\rho}\boldsymbol{v}'_t + \rho'\boldsymbol{v}_t \, ,$$

---

[5] We choose $\mathcal{M} := \{A \in \mathbb{R}^{n\times n} : det\, A \geq \mathcal{D}_* \; and \; |A| \leq M := max\,[\|\boldsymbol{\eta}\nabla^T\|_{L^\infty(Q_T)}, \; \|\tilde{\boldsymbol{\eta}}\nabla^T\|_{L^\infty(Q_T)}]\}$. For $A = [a_{ij}] \in \mathcal{M}$, from the equivalence of norms, $max|a_{ij}| \leq K_1|A| \leq K_1M$ and using Cramer's rule ($n = 3$ for simplicity): $|A^{-1}|^2 = (det\, A)^{-2} \cdot [(a_{22}a_{33} - a_{32}a_{23})^2 + ... \,] \;\leq\; \mathcal{D}_*^{-2}K_2 \cdot \sum_{ijlm} a_{ij}^2 a_{lm}^2 \;\leq\; \mathcal{D}_*^{-2}K_2K_1^2M^2 \cdot \sum_{ijlm} a_{ij}^2 \;\leq\; K_3^2|A|^2$.

[6] This is inequality (2.15) in [55]. We have (for the local Lipschitz continuity of matrix inversion, we refer to [67], p.110): $|\tilde{A}^{-1} - A^{-1}| \;=\; |\tilde{A}^{-1}(A - \tilde{A})A^{-1}| \;\leq\; K_3M \cdot |A - \tilde{A}| \cdot K_3M \quad \forall\, \tilde{A}, A \in \mathcal{M}$, hence $c_2 = K_3^2M^2$.

so that

$$\int_{\Omega_F} \tilde{\mathcal{D}}\tilde{\rho}\cdot \boldsymbol{v}'^T \boldsymbol{v}'_t \, d\boldsymbol{x} \quad = \quad \int_{\Omega_F} -\tilde{\mathcal{D}}\rho' \cdot \boldsymbol{v}'^T \boldsymbol{v}_t \quad +$$

$$+\, \boldsymbol{v}'^T \cdot [\tilde{\mathcal{D}}(\tilde{S}\nabla^T) \overset{\circ}{\circ} (\tilde{\boldsymbol{\eta}}\nabla^T)^{-1} - \mathcal{D}(S\nabla^T) \overset{\circ}{\circ} (\boldsymbol{\eta}\nabla^T)^{-1} - \mathcal{D}'(S\nabla^T) \overset{\circ}{\circ} (\boldsymbol{\eta}\nabla^T)^{-1}]\, d\boldsymbol{x}\,.$$

Here, $\mathcal{D}'(t,\boldsymbol{x}) := \tilde{\mathcal{D}}(t,\boldsymbol{x}) - \mathcal{D}(t,\boldsymbol{x})$. By product differentiation,

$$[\mathcal{D}S(\boldsymbol{\eta}\nabla^T)^{-T}]\nabla \;=\; (S\nabla^T) \overset{\circ}{\circ} [\mathcal{D}(\boldsymbol{\eta}\nabla^T)^{-1}] \;+\; S[(\mathcal{D}(\boldsymbol{\eta}\nabla^T)^{-T})\nabla]$$

and Cramer's rule yields $(\mathcal{D}(\boldsymbol{\eta}\nabla^T)^{-T})\nabla = 0$. Therefore, we can write

$$\int_{\Omega_F} \tilde{\mathcal{D}}\tilde{\rho}\cdot \boldsymbol{v}'^T \boldsymbol{v}'_t \, d\boldsymbol{x} \quad =$$

$$= \quad \int_{\Omega_F} -\tilde{\mathcal{D}}\rho' \cdot \boldsymbol{v}'^T \boldsymbol{v}_t \;+\; \boldsymbol{v}'^T \cdot [J'\nabla] \;-\; \boldsymbol{v}'^T \cdot [\mathcal{D}'(S\nabla^T) \overset{\circ}{\circ} (\boldsymbol{\eta}\nabla^T)^{-1}] \quad d\boldsymbol{x}$$

with $J' := \tilde{\mathcal{D}}\tilde{S}(\tilde{\boldsymbol{\eta}}\nabla^T)^{-T} - \mathcal{D}S(\boldsymbol{\eta}\nabla^T)^{-T}$. Another product differentiation leads to

$$\int_{\Omega_F} \tilde{\mathcal{D}}\tilde{\rho}\cdot \boldsymbol{v}'^T \boldsymbol{v}'_t \, d\boldsymbol{x} \quad = \quad \int_{\Omega_F} -\tilde{\mathcal{D}}\rho' \cdot \boldsymbol{v}'^T \boldsymbol{v}_t \quad +$$

$$+ \quad [\boldsymbol{v}'^T J']\nabla \quad - \quad (\boldsymbol{v}'\nabla^T)^T : \, J' \quad - \quad \boldsymbol{v}'^T \cdot [\mathcal{D}'(S\nabla^T) \overset{\circ}{\circ} (\boldsymbol{\eta}\nabla^T)^{-1}] \quad dx,$$

and Gauss' theorem combined with the boundary values $\boldsymbol{v}' = 0$ on $\Gamma_A \quad (\partial\Omega_F = \Gamma_A \cup \Gamma_{FS})$ yields

$$\int_{\Omega_F} \tilde{\mathcal{D}}\tilde{\rho}\cdot \boldsymbol{v}'^T \boldsymbol{v}'_t \, d\boldsymbol{x} \quad = \quad \int_{\Omega_F} -\,\tilde{\mathcal{D}}\rho' \cdot \boldsymbol{v}'^T \boldsymbol{v}_t \;-\; (\boldsymbol{v}'\nabla^T)^T : \, J' \,+$$

$$-\, \boldsymbol{v}'^T \cdot [\mathcal{D}'(S\nabla^T) \overset{\circ}{\circ} (\boldsymbol{\eta}\nabla^T)^{-1}] \quad d\boldsymbol{x} \quad + \quad \int_{\Gamma_{FS}} \boldsymbol{v}'^T J' \boldsymbol{n} \quad ds\;.$$

Recalling with the definition of J', we see that the boundary integral contains only terms appearing in the interface conditions. Adding this identity to the energy estimate of the plate already eliminates the integrals over the interface Γ_{FS}.

Applying the $\tilde{a}\tilde{b}$-rule to J' in the integral over Ω_F, finally leads to

$$\int_{\Omega_F} \tilde{\mathcal{D}}\tilde{\rho}\cdot \boldsymbol{v}'^T \boldsymbol{v}'_t \, d\boldsymbol{x} \quad = \quad \int_{\Omega_F} -\,\tilde{\mathcal{D}}\rho' \cdot \boldsymbol{v}'^T \boldsymbol{v}_t \;-\; \boldsymbol{v}'^T \cdot [\mathcal{D}'(S\nabla^T) \overset{\circ}{\circ} (\boldsymbol{\eta}\nabla^T)^{-1}] \quad +$$

$$-\,(\boldsymbol{v}'\nabla^T)^T : \, [S'\tilde{\mathcal{D}}(\tilde{\boldsymbol{\eta}}\nabla^T)^{-T} + S\mathcal{D}'(\tilde{\boldsymbol{\eta}}\nabla^T)^{-T} + S\mathcal{D}Q'^T] \quad d\boldsymbol{x} \quad +$$

$$+ \quad \int_{\Gamma_{FS}} \boldsymbol{v}'^T J' \boldsymbol{n} \quad ds \tag{3.5}$$

with $S' := \tilde{S} - S$.

The main task in the remaining part of the proof is the elimination of $\boldsymbol{v}'\nabla^T$ from the energy estimate. The goal is to obtain an estimate of the form

$$\left(\frac{d}{dt}\int_{\Omega_F} energies \quad d\boldsymbol{x}\right) \quad + \quad c_o\int_{\Omega_F} |\boldsymbol{v}'\nabla^T|^2\, d\boldsymbol{x} \quad \leq$$

$$\leq \quad \int_{\Omega_F} energies \quad d\boldsymbol{x} \quad + \quad c_o\int_{\Omega_F} |\boldsymbol{v}'\nabla^T|^2\, d\boldsymbol{x} \quad + \quad \int_{\Gamma_{FS}} \boldsymbol{v}'^T J'\boldsymbol{n} \quad ds \tag{3.6}$$

after adding all energy estimates of the fluid. $\int_{\Omega_F} |\boldsymbol{v}'\nabla^T|^2\; dx$ was already obtained on the right-hand sides of the estimates for the particle path and the continuity equation and weighted with arbitrary constants. In order to obtain $c_o\int_{\Omega_F} |\boldsymbol{v}'\nabla^T|^2\; d\boldsymbol{x}$ on the left-hand side of (3.6), we insert the constitutive equation for S and split in (3.5) according to

$$-(\boldsymbol{v}'\nabla^T)^T : \; [S'\tilde{\mathcal{D}}(\tilde{\boldsymbol{\eta}}\nabla^T)^{-T}] \; = \; -\,\tilde{\mathcal{D}}\cdot\beta \; + \; \gamma \tag{3.7}$$

which will lead on the following four pages to the estimate

$$\int_{\Omega_F} \tilde{\mathcal{D}}\cdot\beta \quad d\boldsymbol{x} \quad \geq \quad c_o\int_{\Omega_F} |\boldsymbol{v}'\nabla^T|^2\, d\boldsymbol{x} \quad - \quad c_4\int_{\Omega_F} |\boldsymbol{v}'|^2\, dx \tag{3.8}$$

with $c_o, c_4 > 0$. The remaining free constants (those with the bars, such as $\bar{c}_2$ in the estimate for the continuity equation) have to be chosen so that they add up and let c_o appear on the right-hand side of (3.6) as-well.

We have

$$\begin{aligned} S \quad = \quad & -\pi(\rho,\theta)\cdot I + \mu\cdot[(\boldsymbol{v}\nabla^T)(\boldsymbol{\eta}\nabla^T)^{-1} + (\boldsymbol{\eta}\nabla^T)^{-T}(\boldsymbol{v}\nabla^T)^T] \quad + \\ & + \quad (\zeta - \frac{2}{3}\mu)\cdot(\boldsymbol{v}\nabla^T) : (\boldsymbol{\eta}\nabla^T)^{-1}\cdot I\,, \end{aligned}$$

and using the $\tilde{a}\tilde{b}$-rule and $\pi'(t,\boldsymbol{x}) := \pi(\tilde{\rho}(t,\boldsymbol{x}),\tilde{\theta}(t,\boldsymbol{x})) - \pi(\rho(t,\boldsymbol{x}),\theta(t,\boldsymbol{x}))$,

$$S' \; = \; -\pi'\cdot I \; + \; \mu\cdot[(v\nabla^T)Q' + (\boldsymbol{v}'\nabla^T)(\tilde{\boldsymbol{\eta}}\nabla^T)^{-1} + Q'(v\nabla^T)^T +$$

$$+(\tilde{\boldsymbol{\eta}}\nabla^T)^{-T}(\boldsymbol{v}'\nabla^T)^T] \; + \; (\zeta - \frac{2}{3}\,\mu)\cdot[(v\nabla^T) : Q' + (v\nabla^T) : (\tilde{\boldsymbol{\eta}}\nabla^T)^{-1}]\cdot I\;.$$

Moreover, using this identity the splitting (3.7) is carried out as follows,

$$\begin{aligned} \beta \quad := \quad & (\boldsymbol{v}'\nabla^T)^T : \; [\{\; \mu(\boldsymbol{v}'\nabla^T)(\tilde{\boldsymbol{\eta}}\nabla^T)^{-1} \; + \; \mu(\tilde{\boldsymbol{\eta}}\nabla^T)^{-T}(\boldsymbol{v}'\nabla^T)^T \quad + \\ & + \quad (\zeta - \frac{2}{3}\,\mu)\cdot(\boldsymbol{v}\nabla^T) : (\tilde{\boldsymbol{\eta}}\nabla^T)^{-1}\cdot I\;\}\cdot(\tilde{\boldsymbol{\eta}}\nabla^T)^{-T}] \end{aligned}$$

$$\gamma \quad := \quad -(\boldsymbol{v}'\nabla^T)^T : \; [\,\tilde{\mathcal{D}}\cdot\{-\pi'\cdot I \; + \; \mu(\boldsymbol{v}\nabla^T)Q' \; + \; \mu Q'(\boldsymbol{v}\nabla^T)^T \quad +$$

$$+ \quad (\zeta - \frac{2}{3}\,\mu) \cdot (\boldsymbol{v}\nabla^T) : Q' \cdot I \,\} \cdot (\tilde{\boldsymbol{\eta}}\nabla^T)^{-T}] \,.$$

Next we show the estimate (3.8). We abbreviate the matrix fields $A := \boldsymbol{v}'\nabla^T$, $B := (\tilde{\boldsymbol{\eta}}\nabla^T)^{-1}$, and because of the identity

$$A^T : [(AB + B^T A^T)B^T] = [B^T A^T] : (AB + B^T A^T) =$$
$$= \frac{1}{2}(AB + B^T A^T) : (AB + B^T A^T) =$$
$$= \frac{1}{2}(AB + B^T A^T)^T : (AB + B^T A^T) = \frac{1}{2}|(AB + B^T A^T)|^2 \,,$$

(cf. [28], p.6), β has the form

$$\begin{aligned} \beta \quad &= \quad \frac{\mu}{2} \mid (\boldsymbol{v}'\nabla^T)(\tilde{\boldsymbol{\eta}}\nabla^T)^{-1} + (\tilde{\boldsymbol{\eta}}\nabla^T)^{-T}(\boldsymbol{v}'\nabla^T)^T|^2 \quad + \\ &+ \quad (\zeta - \frac{2}{3}\mu) \; [\; (v\nabla^T) : (\boldsymbol{\eta}\nabla^T)^{-1}]^2 \quad = \\ &= \quad \frac{\mu}{2} \, |AB + B^T A^T|^2 \quad + \quad \left(\zeta - \frac{2\mu}{3}\right) \; [A : B]^2 \,. \end{aligned}$$

The first step towards the proof of (3.8) is the following estimate which is independent of the form of the square matrices A, B, but holds for dimensions $n = 2, 3$ only,

$$\beta \quad \geq \quad min\left(\frac{\mu}{2}, \frac{3\zeta}{4}\right) \cdot |AB + B^T A^T|^2 \,. \tag{3.9}$$

In the case $\zeta - \frac{2}{3}\mu \geq 0$, we have $\frac{\mu}{2} = min\left(\frac{\mu}{2}, \frac{3\zeta}{4}\right)$, so that (3.9) follows immediately. The case $\zeta - \frac{2}{3}\mu < 0$ is a little more difficult. To this end, let

$$A = \begin{pmatrix} A_1 \\ A_2 \\ \vdots \\ A_n \end{pmatrix} \qquad \text{und} \quad B = (B_1, B_2, \cdots, B_n) \;,$$

in other words, A_i respectively B_i are the columns of A respectively B. We have[7]

$$\begin{aligned} [A : B]^2 \; &= \; \left[\sum_{i=1}^{n} A_i B_i\right]^2 \; = \; \sum_{i=1}^{n}(A_i B_i)^2 \quad + \\ &+ \; 2 \sum_{1\leq i<j\leq n} A_i B_i \cdot A_j B_j \quad \leq \quad n \, \sum_{i=1}^{n}(A_i B_i)^2 \,. \end{aligned}$$

---

[7] Using $C := AB$, (3.9) can be shown entirely with C. In this case, $A : B = traceC$ and $A_i B_j = c_{ij}$.

Hence, only for $n = 2$ or 3 $\quad [A:B]^2 \;\leq\; 3\sum_{i=1}^n (A_iB_i)^2 \quad$ holds. In addition,

$$\begin{aligned} |AB + B^TA^T|^2 \;&=\; 2(AB):(AB) + 2(AB):(B^TA^T) \;= \\ &=\; 2\sum_{i,j=1}^n (A_iB_j)\cdot(A_jB_i) \;+\; 2\sum_{i,j=1}^n (A_iB_j)^2 \;= \\ &=\; 4\sum_{i=1}^n (A_iB_i)^2 \quad+\quad 2\sum_{1\leq i<j\leq n} (A_iB_j + A_jB_i)^2 \;. \end{aligned}$$

Therefore, we have

$$|AB + B^TA^T|^2 \;-\; 4\sum_{i=1}^n (A_iB_i)^2 \;\geq\; 0\;.$$

Together with $\dfrac{3\zeta}{4} = min\left(\dfrac{\mu}{2}, \dfrac{3\zeta}{4}\right)$,

$$\begin{aligned} \beta \;&\geq\; \frac{3\zeta}{4}\left[|AB + B^TA^T|^2 \;-\; 4\sum_{i=1}^n (A_iB_i)^2\right] \quad+ \\ &+\; \frac{\mu}{2}\left[4\sum_{i=1}^n (A_iB_i)^2\right] \quad+\quad \left(\zeta - \frac{2\mu}{3}\right)\;[A:B]^2 \quad\geq \\ &\geq\; \frac{3\zeta}{4}\left[|AB + B^TA^T|^2 \;-\; 4\sum_{i=1}^n (A_iB_i)^2\right] \quad+ \\ &+\; \frac{\mu}{2}\left[4\sum_{i=1}^n (A_iB_i)^2\right] \quad+\quad 3\left(\zeta - \frac{2\mu}{3}\right)\;\sum_{i=1}^n (A_iB_i)^2 \end{aligned}$$

follows, where the last estimate is correct because of $\quad \zeta - \dfrac{2\mu}{3} < 0 \quad$. Thus, (3.9) is proven. This means that we have reached

$$\int_{\Omega_F} \tilde{\mathcal{D}}\cdot\beta \quad d\boldsymbol{x} \quad\geq\quad c_5\int_{\Omega_F} \tilde{\mathcal{D}} \;\cdot\; |\;(\boldsymbol{v}'\nabla^T)(\tilde{\boldsymbol{\eta}}\nabla^T)^{-1} + \;(\tilde{\boldsymbol{\eta}}\nabla^T)^{-T}(\boldsymbol{v}'\nabla^T)^T\;|^2 \quad d\boldsymbol{x} \qquad (3.10)$$

with $\;c_5 = min\left(\dfrac{\mu}{2}, \dfrac{3}{4\zeta}\right) > 0\;$. The step from (3.10) to (3.8) utilizes Korn's inequality (cf. [32], theorem 3.4, page 84):

Let $\Omega \subseteq \mathbb{R}^3$ be a connected domain with Lipschitz boundary, and for $w \in W^{1,2}(\Omega)$ define $D(w) := \frac{1}{2}[(w\nabla^T) + (w\nabla^T)^T]$. There is a constant $C(\Omega) > 0$ so that

$$\|w\|^2_{W^{1,2}(\Omega)} \quad\leq\quad C(\Omega)\cdot\int_\Omega |w|^2 + |D(w)|^2\;dy \quad\; \forall\, w \in W^{1,2}(\Omega)\;.$$

Defining $w(t,y) := \boldsymbol{v}'(t, \tilde{\boldsymbol{\eta}}^{-1}(t,y))$ on $\tilde{\Omega}_A(t) := \tilde{\boldsymbol{\eta}}(t,\Omega_F)$, where $\tilde{\boldsymbol{\eta}}^{-1}(t,y)$ is the inverse of the mapping

$$\tilde{\boldsymbol{\eta}}(t,\cdot) : \Omega_F \to \tilde{\Omega}_A(t), \; x \mapsto \tilde{\boldsymbol{\eta}}(t,\boldsymbol{x}) \quad \text{for fixed } t,$$

we immediately see that $\int_{\tilde{\Omega}_A(t)} 4 \cdot |D(w)|^2 \, dy$ is precisely the integral on the right-hand side of (3.10). We know that Korn's inequality is valid for $\Omega = \Omega_F$. $\tilde{\boldsymbol{\eta}}^{-1}(t,\cdot)$ maps $\tilde{\Omega}_A(t)$ to Ω_F, where the regularity conditions of the theorem imply that[8]

$$\|\tilde{\boldsymbol{\eta}}^{-1}(t,y)\|_{H^{2,\infty}(\tilde{\Omega}_A(t))} \quad \text{on} \quad [0,T] \quad \text{uniformly bounded}$$

$$\text{and} \quad det[\tilde{\boldsymbol{\eta}}^{-1}\nabla_y^T] \geq d_* > 0 \quad \text{for all} \quad (t,y) \quad \text{with} \quad t \in [0,T], \; y \in \tilde{\Omega}_A(t) \, .$$

The procedure in [51] (pages 95/96) yields a constant independent of t such that[9]

$$\int_{\tilde{\Omega}_A(t)} |w|^2 + |w\nabla_y^T|^2 \, dy \quad \leq \quad c_6 \cdot \int_{\tilde{\Omega}_A(t)} |w|^2 + |D(w)|^2 \, dy$$

$$\forall \, t \in [0,T], \; w \in W^{1,2}(\tilde{\Omega}_A(t)) \, .$$

Using the substitution $w(t,y) := \boldsymbol{v}'(t, \tilde{\boldsymbol{\eta}}^{-1}(t,y))$, we obtain

$$\int_{\Omega_F} \frac{1-c_6}{c_6} \, \tilde{\mathcal{D}} \, |\boldsymbol{v}'|^2 \; + \; \frac{1}{c_6} \, \tilde{\mathcal{D}} \, | \, (\boldsymbol{v}'\nabla^T)(\tilde{\boldsymbol{\eta}}\nabla^T)^{-1} \, |^2 \quad d\boldsymbol{x} \quad \leq$$

$$\leq \quad \frac{1}{4} \int_{\Omega_F} \tilde{\mathcal{D}} \, \cdot \, | \, (\boldsymbol{v}'\nabla^T)(\tilde{\boldsymbol{\eta}}\nabla^T)^{-1} + \, (\tilde{\boldsymbol{\eta}}\nabla^T)^{-T}(\boldsymbol{v}'\nabla^T)^T \, |^2 \quad d\boldsymbol{x} \quad \forall \, t$$

and, with A, B as above, we have

$$| \, (\boldsymbol{v}'\nabla^T)(\tilde{\boldsymbol{\eta}}\nabla^T)^{-1} \, |^2 \; = \; trace(ABB^TA^T) \; = \; \sum_{i=1}^n A_i BB^T A_i^T \; \geq$$

$$\geq \quad \frac{1}{c_7^2} \sum_{i=1}^n |A_i|^2 \quad = \quad \frac{1}{c_7^2} \, |A|^2 \quad = \quad \frac{1}{c_7^2} \, |\boldsymbol{v}'\nabla^T|^2 \, ,$$

where $|B^{-1}| = |\tilde{\boldsymbol{\eta}}\nabla^T| \leq c_7$, with a suitable constant $c_7 > 0$, because of $D\boldsymbol{\eta} \in L^\infty(Q_T)$. Alltogether, we have

$$c_5 \int_{\Omega_F} \tilde{\mathcal{D}} \, \cdot \, | \, (\boldsymbol{v}'\nabla^T)(\tilde{\boldsymbol{\eta}}\nabla^T)^{-1} + \, (\tilde{\boldsymbol{\eta}}\nabla^T)^{-T}(\boldsymbol{v}'\nabla^T)^T \, |^2 \quad d\boldsymbol{x} \quad \geq$$

$$\geq \quad c_o \int_{\Omega_F} |\boldsymbol{v}'\nabla^T|^2 \, d\boldsymbol{x} \quad - \quad c_4 \int_{\Omega_F} |\boldsymbol{v}'|^2 \, d\boldsymbol{x}$$

---

[8] To this end, $(\boldsymbol{\eta}\nabla^T)^{-1}$ is determined using Cramer's rule, the rule for differentiation of inverses ([67], p. 119) is used, and finally the particle path equation and the regularity of $\boldsymbol{\eta}$ and v is applied.

[9] The constants $\alpha, \beta, \gamma, \epsilon$ on page 96 in [51] can be chosen independent of t because of the properties of $\tilde{\boldsymbol{\eta}}^{-1}$.

with the constants $c_4 := 4\,\mathcal{D}_* c_5 (c_6 - 1)/c_6 > 0$ and $c_o := 4\,\mathcal{D}_* c_5/(c_6 c_7^2) > 0$. Together with (3.10), (3.8) follows. From (3.4), (3.5), (3.7) and the definition of γ, we see that

$$\begin{aligned}
\frac{d}{dt} \int_{\Omega_F} \frac{1}{2} \tilde{\mathcal{D}} \tilde{\rho} \mid \boldsymbol{v}' \mid^2 \; d\boldsymbol{x} \quad &= \quad \int_{\Omega_F} \frac{1}{2} \tilde{\mathcal{D}}_t \tilde{\rho} \mid \boldsymbol{v}' \mid^2 + \frac{1}{2} \tilde{\mathcal{D}} \tilde{\rho}_t \mid \boldsymbol{v}' \mid^2 + \\
&+ \tilde{\mathcal{D}} \rho' \cdot \boldsymbol{v}'^T \boldsymbol{v}_t \; - \; \boldsymbol{v}'^T \cdot [\mathcal{D}'(S\nabla^T) \between (\boldsymbol{\eta}\nabla^T)^{-1}] \; - \; \tilde{\mathcal{D}} \beta \\
&- (\boldsymbol{v}'\nabla^T)^T : \; [S\mathcal{D}'(\tilde{\boldsymbol{\eta}}\nabla^T)^{-T} \; + \; S\mathcal{D}Q'^T \; + \; \tilde{\mathcal{D}} \cdot \{-\pi' \cdot I \; + \; \mu(\boldsymbol{v}\nabla^T)Q' + \\
&+ \mu Q'(v\nabla^T)^T \; + \; (\zeta - \frac{2}{3}\mu) \cdot (v\nabla^T) : Q' \cdot I \; \} \cdot (\tilde{\boldsymbol{\eta}}\nabla^T)^{-T}] \quad d\boldsymbol{x} \quad + \\
&+ \int_{\Gamma_{FS}} \boldsymbol{v}'^T J' \boldsymbol{n} \quad ds \; .
\end{aligned}$$

All summands in the integral over Ω_F (after performing all matrix-vector-multiplications) have the form $a'b'c$, and we use $2|a'b'c| \le |c| \cdot (\epsilon^2 a^2 + \epsilon^{-2} b^2)$, where we need $\epsilon \neq 1$ only if a' or b' are components of $\boldsymbol{v}'\nabla^T$. The more, we use (3.8) now and need the Lipschitz continuity of π for estimating $\pi' = \pi(\tilde{\rho}, \tilde{\theta}) - \pi(\rho, \theta)$, and the Lipschitz continuity of the determinant[10] for estimating $\mathcal{D}' := det(\tilde{\boldsymbol{\eta}}\nabla^T) - det(\boldsymbol{\eta}\nabla^T)$. Using the definition of J', we obtain the *energy estimate of the momentum equation*:

$$\begin{aligned}
&\frac{d}{dt} \int_{\Omega_F} \frac{1}{2} \tilde{\mathcal{D}} \tilde{\rho} |\boldsymbol{v}'|^2 \, d\boldsymbol{x} \quad + \quad c_o \int_{\Omega_F} |\boldsymbol{v}'\nabla^T|^2 \, d\boldsymbol{x} \quad \le \\
&\le \quad c_8(t) \int_{\Omega_F} \frac{1}{2} \tilde{\mathcal{D}} \tilde{\rho} |\boldsymbol{v}'|^2 \; + \; |\rho'|^2 \; + \; \frac{1}{2} \tilde{\mathcal{D}} \tilde{\rho} \tilde{c}_v |\theta'|^2 \; + \; |\boldsymbol{\eta}'\nabla^T|^2 \quad d\boldsymbol{x} \quad + \\
&+ \quad \frac{c_o}{2} \int_{\Omega_F} |\boldsymbol{v}'\nabla^T|^2 \, d\boldsymbol{x} \quad + \quad \int_{\Gamma_{FS}} \boldsymbol{v}'^T \left[\tilde{\mathcal{D}} \tilde{S} (\tilde{\boldsymbol{\eta}}\nabla^T)^{-T} - \mathcal{D} S (\boldsymbol{\eta}\nabla^T)^{-T} \right] \boldsymbol{n} \quad ds
\end{aligned}$$

with[11] $\quad c_8(t) \in L^2(0,T)$

In order to understand the rest of the proof, we assume temporarily that we have an isothermic fluid model, i.e. we use a pressure equation of the form $\pi = \pi(\rho)$ and may discard the temperature equation. In this case, the term $\frac{1}{2}\tilde{\mathcal{D}}\tilde{\rho}\tilde{c}_v|\theta'|^2$ does not appear in the quantity $E(t)$ as defined at the beginning of the proof. Adding all estimates found so far and using the interface conditions yields

---

[10] explicit computation of the determinat yields ($n = 3$ for simplicity): $|det\ \tilde{A} - det\ A| \; = \; |\ \tilde{a}_{11}\tilde{a}_{22}\tilde{a}_{33} - a_{11}a_{22}a_{33} + ... \ | \; = \; |\ (\tilde{a}_{11} - a_{11})\tilde{a}_{22}\tilde{a}_{33} + a_{11}(\tilde{a}_{22} - a_{22})\tilde{a}_{33} + a_{11}a_{22}(\tilde{a}_{33} - a_{33}) + ... \ | \; \le \; \sum_{i,j} |\tilde{a}_{ij} - a_{ij}| \cdot K_{ij} K_1^2 M^2$, hence $|det\ \tilde{A} - det\ A|^2 \le K_4 |\tilde{A} - A|^2$ for $\tilde{A}, A \in \mathcal{M}$. Here, the $\tilde{a}\tilde{b}$-rule was used, and the K_{ij} are fixed constants necessary since some matrix entries appear once, others multiple times in the determinant formula.

[11] From the assumptions in [55] we can deduce $\boldsymbol{v}_t \in L^1(0,T; L^\infty(\Omega_F))$ and get $c_8(t) \in L^1(0,T)$ due to the term $\tilde{\mathcal{D}}\rho' \cdot \boldsymbol{v}'^T \boldsymbol{v}_t$. Similar consequences result from $(S\nabla^T) \between (\boldsymbol{\eta}\nabla^T)^{-1}$.

$$\frac{d}{dt}\left[\frac{1}{2}\int_{\Omega_S} {w_t'}^2+\alpha|w_t'\nabla|^2+\beta(\Delta w')^2\,d(x_1,x_2)\quad+\right.$$

$$\left.\int_{\Omega_F}|\boldsymbol{\eta}'|^2+\,|\boldsymbol{\eta}'\nabla^T|^2+\,|\rho'|^2\,+\,\frac{1}{2}\tilde{\mathcal{D}}\tilde{\rho}|\boldsymbol{v}'|^2\,d\boldsymbol{x}\right]$$

$$\leq\quad c_9(t)\left[\frac{1}{2}\int_{\Omega_S} {w_t'}^2+\alpha|w_t'\nabla|^2+\beta(\Delta w')^2\,d(x_1,x_2)\quad+\right.$$

$$\left.\int_{\Omega_F}|\boldsymbol{\eta}'|^2+\,|\boldsymbol{\eta}'\nabla^T|^2+\,|\rho'|^2\,+\,\frac{1}{2}\tilde{\mathcal{D}}\tilde{\rho}|\boldsymbol{v}'|^2\,d\boldsymbol{x}\right].$$

All $|\boldsymbol{v}'\nabla^T|^2$-integrals disappeared due to the choice $\overline{c}_1=\overline{c}_2=c_o/4$; and we have $c_9(t)\in L^2(0,T)$. Integration over time intervals $(0,t)$, $t\leq T$ and application of Gronwall's lemma finally leads to $u'=\rho'=\boldsymbol{v}'=\boldsymbol{\eta}'=0$, hence uniqueness.

We also present the most important steps for obtaining the estimate of the energy equation, or temperature equation, due to the form we have put it in. Again, simple estimation techniques and partial integration are sufficient. In contrast to [55], we estimate the variation of $\int_{\Omega_F}\frac{1}{2}\tilde{\mathcal{D}}\tilde{c}_v|\theta'|^2\,d\boldsymbol{x}$, which is obiously related to the internal energy of the fluid with $\tilde{c}_v(t,\boldsymbol{x}):=c_v(\tilde{\theta}(t,\boldsymbol{x}))$.

Energy estimate for the temperature equation: Differentiating $\frac{d}{dt}\int_{\Omega_F}\frac{1}{2}\tilde{\rho}\tilde{c}_v\tilde{\mathcal{D}}|\theta'|^2\,d\boldsymbol{x}$ leads to the expression $\int_{\Omega_F}\tilde{\rho}\tilde{c}_v\tilde{\mathcal{D}}\theta'\theta_t'\,dx$, which is examined further. The $\tilde{a}\tilde{b}$-rule gives

$$(\tilde{\rho}\tilde{c}_v\tilde{\mathcal{D}})\tilde{\theta}_t-(\rho c_v\mathcal{D})\theta_t\;=\;\tilde{\rho}\tilde{c}_v\tilde{\mathcal{D}}\theta_t'+(\tilde{\rho}\tilde{c}_v\tilde{\mathcal{D}}-\rho c_v\mathcal{D})\theta_t$$

and in combination with the temperature equation we obtain

$$\begin{aligned}\tilde{\rho}\tilde{c}_v\tilde{\mathcal{D}}\theta'\theta_t'\quad&=\quad\theta'[\tilde{\mathcal{D}}\tilde{S}:\tilde{D}-\mathcal{D}S:D]\;-\;\theta'[\tilde{\mathcal{D}}(\tilde{q}\nabla^T):(\tilde{\boldsymbol{\eta}}\nabla^T)^{-1}+\\&\qquad-\,\mathcal{D}(q\nabla^T):(\boldsymbol{\eta}\nabla^T)^{-1}]\;-\;(\tilde{\rho}\tilde{c}_v\tilde{\mathcal{D}}-\rho c_v\mathcal{D})\theta'\theta_t\end{aligned}$$

where $q=-\kappa[(\boldsymbol{\eta}\nabla^T)^{-T}(\theta\nabla)]$. The product rule yields

$$\mathcal{D}(q\nabla^T):(\boldsymbol{\eta}\nabla^T)^{-1}\;=\;[q^T\mathcal{D}(\boldsymbol{\eta}\nabla^T)^{-T}]\nabla\;-\;q^T[(\mathcal{D}(\boldsymbol{\eta}\nabla^T)^{-T})\nabla]\,.$$

Again, the last summand on the right-hand side vanishes due to Cramer's rule, and another product differentiation leads to

$$\theta'\left[[q^T\mathcal{D}(\boldsymbol{\eta}\nabla^T)^{-T}]\nabla\right]\;=\;[\theta'q^T\mathcal{D}(\boldsymbol{\eta}\nabla^T)^{-T}]\nabla\;-\;[q^T\mathcal{D}(\boldsymbol{\eta}\nabla^T)^{-T}](\theta'\nabla)\,.$$

Therefore,

$$\int_{\Omega_F}\tilde{\rho}\tilde{c}_v\tilde{\mathcal{D}}\theta'\theta_t'\,d\boldsymbol{x}\quad=\quad\int_{\Omega_F}\theta'[\tilde{\mathcal{D}}\tilde{S}:\tilde{D}-\mathcal{D}S:D]\quad+$$

$$- (\tilde{\rho}\tilde{c}_v\tilde{\mathcal{D}} - \rho c_v\mathcal{D})\theta'\theta_t \ + \ [\tilde{q}^T\tilde{\mathcal{D}}(\tilde{\boldsymbol{\eta}}\nabla^T)^{-T} \ - \ q^T\mathcal{D}(\boldsymbol{\eta}\nabla^T)^{-T}](\theta'\nabla) \quad d\boldsymbol{x} \quad +$$

$$- \quad \int_{\partial\Omega_F} \theta' \cdot [\tilde{q}^T\tilde{\mathcal{D}}(\tilde{\boldsymbol{\eta}}\nabla^T)^{-T} \ - \ q^T\mathcal{D}(\boldsymbol{\eta}\nabla^T)^{-T}] \cdot n \quad ds\,.$$

As for the momentum equation, $(\theta'\nabla)$ has to be eliminated. Here, this can be done in a simpler way and independently of the other energy estimates:

$$(\theta'\nabla^T)(\tilde{\boldsymbol{\eta}}\nabla^T)^{-1}(\tilde{\boldsymbol{\eta}}\nabla^T)^{-T}(\theta'\nabla) \ = \ |(\tilde{\boldsymbol{\eta}}\nabla^T)^{-T}(\theta'\nabla)|^2 \ \geq \ \frac{1}{c_7^2}|\theta'\nabla|^2$$

as already seen when deriving the energy estimate for the momentum equation, and by definition of the heat flux vector q,

$$[\ \tilde{q}^T\tilde{\mathcal{D}}(\tilde{\boldsymbol{\eta}}\nabla^T)^{-T} \ - \ q^T\mathcal{D}(\boldsymbol{\eta}\nabla^T)^{-T}](\theta'\nabla) \quad \leq$$

$$\leq \quad - \frac{\tilde{\mathcal{D}}\kappa}{c_7^2}|\theta'\nabla|^2 \ - \ \kappa(\theta\nabla^T)[\tilde{\mathcal{D}}(\tilde{\boldsymbol{\eta}}\nabla^T)^{-1}(\tilde{\boldsymbol{\eta}}\nabla^T)^{-T} - \ \mathcal{D}(\boldsymbol{\eta}\nabla^T)^{-1}(\boldsymbol{\eta}\nabla^T)^{-T}](\theta'\nabla)\,.$$

Simple estimation techniques, as those used when treating the continuity equation, combined with $c_{10} := \mathcal{D}_*\kappa/c_7^2 > 0$, yield the *energy estimate for the temperature equation*:

For each $\bar{c}_3 > 0$ *there exists a function* $c_{11}(t) \in L^1(0,T)$, *such that*

$$\frac{d}{dt}\int_{\Omega_F} \frac{1}{2}\tilde{\rho}\tilde{c}_v\tilde{\mathcal{D}}|\theta'|^2\,d\boldsymbol{x} \quad + \quad c_{10}\int_{\Omega_F} |\theta'\nabla|^2\,d\boldsymbol{x} \quad \leq$$

$$\leq \quad c_{11}(t)\int_{\Omega_F} |\rho'|^2 \ + \ \frac{1}{2}\tilde{\rho}\tilde{c}_v\tilde{\mathcal{D}}|\theta'|^2 \ + \ |\boldsymbol{\eta}'\nabla^T|^2 \quad d\boldsymbol{x} \quad +$$

$$+ \quad \bar{c}_3\int_{\Omega_F} |\boldsymbol{v}'\nabla^T|^2\,d\boldsymbol{x} \quad + \quad c_{10}\int_{\Omega_F} |\theta'\nabla|^2\,d\boldsymbol{x} \quad +$$

$$- \quad \int_{\partial\Omega_F} \theta' \cdot [\tilde{q}^T\tilde{\mathcal{D}}(\tilde{\boldsymbol{\eta}}\nabla^T)^{-T} \ - \ q^T\mathcal{D}(\boldsymbol{\eta}\nabla^T)^{-T}] \cdot n \quad ds$$

The integrand of the boundary integral is zero on the piece $(\partial\Omega_F)_1 \cup (\partial\Omega_F)_3$, and finally the boundary condition on $(\partial\Omega_F)_2$ gives

$$- \int_{\partial\Omega_F} \theta' \cdot [\tilde{q}^T\tilde{\mathcal{D}}(\tilde{\boldsymbol{\eta}}\nabla^T)^{-T} \ - \ q^T\mathcal{D}(\boldsymbol{\eta}\nabla^T)^{-T}] \cdot n\,ds \quad = \quad - \int_{(\partial\Omega_F)_2} k \cdot |\theta'|^2\,ds\,,$$

that is, we have another positive term on the left-hand side of the energy estimate. As for the isothermic case, we show uniqueness by choosing $\bar{c}_1 = \bar{c}_2 = \bar{c}_3 = c_o/6$.

Chapter 4

The Discrete Equations

4.1 High-resolution Finite Volume Discretization for the Euler equations on moving grids

Here we discuss our flow discretization on moving grids using the Finite Volume Method. The use of concepts like upwinding, numerical dissipation and Riemann-Solvers [31], [42], [26] are assumed to be known by the reader, and will therefore not be detailed in the sequel.

4.1.1 The finite volume approach

We recall the Euler equations (2.1) for a moving control volume, now written with the flux (2.2) and integrated from an arbitrary time t^n to $t^{n+1} \equiv t^n + \Delta t$,

$$\int_{\Omega(t^{n+1})} U\,dx \;-\; \int_{\Omega(t^n)} U\,dx \;+\; \int_{t^n}^{t^{n+1}} \int_{\partial\Omega(t)} f(U, \dot{\boldsymbol{x}})\,\boldsymbol{n}\;ds\,dt \;=\; 0\;. \tag{4.1}$$

This equation has to hold for any domain $\Omega(t)$ moving within the fluid domain $\Omega_F(t)$. In many applications the fluid domain reaches up to infinity. For a numerical simulation we only consider a finite moving domain $\Omega_F^C(t)$ containing the area of interest. This introduces artificial boundaries, which are dotted in Fig. 4.1. This choice of a finite *computational domain* Ω_F^C defines a very common situation in CFD, where we have artifical boundaries, the in- and outflow boundaries, from where the fluid is meant to attain the ∞-state away from $\Omega_F^C(t)$. Further the common situation is that $\Omega_F^C(t)$ has also impermeable boundaries which may move, as in our case. Next this finite domain is split into a finite set of moving subdomains, the *cells* $\Omega_i(t)$, such that all $\Omega_i(t)$ are disjoint at each instant of time and that their union gives $\Omega_F^C(t)$.

In a finite volume scheme one denotes the state $U_i(t)$ as the mean value of the conserved quantity U in the cell $\Omega_i(t)$. Abbreviating $U_i^n \equiv U_i(t^n)$ and $\Omega_i^n \equiv \Omega_i(t^n)$ we can rewrite

(4.1) for the cell Ω_i as

$$|\Omega_i^{n+1}|\,U_i^{n+1} \;-\; |\Omega_i^n|\,U_i^n \quad + \quad \int_{t^n}^{t^{n+1}} \int_{\partial\Omega_i(t)} f(U,\dot{\boldsymbol{x}})\,\boldsymbol{n}\;ds\,dt \quad = \quad 0\;. \tag{4.2}$$

So far nothing really has happened, but now we will have to face an approximation. Assuming all the meanvalues U_i^n to be known, we want to know the values U_i^{n+1} at the time t^{n+1}. Here we employ 4 *approximation steps*.

Namely, the *first* is a reconstruction-limitation rule that calculates from all the mean values some higher order representation of U within each cell, reducing to first order at discontinuities. From this representation we are only interested in the values resulting at the cell-edges, for evaluating the boundary integral. The details of the reconstruction and limitation are given in Sec. 4.1.7.

At a point on an edge, we will have two values of U coming from each neighbouring cell, which are different in general. This results in the use of a numerical flux function, which approximates $f\,\boldsymbol{n}$ on the edge due to the two values and is the *second approximation step*. There are many possible choices for a numerical flux function. The ones emloyed here are given in Sec. 4.1.4, their implementation for moving edges in Sec. 4.1.5 and the modification at boundaries in Sec. 4.1.6.

At this point we want to introduce the reconstruction-limitation step and the numerical flux function *formally*. For this purpose, if Ω_i has an edge in common with Ω_j let the edge be denoted by e_{ij}. Let further the outward normal of Ω_i on e_{ij} be denoted by $\boldsymbol{n}_{ij}$, the velocity of e_{ij} by $\dot{\boldsymbol{x}}_{ij}$ and let the value at e_{ij} due to the reconstruction in Ω_i be denoted by U_{ij}. The numerical flux function approximating $f\,\boldsymbol{n}$ on the edge e_{ij} in (4.2) can then be expressed in the form $F(U_{ij}, U_{ji}, \dot{\boldsymbol{x}}_{ij}, \boldsymbol{n}_{ij})$. Thus, from reconstruction, limitation and numerical flux, we formally have an approximation of (4.2) as

$$|\Omega_i^{n+1}|\,U_i^{n+1} \;-\; |\Omega_i^n|\,U_i^n \quad + \quad \int_{t^n}^{t^{n+1}} \sum_{e_{ij}\subset\partial\Omega_i} \int_{e_{ij}} F(U_{ij}, U_{ji}, \dot{\boldsymbol{x}}_{ij}, \boldsymbol{n}_{ij})\;ds\;\;dt \quad = \quad 0\;. \tag{4.3}$$

The *third approximation step* is to replace the surface integrals by quadrature formulas. A simple but important example is given in Sec. 4.1.2.

And the *fourth approximation step* is to use quadrature formulas for the time integral. Then the resulting set of equations may be solved for the mean values U_i^{n+1}. Alternatively, we could also insert the first three approximations into (2.1). To the resulting set of ordinary differential equations we could apply a Runge-Kutta Method, which is then equivalent to what is done here in the fourth step, see [30]. This fourth step interferes with the Geometric Conservation Law, which is discussed is Sec. 4.1.3.

4.1.2 Grid movement and cells with polygonal boundaries

In most CFD-codes for 2D-problems the cells have polygonal boundaries, as implemented in our case, too. Then the edges are straight lines and a quadrature formula for the

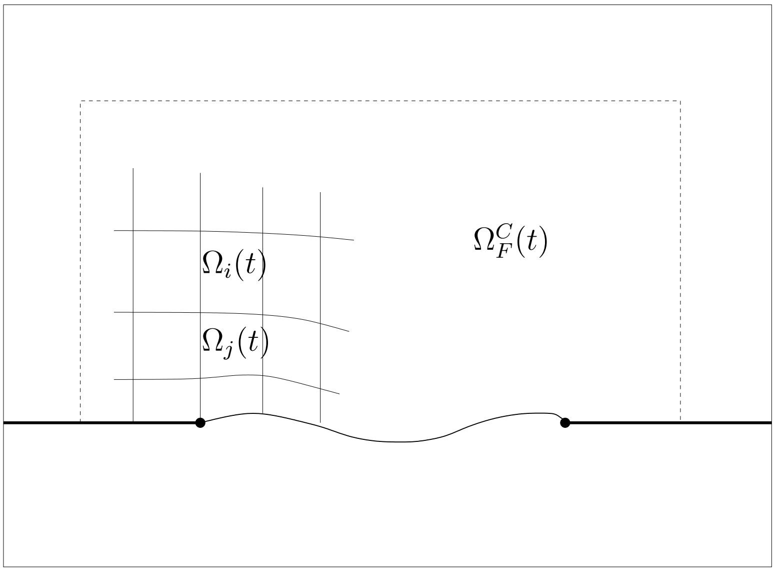

Figure 4.1: Domain of discrete problem and part of the grid

surface integral that is of second order is given by

$$\int_{e_{ij}} F(U_{ij}, U_{ji}, \dot{\boldsymbol{x}}_{ij}, \boldsymbol{n}_{ij})\; ds \quad \approx \quad |e_{ij}| \cdot F(U_{ij,c}, U_{ji,c}, \dot{\boldsymbol{x}}_{ij,c}, \boldsymbol{n}_{ij,c})\;, \tag{4.4}$$

where the c-subscript indicates that all values are taken at the edge center.

The movement of the grid is usually based on the movement of the vertices. A very general approach is to model the vertices as a system of mass points connected by springs along the edges and to solve the spring-mass-system under the constraint that the vertices on the boundary follow the boundary movement. In the case of a simple geometry the vertices may be moved by some analytically given stretching rule, which is how the grid movement for the panel flutter problem is implemented here.

In the remaining part we only consider moving cells with polygonal boundaries where the cell movement is prescribed by the movement of the vertices.

4.1.3 The Geometric Conservation Law (GCL)

Here we outline the meaning and implications of the GCL for 2D finite volume schemes on moving grids. For the moving subdomain $\Omega(t)$ we can formulate the (*continuous*) GCL,

$$|\Omega(t^{n+1})| \;-\; |\Omega(t^n)| \quad = \quad \int_{t^n}^{t^{n+1}} \int_{\partial\Omega(t)} \dot{\boldsymbol{x}}^T\, \boldsymbol{n}\;\, ds\, dt\;. \tag{4.5}$$

It states that the change in volume is due to the area swept over by the moving boundary. Of course, this equality is also present in the Euler equations. It may be refound by noting that $U \equiv \overline{U} = const.$ is a solution of the Euler equations and thus also has to satisfy the Euler equations when expressed for a moving domain. I.e. plugging $U \equiv \overline{U}$ into (4.1), using the flux (2.2) and the fact that $\int_{\partial\Omega} c^T n\, ds = 0$ for a constant vector c, (4.5) results.

It makes sense to demand (4.5) also on the discrete level as a consistency condition, which influences the 3rd and 4th approximation step. More precisely, in the recent paper [22], assuming a CFL–condition, the satisfaction of the *discrete GCL that corresponds to a scheme* was proven to be equivalent to *nonlinear stability* for scalar hyperbolic equations. Here some explanations are needed: Propose some scheme by discretizing the integrals in (4.3); if this scheme is satisfied for $U_i^n \equiv U_i^{n+1} \equiv \overline{U} = const.$, then the scheme is said to satisfy its discrete GCL. Nonlinear stability is meant in the sense that the maxima, respectively minima, do not increase, respectively decrease, from one to the next time level, a property shared also by the exact solution of a scalar hyperbolic equation.

Let us discuss the discrete GCL for a certain class of discretizations: We assume vertex movements $\boldsymbol{x}(t)$ to be given and the edges moving as straight lines between them. We employ a standard quadrature rule for the integrals in (4.3) and in case that intermediate values for U are needed let them be defined through linear interpolation from U^n and U^{n+1}. Plugging $U_i^n \equiv U_i^{n+1} \equiv \overline{U} = const.$ into this scheme, using the fact that a reconstruction-limitation and numerical flux have to satisfy the compatibility condition $U_{ij} \equiv \overline{U} \;\; \forall ij$ and $F(\overline{U}, \overline{U}, \dot{\boldsymbol{x}}, \boldsymbol{n}) \equiv f(\overline{U}, \dot{\boldsymbol{x}})\, \boldsymbol{n}$, we obtain that (4.5) has to be satisfied exactly, when replacing all expressions by the corresponding ones on the discrete level.

Since the cell areas $|\Omega_i^{n+1}|$, $|\Omega_i^n|$ are evaluated exactly for cells with polygonal boundaries, their difference has to be equal to the discrete evaluation of the r.h.s. in (4.5), which depends only on the choices made in the third and fourth approximation steps. Thus we obtain the requirement, that the discrete evaluation of the r.h.s. in (4.5) has to give the exact value of the integral. Below, we will express the integrand in (4.5) as a polynomial, which means that the discrete scheme has to be *exact* for the degree of the polynomial! Otherwise the discrete equations are not satisfied when plugging in $U_i^n \equiv \overline{U}$.

Now, let us express the r.h.s. of (4.5) for one edge of a moving cell with polygonal boundary. The movement of this straight edge is entirely defined by the movement of the edge endpoints (the vertices). Assuming the movement of the two vertices to be given by $\boldsymbol{x}_l(t)$ and $\boldsymbol{x}_r(t)$, a parametrization of the moving edge is given by

$$\alpha\, \boldsymbol{x}_l(t) \;+\; (1-\alpha)\, \boldsymbol{x}_r(t)\,, \quad \text{with}\, \alpha \in [0,1]\,.$$

Expressing the normal, which is constant along the straight edge, as

$$\boldsymbol{n}(t) \;=\; H \cdot \frac{\boldsymbol{x}_r(t) - \boldsymbol{x}_l(t)}{||\boldsymbol{x}_l(t) - \boldsymbol{x}_r(t)||_2}\,, \quad \text{with} \quad H \;=\; \begin{pmatrix} 0 & -1 \\ 1 & 0 \end{pmatrix}$$

and using the calculus of integrals, we obtain

$$
\begin{aligned}
\int_{t^n}^{t^{n+1}} \int_e \dot{\boldsymbol{x}}^T \boldsymbol{n} \; ds\, dt \quad &= \\
&= \int_{t^n}^{t^{n+1}} \int_0^1 ||\boldsymbol{x}_l(t) - \boldsymbol{x}_r(t)||_2 \cdot \left(\alpha\, \dot{\boldsymbol{x}}_l(t) \,+\, (1-\alpha)\, \dot{\boldsymbol{x}}_r(t)\right)^T \cdot \boldsymbol{n}(t) \; d\alpha\, dt \\
&= \int_{t^n}^{t^{n+1}} \frac{1}{2} \left(\dot{\boldsymbol{x}}_l(t) \,+\, \dot{\boldsymbol{x}}_r(t)\right)^T H \left(\boldsymbol{x}_r(t) - \boldsymbol{x}_l(t)\right) dt
\end{aligned}
$$

The integration over α is exact when using any second order quadrature rule in our third approximation step, since the integrand is linear in α. E.g. the midpoint rule (4.4) may be used. The remaining integration over t demands the consistency between the choice of vertex-movement $\boldsymbol{x}(t)$ and the time integration scheme. E.g. when it suffices to represent the vertex positions $\boldsymbol{x}(t^n)$ and $\boldsymbol{x}(t^{n+1})$ exactly, we can assume $\boldsymbol{x}(t)$ to be linear within each time step. Then $\dot{\boldsymbol{x}}$ is a constant and the integrand is linear in t, i.e. a second order time integration suffices for the exact integration. If one wants to be exact in both position and velocities at t^n and t^{n+1} one chooses $\boldsymbol{x}(t)$ as a polynomial of third degree, and then the integrand is of degree 5 and thus a sixth order time integration scheme is needed. This discussion was motivated by a similar one in [38].

4.1.4 The numerical flux

Here we discuss the implementation of the numerical fluxes. In our code, the Van-Leer Flux-Vector Splitting (FVS) [63] and the Solomon-Osher flux [49], [26] are implemented. The Van-Leer FVS is further important for our algorithm since it is used throughout as the flux discretization in the preconditioner. Thus we only give the Van-Leer FVS explicitly.

From now on we use primitive states as flux arguments and for convenience we keep the notations for the flux f of the Euler equations (2.2) and the numerical flux F, which was introduced formally in (4.3). This corresponds also to the actual implementation.

We define the numerical fluxes for the case that the edge lies on the y-axis with the cell under consideration in the halfspace $x < 0$ and the neighbour cell in the halfspace $x > 0$. Having the primitive states $\mathcal{U}$ respectively $\mathcal{V}$ in the left respectively right halfspace, a Riemann-problem in 2D is defined and we denote the value of the exact solution at $x = 0$ by $\mathcal{U}^*$. We are interested in an approximation of the flux

$$
f^x(\mathcal{U}) \quad \equiv \quad f(\mathcal{U}, \mathbf{0}) \cdot (1,0)^T
$$

at $\mathcal{U}^*$. Here f is the flux of the Euler equations (2.2). We denote the approximation given by the numerical flux by $F^x(\mathcal{U},\mathcal{V})$, thus formally we want to have

$$F^x(\mathcal{U},\mathcal{V}) \quad \approx \quad f^x(\mathcal{U}^*) \quad \equiv \quad U^*\,u^* \; + \begin{pmatrix} 0 \\ p^* \\ 0 \\ p^*\,u^* \end{pmatrix} . \tag{4.6}$$

The general case of the numerical flux $F(\mathcal{U},\mathcal{V},\dot{\boldsymbol{x}})$ on an arbitrarily oriented edge moving with velocity $\dot{\boldsymbol{x}}$ is then carried back to F^x via transformations in Sec. 4.1.5.

The Van-Leer FVS

The typical form of a FVS is $F^x(\mathcal{U},\mathcal{V}) \;=\; f^+(\mathcal{U}) \;+\; f^-(\mathcal{V})$, where f^+ and f^- are chosen such that at least

- $f^x \quad = \quad f^+ \;+\; f^-$,
- the Jacobian of f^+, respectively f^-, taken with respect to the conservative state, has only nonnegative, respectively nonpositive, eigenvalues.

Van-Leer's FVS satisfies these conditions, and has some more useful properties, see [63]. Using $M = u/c$, Van-Leer's FVS is given by

$$f^-(\mathcal{U}) \;=\; f^x(\mathcal{U}) \quad \text{and} \quad f^+(\mathcal{U}) \;=\; 0\,, \qquad \text{if} \quad M \le -1$$

$$f^{\pm}(\mathcal{U}) \quad = \quad \pm\,\frac{\rho}{4\,c}\,(u \pm c)^2 \cdot \begin{pmatrix} 1 \\[1ex] \dfrac{(\gamma-1)\,u \pm 2\,c}{\gamma} \\[2ex] v \\[1ex] \dfrac{((\gamma-1)\,u \pm 2\,c)^2}{2\,(\gamma^2-1)} \end{pmatrix} , \qquad \text{if} \quad -1 < M < 1 \tag{4.7}$$

$$f^-(\mathcal{U}) \;=\; 0 \quad \text{and} \quad f^+(\mathcal{U}) \;=\; f^x(\mathcal{U})\,, \qquad \text{if} \quad M \ge 1$$

4.1.5 General representation of numerical fluxes over moving edges

Here we use the rotational and the Galilean invariance of the Euler equations and carry them over to the numerical fluxes. For proofs of these invariances, see [26]. We obtain an expression for the evaluation of the numerical flux at an arbitrarily oriented moving edge via transformations of F^x. Actually, one can also set up various numerical fluxes for arbitrary edges and prove their invariances; the rotational invariance of the Solomon-Osher flux and some others is proven in [26].

4.1.5.1 Rotational invariance

We introduce the rotation matrix Q corresponding to an edge with normal vector $\boldsymbol{n} = (cos, sin)^T$, such that the velocity components in $\mathcal{U}$ are transformed to their normal and tangential part by Q^{-1}. We have

$$v_n = \boldsymbol{v}^T \boldsymbol{n} = u\, cos + v\, sin\,, \quad v_t = -u\, sin + v\, cos\,,$$

so that

$$Q^{-1} = \begin{pmatrix} 1 & & & \\ & cos & sin & \\ & -sin & cos & \\ & & & 1 \end{pmatrix}, \quad Q = \begin{pmatrix} 1 & & & \\ & cos & -sin & \\ & sin & cos & \\ & & & 1 \end{pmatrix}.$$

Then it is easily shown that the flux (2.2) of the Euler equations satisfies

$$f(\mathcal{U},0)\,\boldsymbol{n} \quad = \quad Q\, f^x(Q^{-1}\mathcal{U})\ . \tag{4.8}$$

Comparing with (4.6), we obtain the numerical flux $F(\mathcal{U},\mathcal{V},\mathbf{0})$ over a generally oriented non-moving edge,

$$F(\mathcal{U},\mathcal{V},\mathbf{0}) \quad = \quad Q\, F^x(Q^{-1}\mathcal{U}, Q^{-1}\mathcal{V})\ . \tag{4.9}$$

4.1.5.2 Galilean invariance

We look again at a Riemann-Problem. Initially, we have constant states on the two sides of an arbitrarily oriented interface, $\mathcal{U}$ in the $-\boldsymbol{n}$-halfspace and $\mathcal{V}$ in the $\boldsymbol{n}$-halfspace. We let the interface move with the constant velocity $\dot{\boldsymbol{x}}$ and pick the value $\overline{\mathcal{U}}^*$ of the solution on the moving interface. We look for a formula for $f(\overline{U}^*, \dot{\boldsymbol{x}})\,\boldsymbol{n}$ in terms of the flux at a non–moving interface:

Given the solution of the Riemann-problem $\overline{\mathcal{U}}(t,\boldsymbol{x}) \equiv (\rho(t,\boldsymbol{x}), \boldsymbol{v}(t,\boldsymbol{x}), p(t,\boldsymbol{x})\,)$, from the Galilean invariance of the Euler equations we get that

$$\mathcal{U}(t,\boldsymbol{x}_G) \quad \equiv \quad (\,\rho(t,\boldsymbol{x}_G + \dot{\boldsymbol{x}}\,t),\ \boldsymbol{v}(t,\boldsymbol{x}_G + \dot{\boldsymbol{x}}\,t) - \dot{\boldsymbol{x}},\ p(t,\boldsymbol{x}_G + \dot{\boldsymbol{x}}\,t)\,)$$

is the solution corresponding to the Riemann-data $\mathcal{U} - \dot{X}$, $\mathcal{V} - \dot{X}$, where we have set $\dot{X} \equiv (0,\dot{x},\dot{y},0)^T$ with a constant velocity vector $\dot{\boldsymbol{x}} \equiv (\dot{x},\dot{y})^T$. Galilei moves with the velocity $\dot{\boldsymbol{x}}$ and the coordinates in the system moving with him are denoted by $\boldsymbol{x}_G$. So when Galilei keeps looking at the same point $\boldsymbol{x}_G$ he observes the fluid state $\mathcal{U}$. Thus the value $\mathcal{U}(t,\boldsymbol{x})$ he observes on the moving interface is $\mathcal{U}^* \equiv \overline{\mathcal{U}}^* - \dot{X}$.

Inserting these relations, we have

$$f(\overline{\mathcal{U}}^*, \dot{\boldsymbol{x}})\,\boldsymbol{n} \quad = \quad \begin{pmatrix} \overline{\rho}^* \\ \overline{\rho}^*\overline{u}^* \\ \overline{\rho}^*\overline{v}^* \\ \frac{1}{2}\,\overline{\rho}^*\,|\overline{\boldsymbol{v}}^*|^2 + \overline{p}^*/(\gamma-1) \end{pmatrix} (\overline{\boldsymbol{v}}^* - \dot{\boldsymbol{x}})^T\boldsymbol{n}\ + \begin{pmatrix} 0 \\ \overline{p}^* cos \\ \overline{p}^* sin \\ \overline{p}^*\,\overline{\boldsymbol{v}}^{*T}\boldsymbol{n} \end{pmatrix}$$

$$= \begin{pmatrix} \rho^* \\ \rho^*(u^* + \dot{x}) \\ \rho^*(v^* + \dot{y}) \\ \frac{1}{2}\,\rho^*\,|\boldsymbol{v}^* + \dot{\boldsymbol{x}}|^2 + p^*/(\gamma-1) \end{pmatrix} \boldsymbol{v}^{*T}\boldsymbol{n} \;+\; \begin{pmatrix} 0 \\ p^* cos \\ p^* sin \\ p^*\,(\boldsymbol{v}^* + \dot{\boldsymbol{x}})^T \boldsymbol{n} \end{pmatrix}$$

$$= \begin{pmatrix} \rho^* \\ \rho^* u^* \\ \rho^* v^* \\ \frac{1}{2}\,\rho^*\,|\boldsymbol{v}^*|^2 + p^*/(\gamma-1) \end{pmatrix} \boldsymbol{v}^{*T}\boldsymbol{n} \;+\; \begin{pmatrix} 0 \\ p^* cos \\ p^* sin \\ p^*\,\boldsymbol{v}^{*T}\boldsymbol{n} \end{pmatrix} \;+$$

$$+ \begin{pmatrix} 0 \\ \dot{x}\,\rho^*\boldsymbol{v}^{*T}\boldsymbol{n} \\ \dot{y}\,\rho^*\boldsymbol{v}^{*T}\boldsymbol{n} \\ (\frac{1}{2}\,|\dot{\boldsymbol{x}}|^2 + \boldsymbol{v}^{*T}\dot{\boldsymbol{x}})\,\rho^*\boldsymbol{v}^{*T}\boldsymbol{n} + p^*\dot{\boldsymbol{x}}^T\boldsymbol{n} \end{pmatrix} .$$

This may also be written as

$$f(\overline{\mathcal{U}}^*, \dot{\boldsymbol{x}})\,\boldsymbol{n} \quad = \quad S \cdot f(\mathcal{U}^*, \boldsymbol{0})\,\boldsymbol{n} \quad = \quad S \cdot f(\overline{\mathcal{U}}^* - \dot{X}, \boldsymbol{0})\,\boldsymbol{n} \tag{4.10}$$

where

$$S \quad = \quad \begin{pmatrix} 1 & & & \\ \dot{x} & 1 & & \\ \dot{y} & & 1 & \\ |\dot{\boldsymbol{x}}|^2/2 & \dot{x} & \dot{y} & 1 \end{pmatrix} .$$

Carrying this identity over to the numerical flux, we have

$$F(\mathcal{U}, \mathcal{V}, \dot{\boldsymbol{x}}, \boldsymbol{n}) \quad = \quad S\,F(\mathcal{U} - \dot{X},\, \mathcal{V} - \dot{X}, \boldsymbol{0}, \boldsymbol{n})\,. \tag{4.11}$$

Note again, that (4.11) was derived by carrying over the corresponding identity (4.10) that holds for exact solutions of the Euler equations. Actually (4.11) may be used as a definition for the l.h.s. The l.h.s. may also be derived by other means, for example in [3] Van-Leer's FVS was extended to the case of moving edges by carrying over Van-Leer's derivation of the FVS for fixed edges [63]. Collecting terms, one can check that the expression found in [3] for the l.h.s of (4.11) is equal to the expression which we get when inserting Van-Leer's FVS from [63] into the r.h.s. of (4.11).

Alltogether

Applying (4.11) and (4.9) successively we get a formula for the flux $F(\mathcal{U}, \mathcal{V}, \dot{\boldsymbol{x}}, \boldsymbol{n})$ over a generally oriented moving edge in terms of F^x,

$$F(\mathcal{U}, \mathcal{V}, \dot{\boldsymbol{x}}, \boldsymbol{n}) \quad = \quad S\,Q\,F^x\big(Q^{-1}\,(\mathcal{U} - \dot{X}),\, Q^{-1}\,(\mathcal{V} - \dot{X})\big)\ . \tag{4.12}$$

4.1.6 The numerical flux at impermeable and artificial boundaries

As will be seen in the following section the boundary condition $\boldsymbol{v}^T\boldsymbol{n} = \dot{\boldsymbol{x}}^T\boldsymbol{n}$ from Sec. 2.1.1.1 which is to be imposed at moving impermeable boundaries is satisfied at the quadrature point of the edge, due to the reconstruction. The flux at such a boundary is given by (2.3) which is approximated with the pressure at the edge center and the normal velocity of the center, i.e.

$$|e_{ij}| \cdot F(U_{ij},\,\cdot\,,\dot{\boldsymbol{x}}_{ij},\boldsymbol{n}_{ij}) \quad = \quad |e_{ij}|\,p_{ij}\begin{pmatrix} 0 \\ n_{ij,1} \\ n_{ij,2} \\ \dot{\boldsymbol{x}}_{ij}^T\boldsymbol{n}_{ij} \end{pmatrix}. \tag{4.13}$$

Often this implementation of the boundary flux is *successfully* implemented in CFD–codes without taking care of the condition $\boldsymbol{v}^T\boldsymbol{n} = \dot{\boldsymbol{x}}^T\boldsymbol{n}$ imposed on the velocity.

At an artificial boundary edge (inflow or outflow) we place a ghost cell which is considered to lie on the boundary. Across the boundary edge the nonreflecting modification of the Euler equations (2.4) discussed in Sec. 2.1.1.2 is discretized in upwind manner of first order in space. The tangential contribution of (2.4) is neglected, i.e. denoting the state inside the domain by U_i and the state in the ghost cell by U_g, the discrete equations are

$$\frac{dU_g}{dt} + A_n^+(U_g)\,\frac{U_g - U_i}{\Delta\, x_n} \quad = \quad 0\,.$$

4.1.7 Linear reconstruction and limiter

The issues of reconstruction and limiting are both implemented in an unstructured grid manner. The reconstruction is obtained from a least-squares-problem for each cell and the switch towards a first order discretization near discontinuities is realized with Venkatakrishnan's limiter [64]. According to [1] this strategy is superior in solution quality and convergence properties compared to other combinations of reconstruction and limiting on unstructured grids. The implementations presented below were tested with the steady problems considered in [1], yielding similar solution qualities and convergence properties.

To obtain the reconstruction from a least-squares-problem is a common strategy [26]. Here we propose a least-squares-functional that should suit unstructured grids very well.

We assume each primitive variable q to have in each cell a linear distribution of the form

$$q(x,y) \;=\; q_i + q_x(x-x_i) + q_y(y-y_i)\,,$$

where (x_i, y_i) is the cell barycenter and thus q_i its mean value. The distribution of the mean values over all cells are assumed as known and the slopes q_x, q_y are selected such that they minimize

$$F(q_x,q_y) \;=\; \int_{\mathcal{C}} (q(x,y) - q_{\mathcal{C}}(x,y))^2 ds\,.$$

Here the curve $\mathcal{C}$ is the closed polygonal curve connecting the barycenters of adjacent neighbour cells, as shown in the Fig. 4.2. $q_{\mathcal{C}}$ is the continuous, piecewise linear function defined on that curve by setting

$$q_{\mathcal{C}}(x_j, y_j) = q_j \quad \text{for all barycenters of the neighbour cells } (x_j, y_j)\,.$$

Since $q - q_{\mathcal{C}}$ is linear on each section of the curve that connects two barycenters, F can be calculated exactly by simple quadrature formulas and F is a quadratic functional in (q_x, q_y). The problem

$$\text{find} \quad q_x, q_y \quad \text{such that} \quad F(q_x, q_y) \;=\; \min_{(s_1,s_2)\in \mathbb{R}^2} F(s_1, s_2)$$

is easily solved via a system of two linear equations. Finally we steer the space discretization order by modifying the slopes with a factor ϕ,

$$q_x \;:=\; \phi \cdot q_x \;, \qquad q_y \;:=\; \phi \cdot q_y.$$

For a given cell Ω_i Venkatakrishnan's slope limiter ϕ is given as a minimum over all its edges:

$$\begin{aligned}
\text{Defining} \quad \epsilon \;&=\; \left(\frac{k \cdot |\,\mathcal{C}_i\,|}{\pi}\right)^3 \quad \text{with} \quad k = 2 \quad \text{and the "cell diameter"} \quad |\,\mathcal{C}_i\,|/\pi \;, \\
\Delta_{ij} \;&=\; q_j - q_i \;, \\
\overline{\Delta}_{ij} \;&=\; q_x\,(x_{ij} - x_i) \;-\; q_y\,(y_{ij} - y_i) \;, \\
&\;\; \text{with the coordinates of the edge center} \quad (x_{ij}, y_{ij}) \\
&\;\; \text{and if} \quad \overline{\Delta}_{ij} \cdot \Delta_{ij} \;<\; 0 \qquad \text{then set} \qquad \Delta_{ij} \;=\; 0 \;, \\
\text{the limiter is} \quad \phi \;&=\; \min\nolimits_{e_{ij}\subset\partial\Omega_i} \; \frac{(\Delta_{ij}^2 + \epsilon) + 2\,\Delta_{ij}\,\overline{\Delta}_{ij}}{\Delta_{ij}^2 + 2\,\overline{\Delta}_{ij}^2 + \Delta_{ij}\,\overline{\Delta}_{ij} + \epsilon} \;.
\end{aligned}$$

4.1.7.1 Modification at impermeable boundaries

At a flux evaluation point on a (moving) wall we want the normal fluid velocity to equal the normal wall velocity, $\dot{\boldsymbol{x}}^T\boldsymbol{n} = \boldsymbol{v}^T\boldsymbol{n}$. We achieve this by modifying the velocity-slopes obtained from the above reconstruction and limiting process. Let u_x, u_y, v_x, v_y be the obtained slopes of the velocity vector $\boldsymbol{v} \equiv (u, v)^T$. We define the normalized vector $\boldsymbol{\eta}$ to point from the cell barycenter to the evaluation point on the edge and the normalized vector $\boldsymbol{\vartheta}$ to be perpendicular to $\boldsymbol{\eta}$. Then we consider the possible set of modified slopes $\overline{u}_x, \overline{u}_y, \overline{v}_x, \overline{v}_y$ to be those obtained by keeping the $\boldsymbol{\vartheta}$-derivatives u_ϑ and v_ϑ fixed and changing the $\boldsymbol{\eta}$-derivatives u_η and v_η such that we have $\dot{\boldsymbol{x}}^T\boldsymbol{n} = \overline{\boldsymbol{v}}^T\boldsymbol{n}$, where $\overline{\boldsymbol{v}}$ is the velocity at the evaluation point due to the modified slopes. Amongst the possible

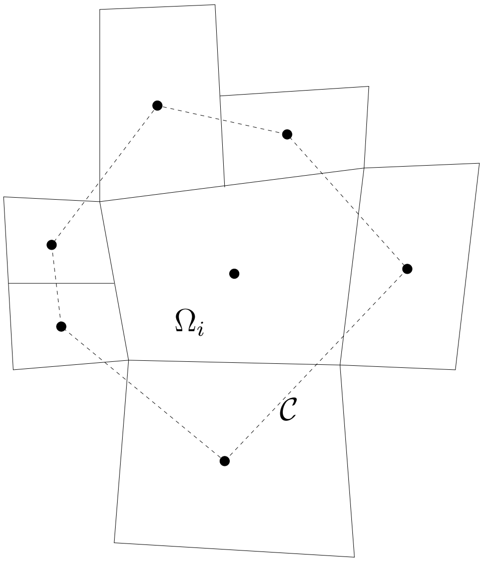

Figure 4.2: The cell Ω_i, its neighbour cells and the curve $\mathcal{C}$ are shown. $\mathcal{C}$ is a polygonal curve connecting the barycenters of Ω_i's neighbour cells.

modified slopes we choose the one deviating the least from the original slopes, i.e. we solve the least-squares-problem

$$\min\{(u_x-\overline{u}_x)^2+(u_y-\overline{u}_y)^2+(v_x-\overline{v}_x)^2+(v_y-\overline{v}_y)^2 \ : \ \text{all} \quad \overline{u}_x, \overline{u}_y, \overline{v}_x, \overline{v}_y \quad \text{with} \quad \dot{\boldsymbol{x}}^T\boldsymbol{n} = \overline{\boldsymbol{v}}^T\boldsymbol{n}\} \ .$$

The construction makes the least-squares-problem particularly simple:

$$\overline{\boldsymbol{v}} \ = \ \boldsymbol{v}_i + \Delta \cdot (\overline{u}_\eta, \overline{v}_\eta)^T \ ,$$

where Δ is the distance from the center to the evaluation point and $\boldsymbol{v}_i$ is the mean velocity vector of the cell. Thus the condition $\dot{\boldsymbol{x}}^T\boldsymbol{n} = \overline{\boldsymbol{v}}^T\boldsymbol{n}$ characterizes the set of possible modified slopes as

$$\{\overline{u}_x, \overline{u}_y, \overline{v}_x, \overline{v}_y \quad \text{with} \quad \overline{u}_\eta n_1 + \overline{v}_\eta n_2 \ = \ (\dot{\boldsymbol{x}} - \boldsymbol{v}_i)^T\boldsymbol{n}/\Delta\} \ . \tag{4.14}$$

Since we have fixed the $\boldsymbol{\vartheta}$-derivatives, we have

$$\begin{pmatrix} \overline{u}_x \\ \overline{u}_y \end{pmatrix} = \begin{pmatrix} \eta_1 & -\eta_2 \\ \eta_2 & \eta_1 \end{pmatrix} \begin{pmatrix} \overline{u}_\eta \\ u_\vartheta \end{pmatrix}, \quad \begin{pmatrix} \overline{v}_x \\ \overline{v}_y \end{pmatrix} = \begin{pmatrix} \eta_1 & -\eta_2 \\ \eta_2 & \eta_1 \end{pmatrix} \begin{pmatrix} \overline{v}_\eta \\ v_\vartheta \end{pmatrix},$$

and plugging into the least-squares-functional together with the condition in (4.14), we have a quadratic functional in, say, $\overline{u}_\eta$. We find the minimum at some $\overline{u}_\eta^*$ and define the modified slopes for the boundary cell to be

$$\begin{pmatrix} \overline{u}_x \\ \overline{u}_y \end{pmatrix} = \begin{pmatrix} \eta_1 & -\eta_2 \\ \eta_2 & \eta_1 \end{pmatrix} \begin{pmatrix} \overline{u}_\eta^* \\ u_\vartheta \end{pmatrix}, \quad \begin{pmatrix} \overline{v}_x \\ \overline{v}_y \end{pmatrix} = \begin{pmatrix} \eta_1 & -\eta_2 \\ \eta_2 & \eta_1 \end{pmatrix} \begin{pmatrix} \overline{v}_\eta^* \\ v_\vartheta \end{pmatrix}.$$

4.2 Finite element discretization for the von-Kármán panel

The standard discretization of elliptic operators is the Finite Element Method, used almost exclusively in current applications for the spacial discretization of structural equations. Conformal elements in one dimension for fourth order operators are constructed from the Hermite shape functions on the unit interval, $\xi \in [0,1]$,

$$\begin{aligned} s_{0,l}(\xi) &= (1+2\xi)\,(1-\xi)^2\,, \\ s_{0,r}(\xi) &= (3-2\xi)\,\xi^2\,, \\ s_{1,l}(\xi) &= \xi\,(1-\xi)^2\,, \\ s_{1,r}(\xi) &= -(1-\xi)\,\xi^2\,. \end{aligned}$$

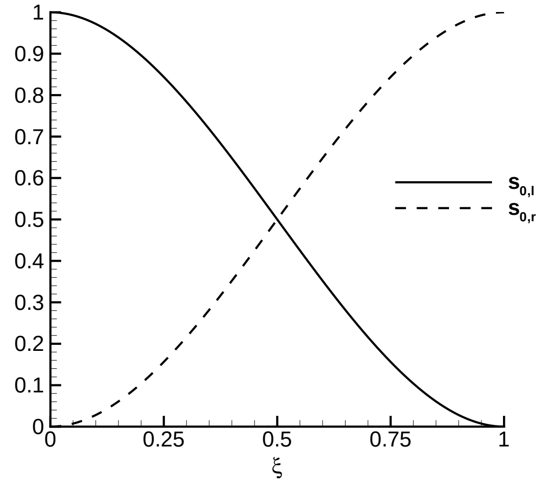

These shapes are seen in the figures on the right. They satisfy the interpolation conditions

$$\begin{aligned} s_{0,l}(0) &= 1, \quad s_{0,l}(1) = s'_{0,l}(0) = s'_{0,l}(1) = 0\,, \\ s_{0,r}(1) &= 1, \quad s_{0,r}(0) = s'_{0,r}(0) = s'_{0,r}(1) = 0\,, \\ s'_{1,l}(0) &= 1, \quad s_{1,l}(0) = s_{1,l}(1) = s'_{1,l}(1) = 0\,, \\ s'_{1,r}(1) &= 1, \quad s_{1,r}(0) = s_{1,r}(1) = s'_{1,r}(0) = 0\,. \end{aligned}$$

From the shapes we construct the basis functions. We have a domain $(a,b) \subset \mathbb{R}$ and $n+1$ equidistant nodes $x_i = a + i\,h\,,\ i = 0,1,...,n\,,$ with $h = (b-a)/n$. We only consider the boundary condition that models a beam that is *simply supported* at its ends. Thus we have a basis function at the left boundary node,

$$\phi_0^1(x) = \begin{cases} s_{1,l}((x-x_0)/h) & x \in [x_0, x_1] \\ 0 & \text{otherwise} \end{cases}\,,$$

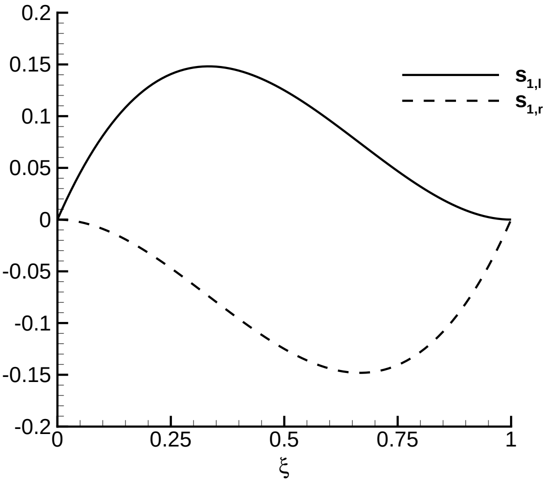

two basis functions centered at each inner node,

$$\phi_i^0(x) = \begin{cases} s_{0,r}((x-x_{i-1})/h) & x \in [x_{i-1}, x_i] \\ s_{0,l}((x-x_i)/h) & x \in [x_i, x_{i+1}] \\ 0 & \text{otherwise} \end{cases}$$

$$\phi_i^1(x) = \begin{cases} s_{1,r}((x-x_{i-1})/h) & x \in [x_{i-1}, x_i] \\ s_{1,l}((x-x_i)/h) & x \in [x_i, x_{i+1}] \\ 0 & \text{otherwise} \end{cases}$$

for $i = 1, 2, ..., n-1$, and a basis function at the right boundary,

$$\phi_n^1(x) = \begin{cases} s_{1,r}((x-x_{n-1})/h) & x \in [x_{n-1}, x_n] \\ 0 & \text{otherwise .} \end{cases}$$

For all basis functions we have

$$\begin{aligned} \phi_i^k &\in H^2(a,b) \cap H_0^1(a,b) \\ &\subset \{f \in C^1[a,b] \,:\, f(a) = f(b) = 0\} \,. \end{aligned}$$

Now the spacial discretization of the von-Kármán equations is achieved by posing the problem (2.5) only on a subspace of $H^2(0,l) \cap H_0^1(0,l)$, namely on the linear hull of the basis functions defined above. Thus we plug

$$w(t,x) \;=\; \sum_{i,k} \alpha_i^k(t)\, \phi_i^k(x)$$

into (2.5) and test with only the basis functions; further we introduce $\beta_i^k \equiv (\alpha_i^k)_t$ and obtain a first order system of ODEs:

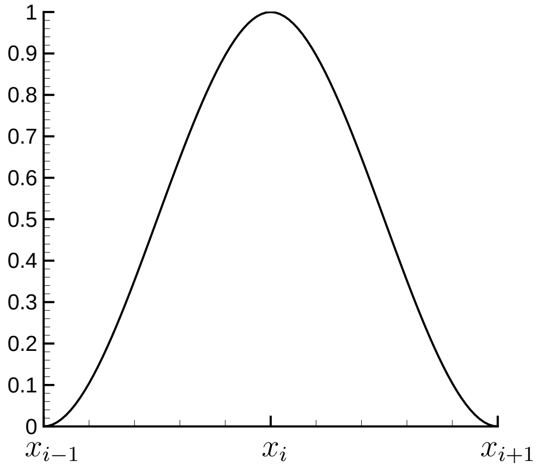

ϕ_i^0 for $i = 1, ..., n-1$

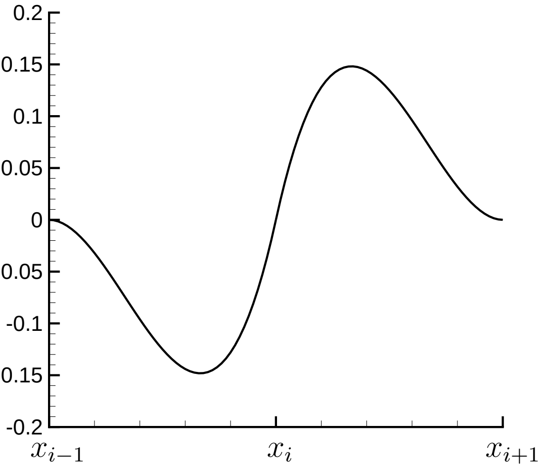

ϕ_i^1 for $i = 1, ..., n-1$

$$\sum_{i,k} D\,\alpha_i^k\,(\phi_i^k, \phi_j^l)_2 \;+\; \alpha_i^k\, N(w_x)\,(\phi_i^k, \phi_j^l)_1 \;+\; m\,(\beta_i^k)_t\,(\phi_i^k, \phi_j^l)_0 \;=\; -\,(p_1 - p_2, \phi_j^l)_0 \quad \forall\, j, l\,,$$

$$(\alpha_j^l)_t \;=\; \beta_j^l \qquad \forall\, j, l\,.$$

Above we let the indices of the basis functions ϕ_i^k, ϕ_j^l run without any further specification, but they are meant to run over all index pairs, for which a basis function was defined. Further, we have introduced abbreviations for the inner products,

$$\begin{aligned} (\phi, \psi)_0 &\equiv (\phi, \psi), \\ (\phi, \psi)_1 &\equiv (\phi_x, \psi_x), \\ (\phi, \psi)_2 &\equiv (\phi_{xx}, \psi_{xx}). \end{aligned}$$

The set of $4(n-1)+4$ ODEs may now be integrated in time with any kind of Runge-Kutta-scheme to approximately solve for discrete values of the coefficients $\alpha_i^k(t)$, $\beta_i^k(t)$. The following implicit mid-point rule will be used below in the construction of an aeroelastic scheme with correct energy transfer:

$$\sum_{i,k} D\,(\alpha_i^k)^{n+1/2}\,(\phi_i^k,\phi_j^l)_2 + (\alpha_i^k)^{n+1/2}\,N^{n+1/2}\,(\phi_i^k,\phi_j^l)_1 + m\,\frac{(\beta_i^k)^{n+1}-(\beta_i^k)^n}{\Delta t}\,(\phi_i^k,\phi_j^l)_0 \quad =$$

$$= \quad -\,((p_1-p_2)^{n+1/2},\phi_j^l)_0 \quad \forall\, j,l\,,$$

$$\frac{(\alpha_j^l)^{n+1}-(\alpha_j^l)^n}{\Delta t} \quad = \quad (\beta_j^l)^{n+1/2} \qquad \forall\, j,l\,,$$

where we have set $(...)^{n+1/2} \equiv ((...)^{n+1} + (...)^n)/2$. Defining $w^n(x) \equiv \sum_{i,k}(\alpha_i^k)^n\,\phi_i^k(x)$ and introducing the velocity $v^n(x) \equiv \sum_{i,k}(\beta_i^k)^n\,\phi_i^k(x)$, this system reads

$$\left.\begin{array}{rcl}
N^{n+1/2} & = & (N(w^{n+1}) + N(w^n))/2 \\
D\,(w^{n+1/2},\phi_j^l)_2 \;+\; N^{n+1/2}\,(w^{n+1/2},\phi_j^l)_1 \;+ & & \\
+\; m\,(v^{n+1}-v^n,\phi_j^l)_0 & = & -\,\Delta t\,((p_1-p_2)^{n+1/2},\phi_j^l)_0 \\
(\alpha_j^l)^{n+1}-(\alpha_j^l)^n & = & \Delta t\,(\beta_j^l)^{n+1/2} \\
 & & \text{for all } j,l
\end{array}\right\} \tag{4.15}$$

4.3 Coupling schemes

So far the spacial and temporal discretizations of fluid and structure are given for the separate fluid and structural code. In order to simulate a time dependent aeroelastic process, we can call the routines that advance the fluid or the structure by a single time step from a master program, providing each medium with available data from the other medium. This kind of *partitioned* coupling can be performed in various ways, leading to the classes of coupling schemes A, B, C as discussed in the introductory chapter. Those partitioned schemes implemented here for the purpose of comparisons are discussed in more detail below. The newly developed Newton–GMRes algorithm to achieve a tight coupling (class C) is not a partitioned scheme, but uses independent modules from the fluid and the structure code. The Newton–GMRes coupling is described in more detail in Sec. 5.3.

The most simple coupling scheme, the *loose* coupling, is depicted in Fig. 4.3. We can see that with fluid state U^0 and structure deflection w^0 given at the same time level, first the structure is advanced, taking as the load the pressure from U^0. The time and space discretization of the structure may be of arbitrary order. Next the new position x^1 of the fluid grid is determined from the calculated deflection w^1. We assume to use a standard high-resolution FVM in the fluid as described in Sec. 4.1. The GCL is satisfied by employing the mid-point rule in the time integration, assuming the vertex movements as linear with a constant velocity within each time step. The flux evaluation is performed at the half time grid position and averaged fluid state $U^{1/2}$ and the grid velocities as given in the figure. Of course, due to the lagged action of the aerodynamic load, this scheme does not have a conservative load transfer at the fluid-structure-interface and the high orders present in the separate fluid and structure codes are reduced in the coupled version, compare Chapter 6 or [38]. Nevertheless, this scheme may suffice in many cases [23] and is the easiest to implement.

Apart from the flow solver and the structural solver the loose coupling is finally defined when the discrete load transfer from the representation of the fluid pressure to the representation of the structural load is specified and the boundary positions of the fluid grid are given through the discrete panel deflections. These points are discussed in Sec. 4.4, and are also subject to verification for the following coupling schemes.

An improved partitioned scheme is the *staggered* scheme from [38], shown in Fig. 4.4.

A time stepping scheme that is *formally* of second order in each discretization step, with no time shift in the load transfer, is given in Fig. 4.5, the *tight* coupling. It integrates the coupled discrete fluid-structure system implicitly in time. For this coupling scheme the discretization at the interface can further be specified to result in a *correct energy transfer* between fluid and structure as shown in the next section. Due to the implicit nature of this scheme a sufficiently convergent iteration process is needed to reduce the residual.

One possible way to achieve a tight coupling, is to apply a *fixed–point–iteration* (FPI), where a fixed–point–step is done in the manner of a loose coupling. We do this by taking U^0 as an initial guess for U^1 and then satisfy alternatingly the equations of the tight coupling in the sequence 1,2,3 defined in the loose coupling. In the third step U^1 is renewed and is then used to repeat the iteration until a convergence criterion is met. A similar strategy to obtain a tight coupling can be found in [46] or [33].

The particular iteration proposed here to achieve a tight coupling is to use a *matrix–free Newton–GMRes* iteration that is applied to the coupled system of fluid–structure equations of Fig. 4.5. This algorithm is further discussed in Sec. 5.3.

Other coupling procedures

Various other coupling procedures can be found in the literature. We mention two classes not implemented here: Often the structural codes allow larger time steps than the fluid codes, so that the loose or the staggered coupling is further refined by doing several fluid time steps during one structural time step, which is a coupling procedure known as *subcycling* [23]. A *predictor* scheme is present, when either the fluid data [33] or the structural data [52] is interpolated from previous time steps to obtain an estimate of the fluid or the structural state at the end of the current time step.

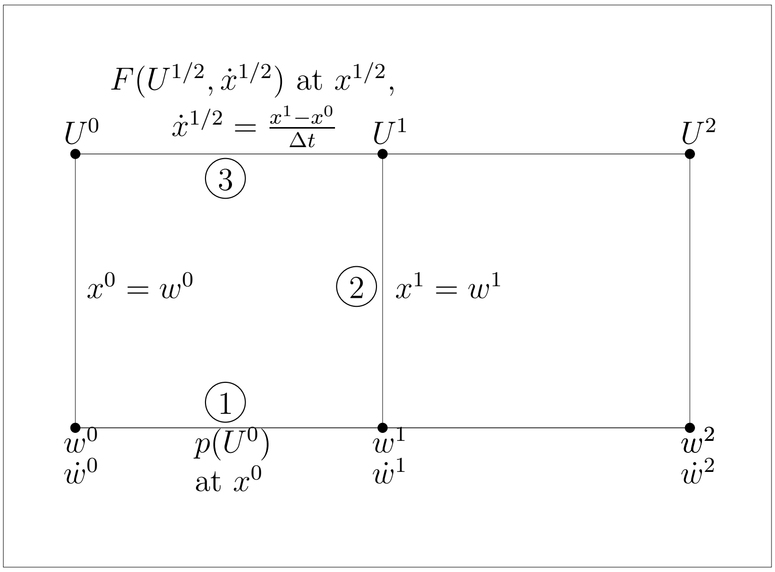
$F(U^{1/2}, \dot{x}^{1/2})$ at $x^{1/2}$,
$\dot{x}^{1/2} = \frac{x^1 - x^0}{\Delta t}$
U^0
U^1
U^2
③
$x^0 = w^0$
②
$x^1 = w^1$
①
w^0
$\dot{w}^0$
$p(U^0)$
at x^0
w^1
$\dot{w}^1$
w^2
$\dot{w}^2$

Figure 4.3: Loose Coupling

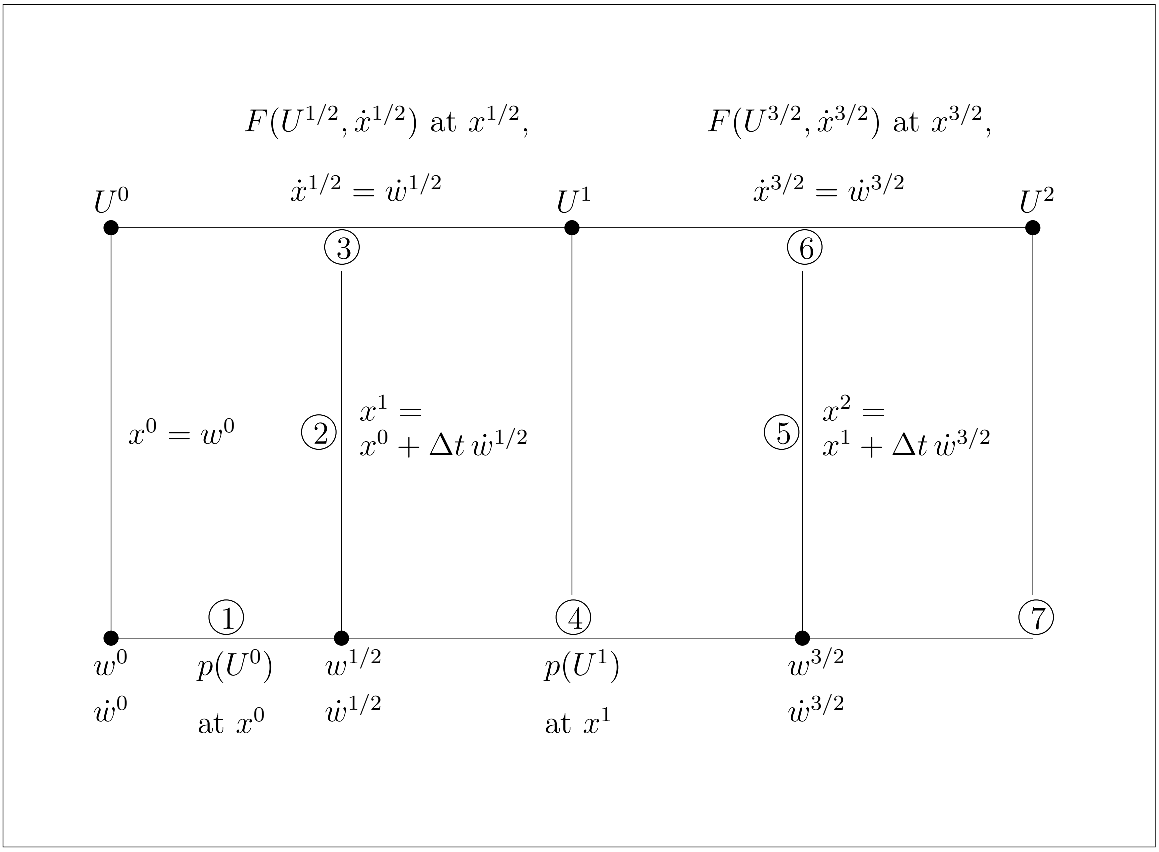
$F(U^{1/2}, \dot{x}^{1/2})$ at $x^{1/2}$,
$\dot{x}^{1/2} = \dot{w}^{1/2}$
$F(U^{3/2}, \dot{x}^{3/2})$ at $x^{3/2}$,
$\dot{x}^{3/2} = \dot{w}^{3/2}$
U^0
U^1
U^2
③
⑥
$x^0 = w^0$
②
$x^1 =$
$x^0 + \Delta t\, \dot{w}^{1/2}$
⑤
$x^2 =$
$x^1 + \Delta t\, \dot{w}^{3/2}$
①
④
⑦
w^0
$\dot{w}^0$
$p(U^0)$
at x^0
$w^{1/2}$
$\dot{w}^{1/2}$
$p(U^1)$
at x^1
$w^{3/2}$
$\dot{w}^{3/2}$

Figure 4.4: Staggered Coupling

4.4 Energy transfer on the discrete level

On the continuous level, continuity in the forces and the connectivity of the two media also imply a correct energy transfer between fluid and structure. This was used in Sec. 2.3 to reconfirm the coupling conditions on the continuous level and it was connected to the question of uniqueness via an energy-estimate in Sec. 3.2.

The description of the coupling schemes in Fig. 4.3, Fig. 4.4, Fig. 4.5 only inform us about the time levels from which fluid and structure data are taken to transfer them to the other medium. These transfers concern the connectivity of the media and the load transfer. Details, like the quadrature rules defining the load transfer, still have to be specified.

4.4.1 Connectivity

In all coupling schemes, the transfer imposing the connectivity is directed from the structure to the fluid. It is implemented by placing fluid vertices on the panel initially and thus identifying each of these vertices with a material point of the panel. At a discrete time level the position of each of these vertices is defined by the position of the corresponding material point on the deflected panel.

4.4.2 Load transfer

Given a discrete pressure distribution in the fluid on the interface, a *conservative load projection* to the structure can be implemented as follows. For each fluid edge it has to be checked, which panel element it intersects, and then a sufficiently accurate quadrature rule on the intersection interval has to be employed to evaluate the load integral in (4.15). This kind of load projection is an option in our code. Various other possibilities to handle this point are discussed in [11]. But note that, as for example in the loose coupling, Fig. 4.3, even if the pressure distribution from U^0 is projected conservatively to a structural load distribution, we do not have a *conservative load transfer*, since the pressure distribution from $U^{1/2}$ enters the flux evaluation in the fluid! Note the subtle differences in our usage of the terms *conservative projection* and *conservative transfer*, that was already discussed in the introductory chapter with the aid of the formulas (1.4) and (1.3). We can only speak of a conservative load transfer, if we take the pressure distribution of the fluid that enters the flux evaluation, and project this pressure distribution conservatively to obtain the load that enters the structural equation.

In any case, as pointed out in [11], a conservative load projection can be very advantageous. In the presence of pressure distributions with sharp peaks it is superior in comparison to projections that rely on traditional interpolation strategies.

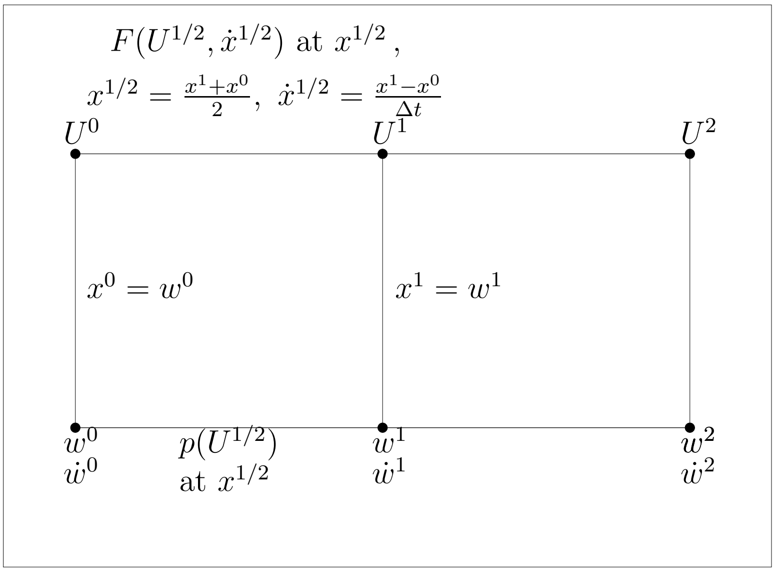
$F(U^{1/2}, \dot{x}^{1/2})$ at $x^{1/2}$,
$x^{1/2} = \frac{x^1+x^0}{2}$, $\dot{x}^{1/2} = \frac{x^1-x^0}{\Delta t}$
U^0
U^1
U^2
$x^0 = w^0$
$x^1 = w^1$
w^0
$\dot{w}^0$
$p(U^{1/2})$
at $x^{1/2}$
w^1
$\dot{w}^1$
w^2
$\dot{w}^2$

Figure 4.5: Tight Coupling

4.4.3 Construction of a scheme with correct energy transfer

Even with a conservative load transfer as described in Sec. 4.4.2 a *correct* or *conservative energy transfer* on the discrete level will only be realized approximately. To implement a correct energy transfer, the fluid grid movement and the evaluation of the load integrals have to be adapted to each other. Below we construct such a scheme with a rather simple load transfer quadrature rule. In this construction, different, so–called *non − matching*, representations of the fluid boundary and the deflected panel are present. Here, as described in earlier sections, the fluid boundary is piecewise linear, while the deflected panel is a piecewise polynomial of third order, compare Fig. 4.6. Such non-matching representations are commonly used in fluid-structure discretizations.

Employing the mid-point rule for the time integration of the spacially discretized flow equations (4.3), the energy component for a cell can be written as

$$E_{F,i}^{n+1} - E_{F,i}^{n} \quad = \quad -\Delta t \cdot \sum_{e_{ij} \subset \partial\Omega_i} |e_{ij}^{n+1/2}| \cdot F_4(\mathcal{U}_{ij}^{n+1/2}, \mathcal{U}_{ji}^{n+1/2}, \dot{\boldsymbol{x}}_{ij}^{n+1/2}, \boldsymbol{n}_{ij}^{n+1/2}) \ .$$

Here F_4 is the fourth component of the numerical flux F in (4.3) and all its arguments are taken at the edge center and the energy contained in the ith cell at time level n is $E_{F,i}^n = |\Omega_i^n| \cdot (\rho_i^n |\boldsymbol{v}_i^n|^2/2 + p_i^n/(\gamma-1))$. Similar to Sec. 2.3 we look at the energy production on the interface, which we want to vanish. The discrete fluid energy is $E_F^n \equiv \sum_{\Omega_i \subset \Omega_F^C} E_{F,i}^n$. We can divide the energy production into the contribution $\partial E_{FS}^{n+1/2}$ coming from the interface and the contribution $\partial E_F^{n+1/2}$ from the remaining boundary. Thus we have

$$E_F^{n+1} - E_F^n \quad = \quad \partial E_{FS}^{n+1/2} + \partial E_F^{n+1/2} \ . \tag{4.16}$$

The numerical flux at an interface edge is given by

$$F_4(\mathcal{U}_{ij}^{n+1/2},\ \cdot\ , \dot{\boldsymbol{x}}_{ij}^{n+1/2}, \boldsymbol{n}_{ij}^{n+1/2}) \quad \equiv \quad p_{ij}^{n+1/2}\,(\dot{\boldsymbol{x}}_{ij}^{n+1/2})^T \boldsymbol{n}_{ij}^{n+1/2} \ ,$$

and summing over all edges on the interface, we obtain

$$\partial E_{FS}^{n+1/2} \quad \equiv \quad -\Delta t \sum_{e_{ij}\subset\Gamma_{FS}} |e_{ij}^{n+1/2}| \cdot p_{ij}^{n+1/2}\,(\dot{\boldsymbol{x}}_{ij}^{n+1/2})^T \boldsymbol{n}_{ij}^{n+1/2} \ .$$

Let us look at a single edge $e \equiv \overline{\boldsymbol{x}_l\,\boldsymbol{x}_r} \subset \Gamma_{FS}$ with end vertices $\boldsymbol{x}_l, \boldsymbol{x}_r$, omitting the ij-indices for the moment. Then $\dot{\boldsymbol{x}}^{n+1/2}$ is given by

$$\dot{\boldsymbol{x}}^{n+1/2} \quad \equiv \quad \frac{1}{2}\left\{\frac{\boldsymbol{x}_l^{n+1}-\boldsymbol{x}_l^n}{\Delta t} + \frac{\boldsymbol{x}_r^{n+1}-\boldsymbol{x}_r^n}{\Delta t}\right\} \ .$$

Further from $\boldsymbol{x}_l^n = (\xi_l, w_l^n)^T$, $w_l^n \equiv w(t^n, \xi_l)$ for some $\xi_l \in [0, l]$, and correspondingly for the right point $\boldsymbol{x}_r^n$, we get

$$(\dot{\boldsymbol{x}}^{n+1/2})^T \boldsymbol{n}^{n+1/2} \quad = \quad \frac{1}{2}\left\{\frac{w_l^{n+1}-w_l^n}{\Delta t} + \frac{w_r^{n+1}-w_r^n}{\Delta t}\right\} n_2^{n+1/2} \ .$$

Looking again at specific edges, adding the indices ij, using $|e_{ij}^{n+1/2}| = -(\xi_{r,ij} - \xi_{l,ij})/n_{2,ij}^{n+1/2}$ and denoting $\Delta\xi_{ij} \equiv \xi_{r,ij} - \xi_{l,ij}$, we obtain

$$\begin{aligned} \partial E_{FS}^{n+1/2} \quad &= \\ = \quad \Delta t \textstyle\sum_{e_{ij}\subset\Gamma_{FS}} \Delta\xi_{ij}\, p_{ij}^{n+1/2} & \frac{1}{2}\left\{\frac{w^{n+1}(\xi_{l,ij}) - w^n(\xi_{l,ij})}{\Delta t} + \frac{w^{n+1}(\xi_{r,ij}) - w^n(\xi_{r,ij})}{\Delta t}\right\} . \end{aligned} \tag{4.17}$$

We turn to the discrete panel equations (4.15) and have to specify the load term due to the coupling conditions and its evaluation through a quadrature rule,

$$\begin{aligned} -\Delta t\ \left((p_1 - p_2)^{n+1/2}\,,\, \phi_k^h\right)_0 \quad &= \quad -\Delta t\ \left(p(\xi, w^{n+1/2}(\xi)) - p_\infty\,,\, \phi_k^h(\xi)\right)_0 \quad \approx \\ \approx \quad -\Delta t\ \textstyle\sum_{e_{ij}\subset\Gamma_{FS}} \Delta\xi_{ij}\,(p_{ij}^{n+1/2} - p_\infty)\ & \left\{\phi_k^h(\xi_{l,ij}) + \phi_k^h(\xi_{r,ij})\right\}/2 \ . \end{aligned} \tag{4.18}$$

Note that most summands do not contribute anything since $\xi_{l,ij}, \xi_{r,ij} \notin \operatorname{supp}(\phi_k^h)$ in most cases. For the inner products on the l.h.s. of (4.15) we may use a different quadrature rule, let us assume that this rule is exact (the inner products of the shapes can be calculated and stored at the beginnning of the computation !!). Using the quadrature formula (4.18) in (4.15) and multiplying with $(\beta_j^l)^{n+1/2} = ((\alpha_j^l)^{n+1} - (\alpha_j^l)^n)/\Delta\, t$ and summing over all j, l we obtain

$$
\begin{aligned}
D\,(w^{n+1/2},v^{n+1/2})_2 \;+\; N^{n+1/2}\,(w^{n+1/2},v^{n+1/2})_1 \;+\; m\,(v^{n+1}-v^{n},v^{n+1/2})_0 \quad &= \\
= \quad -\Delta t \sum_{e_{ij}\subset\Gamma_{FS}} \Delta\xi_{ij}\,(p_{ij}^{n+1/2}-p_\infty)\,\frac{1}{2}\left\{\frac{w^{n+1}(\xi_{l,ij})-w^{n}(\xi_{l,ij})}{\Delta t}\right. &\quad + \\
+ \quad \left.\frac{w^{n+1}(\xi_{r,ij})-w^{n}(\xi_{r,ij})}{\Delta t}\right\} &.
\end{aligned}
$$

From the third equation of (4.15) we have

$$
w^{n+1}-w^{n} \quad = \quad \Delta t\, v^{n+1/2}\ .
$$

Differentiating with respect to x, multiplying by $(\alpha_j^l)^{n+1/2}\phi_j^l$, respectively its derivatives, and summing over all j,l gives

$$
\frac{1}{2}\,(w^{n+1}-w^{n},w^{n+1}+w^{n})_k \quad = \quad (v^{n+1/2},w^{n+1/2})_k \qquad \text{for} \quad k=0,1,2\,,
$$

or

$$
\frac{1}{2}\,\left\{(w^{n+1},w^{n+1})_k-(w^{n},w^{n})_k\right\} \quad = \quad (v^{n+1/2},w^{n+1/2})_k \qquad \text{for} \quad k=0,1,2\ .
$$

Note that $N^{n+1/2}=\frac{E\,h}{2\,l}\left\{(w^{n+1},w^{n+1})_1+(w^{n},w^{n})_1\right\}/2$ and thus

$$
\begin{aligned}
N^{n+1/2}\,(w^{n+1/2},v^{n+1/2})_1 \quad &= \quad \frac{E\,h}{2\,l}\,\frac{(w^{n+1},w^{n+1})_1+(w^{n},w^{n})_1}{2}\,\frac{(w^{n+1},w^{n+1})_1-(w^{n},w^{n})_1}{2} \\
&= \quad \frac{E\,h}{2\,l}\,\frac{(w^{n+1},w^{n+1})_1^2-(w^{n},w^{n})_1^2}{4} \qquad .
\end{aligned}
$$

The discrete panel energy

$$
E_S^n \quad \equiv \quad \frac{m}{2}\,(v^{n},v^{n})_0 + \frac{E\,h}{2\,l}\left(\frac{(w^{n},w^{n})_1}{2}\right)^2 + \frac{D}{2}\,(w^{n},w^{n})_2\ ,
$$

the energy change on the discrete level is

$$
\begin{aligned}
&E_S^{n+1}-E_S^{n} \quad = \\
&= \quad \textstyle\sum_{e_{ij}\subset\Gamma_{FS}} \frac{\Delta\xi_{ij}\,(p_\infty-p_{ij}^{n+1/2})}{2}\,\left\{w^{n+1}(\xi_{l,ij})-w^{n}(\xi_{l,ij})\;+\;w^{n+1}(\xi_{r,ij})-w^{n}(\xi_{r,ij})\right\}\ .
\end{aligned}
\tag{4.19}
$$

Now, from (4.16), (4.17), and (4.19) we see that in the energy change of the discrete fluid-structure-system, $E_F^{n+1}+E_S^{n+1}-(E_F^{n}+E_S^{n})$, the contributions from the interface cancel, so that the following theorem holds:

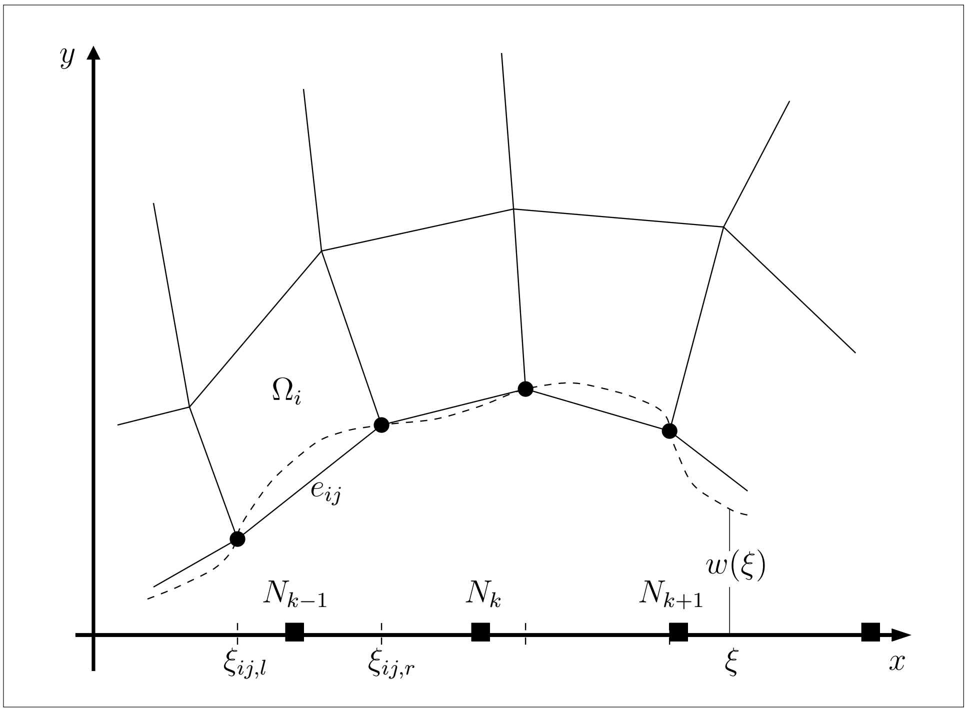

Figure 4.6: Representation of the interface in fluid and structure, N_{k-1}, N_k, N_{k+1} are panel nodes

Theorem 2: The numerical scheme

$$\left.\begin{array}{l} |\Omega_i^{n+1}|\,U_i^{n+1} \;-\; |\Omega_i^n|\,U_i^n \;+ \\ \qquad +\;\; \Delta t \sum_{e_{ij}\subset\partial\Omega_i} |e_{ij}^{n+1/2}|\,F(U_{ij}^{n+1/2}, U_{ji}^{n+1/2}, \dot{\boldsymbol{x}}_{ij}^{n+1/2}, \boldsymbol{n}_{ij}^{n+1/2}) \;\;=\;\; 0\;, \\ \qquad \text{with the boundary treatment (4.13),} \\ \boldsymbol{x}_{ij,l}^n \;=\; (\xi_{ij,l}, w^n(\xi_{ij,l}))^T\,, \quad \boldsymbol{x}_{ij,r}^n \;=\; (\xi_{ij,r}, w^n(\xi_{ij,r}))^T \\ \qquad \text{for all flow edges on the panel,} \end{array}\right\} \quad (4.20)$$

$$\left.\begin{array}{l} D\,(w^{n+1/2},\phi_j^l)_2 \,+\, N^{n+1/2}\,(w^{n+1/2},\phi_j^l)_1 \,+\, m\,(v^{n+1}-v^n,\phi_j^l)_0 \;\;= \\ \qquad =\;\; -\,\Delta t \sum_{e_{ij}\subset\Gamma_{FS}} \Delta\xi_{ij}\, p_{ij}^{n+1/2}\,\left\{\phi_j^l(\xi_{l,ij}) + \phi_j^l(\xi_{r,ij})\right\}/2 \qquad \forall\, j,l\;, \\ (\alpha_j^l)^{n+1} - (\alpha_j^l)^n \;\;=\;\; \Delta t\,(\beta_j^l)^{n+1/2} \qquad \forall\, j,l\;, \end{array}\right\} \quad (4.21)$$

approximating the aeroelastic initial-boundary-value-problem of Chapter 2 satisfies the GCL in the fluid and has a correct energy transfer at the fluid-structure interface.

Remark:

We have compared each coupling scheme in combination with the conservative load projection of Sec. 4.4.2 and the one given in Theorem 2. These comparisons of the load projection strategies did not show a notable difference in the results. The significant *practical* issue in the scheme with conservative energy transfer is its characteristic property as a tight coupling scheme, namely the removement of the time lag present in the loose coupling, which comes along with a high order time discretization at the interface. This is demonstrated through various numerical experiments in Chapter 6.

Chapter 5

The Solution Algorithm

In the first section the solution algorithm for the discretized fluid equations on moving grids is discussed in detail. The basic methodology is to use a matrix–free Newton–GMRes iteration to solve the set of nonlinear equations in each time step approximately. This strategy was also used in [43], [44], [53] in the context of compressible flows. This method is also used to solve the structural equations (Sec. 5.2). One may alternate between the obtained fluid solver and structural solver, performing a loose or staggered coupling or a tight coupling with fixed–point–iteration (FPI), to approximate the solution of a fluid-structure-interaction. The matrix–free Newton–GMRes can also be applied on the coupled set of discrete fluid-structure-equations from Theorem 2, which is explained in Sec. 5.3. Finally we discuss the convergence criterion used in the tight coupling for both the FPI and the Newton iteration (Sec. 5.4).

5.1 Matrix–free Newton–GMRes for the discrete fluid system

The space-discretized equations (4.3) of the fluid may shortly be written as

$$Vol^{n+1}\,U^{n+1} \;-\; Vol^{n}\,U^{n} \;+\; \int_{t^n}^{t^{n+1}} \mathcal{F}(\mathcal{U},x,\dot{x})\;dt \quad = \quad 0\;.$$

Here U, respectively $\mathcal{U}$, contain the conservative, respectively the primitive, state vectors of all cells and $\mathcal{F}(U,x,\dot{x})$ contains the discrete version of the boundary integrals for all cells. In the diagonal matrix Vol^n we collect all cell volumes. x represents the whole grid geometry, i.e. vertex coordinates, normals and so on, and $\dot{x}$ the grid velocities. I.e. for the cell Ω_i this system of equations contains (in 2D) the set of 4 equations

$$|\Omega_i^{n+1}|\,U_i^{n+1} - |\Omega_i^{n}|\,U_i^{n} \;+\; \int_{t^n}^{t^{n+1}} \mathcal{F}_i(\mathcal{U},x,\dot{x})\;dt \quad = \quad 0\;.$$

Of course, $\mathcal{F}_i$ depends on the state U_i and the states U_j of cells Ω_j lying in a neighborhood of Ω_i. The size of this neighborhood is related to the order of the spacial discretization.

Here we have a second order spacial discretization. The vertex velocities within each time step are constant, given by $\dot{x}^{n+1/2} = (x^{n+1} - x^n)/\Delta t$. Different second order time integration schemes are implemented, an explicit second order Runge-Kutta scheme and two implicit schemes, the trapezoidal and the mid-point rule. Here we present the solution algorithm for the general implicit scheme

$$\begin{aligned} & |\Omega_i^{n+1}|\, U_i^{n+1} \;-\; |\Omega_i^n|\, U_i^n \;+ \\ + \;\; & (1-\alpha)\,\Delta t\, \mathcal{F}_i(\mathcal{U}^{n+1}, x^{n+1}, \dot{x}^{n+1/2}) \;+\; \alpha\,\Delta t\,\mathcal{F}_i(\mathcal{U}^n, x^n, \dot{x}^{n+1/2}) \;=\; 0\,. \end{aligned} \tag{5.1}$$

At each time step we solve this system for U^{n+1} by a Newton-iteration. The iteration runs in primitive variables $\mathcal{U}$, so a Newton-step is to solve *approximately*

$$\left[Vol^{n+1} \frac{\partial U}{\partial \mathcal{U}} \;+\; \Delta t\,(1-\alpha) \frac{\partial\, \mathcal{F}(\mathcal{U}, x^{n+1}, \dot{x}^{n+1/2})}{\partial \mathcal{U}} \right]_{\mathcal{U}^*} \Delta\mathcal{U} \;=\; rhs(\mathcal{U}^*) \tag{5.2}$$

and update $\mathcal{U}^* = \mathcal{U}^* + \Delta\mathcal{U}$, where

$$\begin{aligned} rhs(\mathcal{U}^*) \;&= \\ &= \; -Vol^{n+1}\, U^* + Vol^n\, U^n \;-\; \Delta t\,(1-\alpha)\,\mathcal{F}(\mathcal{U}^*, x^{n+1}, \dot{x}^{n+1/2}) \;-\; \Delta t\,\alpha\,\mathcal{F}(\mathcal{U}^n, x^n, \dot{x}^{n+1/2})\,. \end{aligned}$$

As initial guess we use $\mathcal{U}^* = \mathcal{U}^n$ and if a stopping criterion such as

$$||rhs(\mathcal{U}^*)||_2 < \varepsilon_{nonlin} \cdot ||rhs(\mathcal{U}^n)||_2 \qquad \text{or} \qquad ||rhs(\mathcal{U}^*)||_2 < \alpha_{nonlin}$$

is satisfied, we set $\mathcal{U}^{n+1} = \mathcal{U}^*$ and proceed to the next time step.

Let A denote the Jacobian–matrix [....] appearing in equation (5.2). Combining the Newton-iteration with an iterative linear solver such as GMRes, where A contributes only in multiplications of A with vectors [54], one may avoid the calculation and the storage of the matrix A by employing an approximation. Namely, in the present case, the matrix–vector–product can be approximated by a simple difference formula

$$\begin{aligned} A\mathcal{V} \;&\approx \\ &\approx \; Vol^{n+1} \frac{\partial U}{\partial \mathcal{U}}\Big|_* \mathcal{V} \;+\; \frac{\Delta t\,(1-\alpha)}{\varepsilon} \left(\mathcal{F}(\mathcal{U}^* + \varepsilon\mathcal{V}, x^{n+1}, \dot{x}^{n+1/2}) \;-\; \mathcal{F}(\mathcal{U}^*, x^{n+1}, \dot{x}^{n+1/2}) \right)\,. \end{aligned}$$

Of course, a difficulty with this approach lies in the choice of ε, which should be a good compromise, such that the derivative is approximated well and cancellation is avoided. In [53] several proposals for ε from the literature are given; throughout, in all kinds of Newton–GMRes iterations, we have used the simplest choice, which was also preferred by the authors of [53]:

$$\varepsilon \;=\; \frac{\text{eps}^{1/2}}{||\mathcal{V}||_2} \qquad \text{where eps is the machine-accuracy}$$

5.1.1 Iterating with low and high order spacial resolution

Let us denote the l.h.s. of equation (5.1) by $\mathcal{G}_2$, respectively $\mathcal{G}_1$, if the order of the spacial discretization in $\mathcal{F}$ is two, respectively one. The matrix–free methods corresponding to the Newton schemes

$$\mathcal{G}_1'(\mathcal{U}^*)\,\Delta\mathcal{U} \;=\; -\mathcal{G}_2(\mathcal{U}^*)\;,\quad \mathcal{U}^* \;=\mathcal{U}^*+\Delta\mathcal{U} \tag{5.3}$$

and

$$\mathcal{G}_2'(\mathcal{U}^*)\,\Delta\mathcal{U} \;=\; -\mathcal{G}_2(\mathcal{U}^*)\;,\quad \mathcal{U}^* \;=\mathcal{U}^*+\Delta\mathcal{U} \tag{5.4}$$

are implemented. Scheme (5.4) is the classical Newton scheme. Scheme (5.3) turns out to be much more robust and it is also cheaper, since reconstruction and limitation do not contribute in the matrix–free evaluation of the matrix–vector –product. It has frequently been observed, that when convergence stalled it was safer to iterate with (5.3), since in such instances (5.4) tended to shoot into ranges of negative density or pressure. So usually the nonlinear iteration is started with (5.3) and changes to (5.4) after a certain accuracy is reached. When no troubles occur, it can be seen that (5.4) converges much faster.

5.1.2 Preconditioning

It is well known that preconditioning can drastically improve the convergence of GMRes [54] and its successful application within compressible flow solvers was shown in [43], [65]. For the purpose of preconditioning, we have to find a computationally cheap way to roughly invert the equation $A\mathcal{V} = b$. This is achieved by

- considering $\tilde{A}\mathcal{V} = b$ instead, where $\tilde{A} = \mathcal{G}_1'(\mathcal{U}^*)$ and for the purpose of preconditioning the van-Leer flux vector splitting is used in $\mathcal{G}_1$ (this is very efficient and rather simple to implement) and
- performing a single (block) Symmetric Gauss-Seidel (SGS) sweep on $\tilde{A}\mathcal{V} = b$, i.e. solving
$$(\tilde{D}+\tilde{L})\,\tilde{D}^{-1}(\tilde{D}+\tilde{R})\,\mathcal{V} \;=\; b$$
- for a *renumbered* version of the equations, which results from the application of the Reverse-Cuthill-MacKee (RCM) Algorithm on the cell connectivity .

The blocking is cell–wise, the calculation of the matrix blocks is presented below.

Amongst others, the use of SGS for preconditioning in compressible flow solvers was also proposed in [43], [44]. It is well known that the RCM-renumbering can accelerate the convergence of such approximate factorization methods as SGS or the Incomplete Lower Upper factorization (ILU). Renumbering strategies were also applied to compressible flow solvers in [65]. The RCM-renumbering is explained in [5].

A preconditioning consistent with memory savings of a matrix–free approach should of course use only memory that is small compared to the memory that would be needed for the Jacobian. In fact in SGS only the diagonal blocks need to be calculated and the multiplications with the remaining blocks may also be performed in a matrix–free fashion, see [43]. Here we store the diagonal blocks, $\tilde{D}$, and calculate the blocks of $\tilde{L}$ and $\tilde{R}$ when needed.

Calculation of Preconditioning blocks

The 4×4 blocks in the matrix $\tilde{A}$ are obtained from a first order version of $\mathcal{F}$ with the van-Leer flux vector splitting. This approximation of $\mathcal{F}_i$ is (for a cell away from the boundary)

$$\mathcal{F}_i \overset{1st\ order}{=} \sum_{e_{ij} \subset \partial\Omega_i} |e_{ij}|\ S_{ij}\, Q_{ij} \Big(f^+(Q_{ij}^{-1}(\mathcal{U}_i - \dot{X}_{ij})) + f^-(Q_{ij}^{-1}(\mathcal{U}_j - \dot{X}_{ij})) \Big) \ ,$$

with the split fluxes f^+ and f^- from equation (4.7).

Finally, the Jacobian blocks according to this spacial discretization are obtained from the derivative

$$\frac{\partial\, S\, Q\, f^{\pm}(Q^{-1}(\mathcal{U} - \dot{X}))}{\partial \mathcal{U}} \ .$$

Let us introduce some abbreviations,

$$\begin{array}{rcl} \lambda^{\pm} & = & v_n - \dot{x}_n \pm c \\ f_m^{\pm} & = & \pm\, \rho\, (\lambda^{\pm})^2/(4\, c) \\ C^{\pm} & = & \big((\gamma - 1)\,(v_n - \dot{x}_n) \pm 2\, c\big)/\gamma \\ \kappa_{vl} & = & 0.5\, \gamma^2/(\gamma^2 - 1) \\ M & = & (v_n - \dot{x}_n)/c \end{array}$$

so that together with (4.7) we get

$$f^{\pm}(Q^{-1}(\mathcal{U} - \dot{X})) \quad = \quad f_m^{\pm} \cdot \begin{pmatrix} 1 \\ C^{\pm} \\ v_\tau - \dot{x}_\tau \\ \kappa_{vl}\, (C^{\pm})^2 \end{pmatrix}$$

in the case $|M| < 1$. Thus, essentially we have to find the derivatives of $f_m^{\pm}$ and $C^{\pm}$, which are

$$\frac{\partial\, f_m^{\pm}}{\partial \mathcal{U}} \quad = \quad \left(\frac{\lambda^{\pm}}{8}\,(1 \pm 3\, M),\ \frac{\rho\, cos}{2}\,(1 \pm M),\ \frac{\rho\, sin}{2}\,(1 \pm M),\ \frac{\rho\, \lambda^{\pm}}{8\, p}\,(1 \mp M) \right)$$

and

$$\frac{\partial\, C^{\pm}}{\partial \mathcal{U}} \quad = \quad \left(\mp\, \frac{c}{\gamma\, \rho},\ \frac{\gamma - 1}{\gamma}\, cos,\ \frac{\gamma - 1}{\gamma}\, sin,\ \pm\, \frac{c}{\gamma\, p} \right) \ .$$

In the case $|M| \geq 1$ the flux is either 0 or the flux of the Euler equations $f(U, \dot{\boldsymbol{x}})\, \boldsymbol{n}$, compare (2.2), and the derivative is easily found.

5.2 Matrix–free Newton–GMRes for the discrete structural system

Given the loads p_1, p_2, at each time step, the discrete structural system (4.15) is a nonlinear system of equations for the unknown vector containing the coefficients $(\alpha_i^k)^{n+1}$, $(\beta_i^k)^{n+1}$. The coefficients are blocked node–wise and collected in the vector

$$\mathcal{W} \quad \equiv \quad (...., \alpha_i^0, \beta_i^0, \alpha_i^1, \beta_i^1, ...)^T,$$

where the 4 coefficients of an (inner) node are shown. The nonlinear system for $\mathcal{W}^{n+1}$ is also solved with the matrix–free Newton–GMRes using a block–Jacobi preconditioner.

5.3 Matrix–free Newton–GMRes for the discrete fluid-structure system

The discrete fluid–structure system from Theorem 2 (sec 4.4) to be solved at each time step may be written in compact form as

$$\mathcal{H}(\mathcal{U}^{n+1}, \mathcal{W}^{n+1}; \mathcal{U}^n, \mathcal{W}^n) \quad \equiv \quad \begin{pmatrix} \mathcal{H}_F(\mathcal{U}^{n+1}, \mathcal{W}^{n+1}; \mathcal{U}^n, \mathcal{W}^n) \\ \mathcal{H}_S(\mathcal{U}^{n+1}, \mathcal{W}^{n+1}; \mathcal{U}^n, \mathcal{W}^n) \end{pmatrix} \quad = \quad 0 \; .$$

Here the states of fluid $\mathcal{U}^n$ and structure $\mathcal{W}^n$ at the beginning of the time step are given. We have to solve for $\mathcal{U}^{n+1}$ and $\mathcal{W}^{n+1}$. In the evaluation of the structural equations $\mathcal{H}_S$ only the (reconstructed) pressures from the fluid states $\mathcal{U}^{n+1}$, $\mathcal{U}^n$ are needed to determine the loads, whereas in $\mathcal{H}_F$ only the deflections from $\mathcal{W}^{n+1}$, $\mathcal{W}^n$ are needed to determine the fluid grid positions at the new and old time level which define the grid velocities.

When the spacial fluid discretization is of second order, the reconstructed fluid pressures are only available when the grid is defined, which in turn depends on the structural deflection. Thus an evaluation of $\mathcal{H}$ proceeds as follows:

- determine the new grid from $\mathcal{W}^{n+1}$
- determine the grid velocities
- reconstruct and limit
- determine the fluxes
- $\mathcal{H}_{\mathcal{F}}$ is given according to (4.20)
- from the reconstructed pressure determine the structural load
- $\mathcal{H}_{\mathcal{S}}$ is given according to (4.21)

Again we employ a matrix–free Newton GMRes iteration, using

$$\mathcal{H}'(\mathcal{U}^*, \mathcal{W}^*; \mathcal{U}^n, \mathcal{W}^n) \begin{pmatrix} \mathcal{V}_F \\ \mathcal{V}_S \end{pmatrix} \quad \approx$$

$$\approx \quad \frac{1}{\varepsilon}\left(\mathcal{H}(\mathcal{U}^* + \varepsilon\,\mathcal{V}_F,\, \mathcal{W}^* + \varepsilon\,\mathcal{V}_S;\, \mathcal{U}^n, \mathcal{W}^n) - \mathcal{H}(\mathcal{U}^*,\, \mathcal{W}^*;\, \mathcal{U}^n, \mathcal{W}^n) \right)$$

Especially at this point the currently implemented version is far from efficient. For example, it should suffice to perturb the fluid grid in the evaluation of

$$\mathcal{H}_F(\mathcal{U}^* + \varepsilon\,\mathcal{V}_F,\, \mathcal{W}^* + \varepsilon\,\mathcal{V}_S;\, \mathcal{U}^n, \mathcal{W}^n)$$

only in a neighbourhood of the structure to catch the significant part of $\mathcal{H}$'s Jacobian!

We may also switch to a method that uses only the first order spacial fluid discretization in the Jacobian, as discussed in Sec. 5.1.1.

The preconditioning is done in a decoupled fashion. This means that the equation $\mathcal{H}'(\mathcal{V}_F, \mathcal{V}_S)^T = (b_F, b_S)^T$ is "roughly inverted" by employing the fluid preconditioner of Sec. 5.1.2 to the r.h.s. b_F to obtain $\mathcal{V}_F$ and the structural preconditioner of Sec. 5.2 to the r.h.s. b_S to obtain $\mathcal{V}_S$. This point may also be subject to further improvements.

As an initial guess for the Newton–iteration the result of a loose coupling step is used. This loose coupling step may be varied to be well or not so well converged in the two media. A cheap interpolation from previous time steps may also be a good option to obtain an initial guess, but this variant has not been implemented yet.

5.4 Convergence criterion for tight coupling

The convergence criterion is to reduce the residual in the tightly coupled structural equation (4.21) under a given threshold, no matter whether we use the fixed–point–iteration or the Newton–iteration described above. When employing a loose coupling (Fig. 4.3) as an initial guess the structural equation of the loose coupling may be well converged, but this is not equation (4.21). Thus when plugging the initial guess into (4.21) the residual increases immensely. In the following iteration this residual is then reduced by a factor around 10^{-2}. In the fluid equation the changes are not so drastic, the residual may even increase without worsening the result, since the fluid equations of the loose coupling step are the same as those in the tightly coupled version (4.20).

Chapter 6

Numerical Experiments

The main objective of the numerical experiments presented in this Chapter is to examine the influence of the numerical coupling procedures on the obtained approximate solutions and to prove the feasibility of the tight coupling via a matrix–free Newton–iteration of the coupled fluid–structure system. Further, we want to find insight into typical behaviours of the numerical simulations and the limitations of the algorithms. It is not the primary target to compare the different algorithms with respect to efficiency, but we keep an eye on this issue.

All computations were performed in the regime $0.7 < M_\infty < 1.3$, where the panel flutter problem has its severest nonlinearities. Let us distinguish three categories of physical behaviour, namely

- transonic flutter,
- supersonic flutter,
- aeroelastic cases with a steady state (divergence or stable behaviour).

In the latter category the transient phase that leads to the steady state may exhibit phenomena similar to those appearing periodically in the other two categories. To the knowledge of the author, panel flutter with purely subsonic flow has not been observed yet. Transonic and supersonic flutter cases were found to be of different severity for the numerical algorithm. A typical difference found in the solution, is that in transonic flutter cases shock movements are present on the panel, whereas in the supersonic flutter cases the fluid solution remains smooth along the panel.

These principle differences between transonic and supersonic flutter cases are shown in Sec. 6.2. Convergence behaviour of the coupling algorithms with respect to Δt is also found in Sec. 6.2. The fixed–point–iteration (FPI) and the Newton–iteration, which are employed in each time step to achieve a tight coupling, are compared with respect to their convergence properties in Sec. 6.3. In Sec. 6.4 the effect of the different coupling algorithms on the aeroleastic solutions is investigated, where locations of bifurcations in parameter space are demonstrated to depend on the coupling scheme. Finally, in Sec. 6.5

we determine the stability boundary of an aluminium panel, and compare it to results from the literature.

6.1 Parameters of numerical schemes

Let us discuss the numerical parameters that influence and control the computations.

Grid: The panel flutter problem has a simple geometry; a structured fluid grid with quadratic cells in the neighbourhood of the panel may be used, as was done here. The grid is mainly determined by the number of cells on the panel and the distance from the panel to the artificial boundaries. In the literature 50 to 100 cells were used on the panel [33], [14], whereas we have found that 50 fluid cells may suffice to produce good results when looking at the panel deflections, although the solution in the fluid does not look satisfactory. 80 cells on the panel were seen to be a sufficient choice. Grid convergence studies for the panel flutter problem conducted in [33], using 48, 96 and 200 cells on the panel showed that sometimes 48, but definitely 96 cells on the panel were enough, which confirms our choice.

A complete fluid grid with 80 cells on the panel and a total of 8998 cells is shown in Fig. 6.1; the cells are stretched away from the panel, compare the details given under Fig. 6.1. An enlarged view of the grid around the trailing edge of the deformed panel is shown in Fig. 6.2. This grid was used in all experiments presented here. Let us note that, although the grid is logically cartesian in this case, we have a fully unstructured algorithm with unstructured discretization concepts for further developments.

In the structure we have used 26 nodes, whereas 11 to 26 were used in [14] and up to 41 in [33].

Time step size and order: The time step size Δt is dictated by the physical time scales present on the one hand, i.e. by a targeted time accuracy, and on the other hand by the stability requirements of the scheme. When an explicit method is applied, the stability condition of the time-integration scheme can be very restrictive. For the implicit methods employed, *formally* there are no *linear* stability conditions; but the sufficient convergence of the *nonlinear* iteration needed in each time step may restrict the time step size. In order to better compare the different schemes, we only present computations that were run with fixed Δt. All calculations were performed with fluid and structural codes of second order in time.

CFL number: Of course, when an implicit algorithm is good enough to use large time step sizes that correspond to an appropriate temporal resolution, the corresponding CFL number may heavily depend on the given grid. Here a reliable CFL number was found to be 7, which corresponds to a dimensionless time step size $\Delta t/t^*$ around 0.04. In some cases CFL numbers of up to 40 could produce satisfactory results. In [27] $\Delta t/t^* = 0.02$ was used with 50 cells on the panel, whereas in [33] $\Delta t/t^*$ around 0.05 and up to 0.2 brought good results with 96 cells on the panel.

Preconditioner: The performance of Newton–GMRes iterations in implicit schemes may be drastically influenced by the preconditioner, thus influencing the time step size.

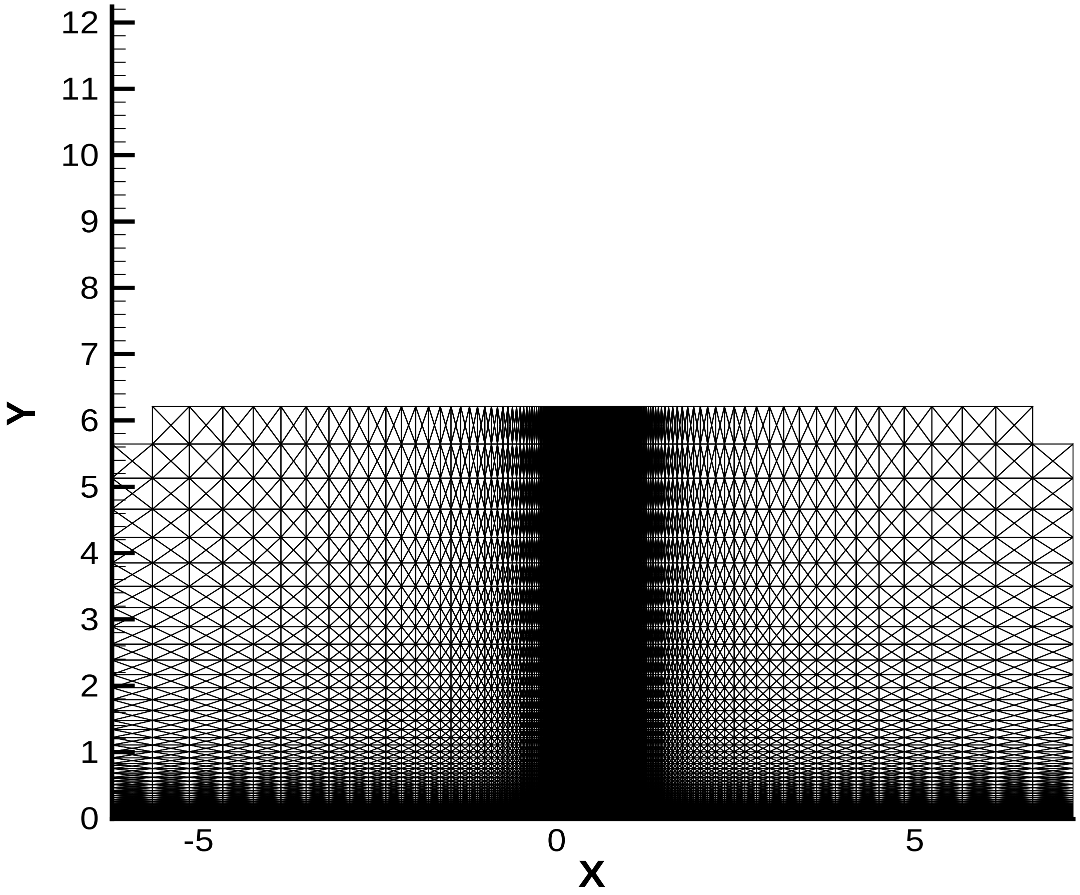

Figure 6.1: 8998 quadrilateral cells are in the fluid grid, 80 of them are in contact with the panel, which is located on the x-axis between $x = 0$ and $x = 1$. The triangles seen in the picture are artificially produced. In order to match our data structure with the visualization tool each quadrilateral cell is divided into 4 triangles. On the panel we have equally spaced quadratic cells with edge lengths $\Delta x = \Delta y$. Δx remains constant another 10 cell columns in front and behind the panel and Δy remains constant 10 cell rows above the panel. Then the edge lengths grow from row to row, respectively column to column, by a factor of 1.1 up to the artificial boundaries.

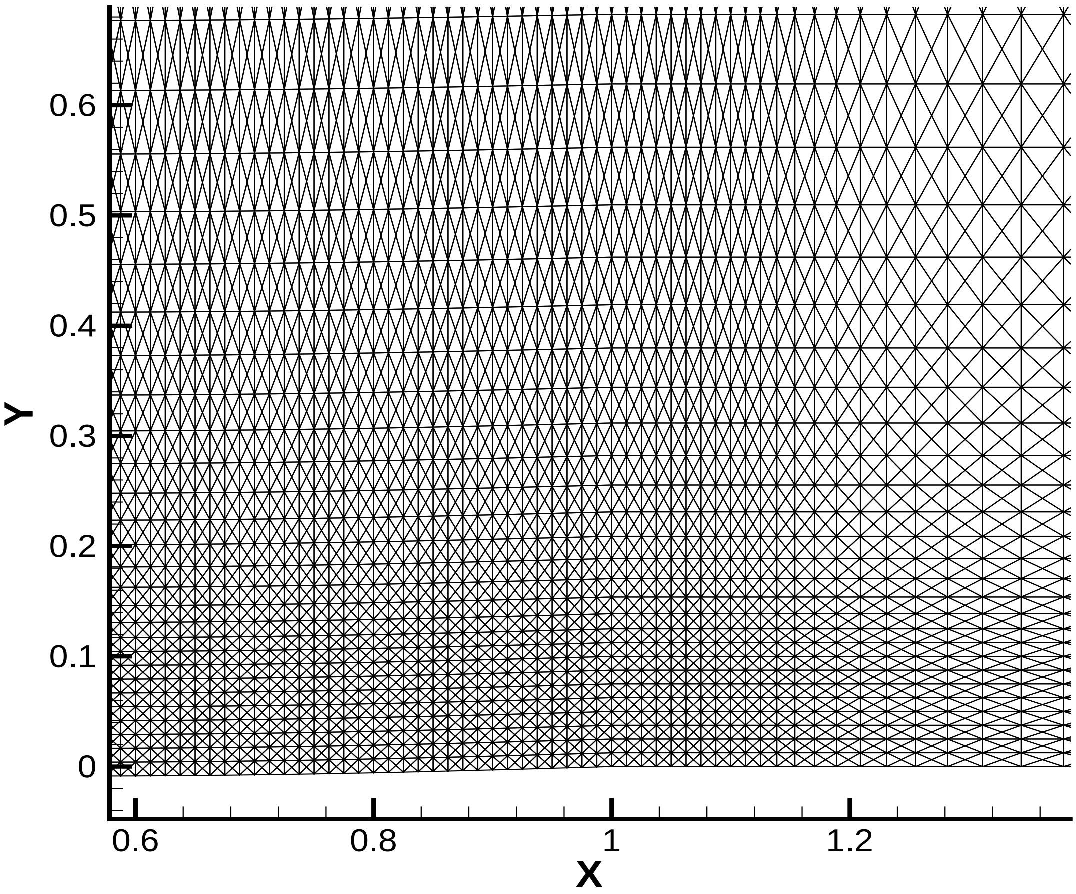
0.6
0.5
0.4
Y
0.3
0.2
0.1
0
0.6
0.8
1
1.2
X

Figure 6.2: An enlargement of the grid around the deformed panel trailing edge is shown.

As described in Chapter 5, we have used the Block–SGS preconditioner in the fluid and the Block–Jacobi preconditioner in the structure.

Let us introduce notations for some significant quantities appearing in the numerical tests below.

T_F	flutter period, a relevant time scale of a limit cycle oscillation
CFL	CFL-number in the fluid
α	*absolute* residual threshold in any kind of iteration, threshold below which the residual has to drop
ε	*relative* residual threshold in any kind of iteration, threshold below which the residual divided by the initial residual has to drop
ε_l	relative residual threshold in (linear) GMRes iteration
α_{nl}, ε_{nl}	absolute and relative residual thresholds in (nonlinear) Newton iteration
α^F, ε^F	absolute and relative residual thresholds in fluid system
α^S, ε^S	absolute and relative residual thresholds in structural system
$\overline{\alpha}$, $\overline{\varepsilon}$	absolute and relative residual thresholds in the tightly coupled fluid–structure system

6.2 Typical computations and convergence in Δt

Here we present two typical cases showing the relation of primary parameters such as the CFL number, residual thresholds and the number of iterations.

Initial condition: Initially, the complete fluid domain is filled with the inflow state, the panel is undeflected and provided with a sinusoidal velocity distribution over the length of the panel with $0.005 \cdot u_\infty$ as velocity peak.

Fluid iteration: A typical relative residual threshold used in the literature, e.g. [66], for unsteady aerodynamic applications is $\varepsilon_{nl}^F = 0.01$ and as initial guess for the fluid state at the end of the time step, one takes the given fluid state at the beginning of the time step. Here we use the same initial guess and assign $\alpha_{nl}^F = 10^{-6}$, which generally corresponds to $\varepsilon_{nl}^F = 0.01$. In a Newton step in the (separate) fluid algorithm, a maximum number of 30 GMRes iterations is possible. Actually, when iterating with the low order Jacobian (5.3), we assign $\varepsilon_l^F = 0.1$ and need only a single GMRes iteration. Increasing ε_l^F does not improve anything for the nonlinear iteration, which is not surprising, due to the inexact linearization. When iterating with the high order Jacobian (5.4), it always takes less than 15 GMRes iterations to reach the assigned threshold of $\varepsilon_l^F = 10^{-3}$. The nonlinear iteration in the fluid is sometimes not satisfactory. As will be seen throughout the examples presented, this did not have a bad effect on the obtained results, as seen through convergence studies in Δt.

Structural iteration: In the (separate) structural algorithm, we have very few unknowns and it is very easy to reduce the residual to machine accuracy, which is practically done, by setting $\alpha_{nl}^S = 10^{-12}$.

Iteration to achieve tight coupling: Here the convergence criterion is assigned in terms of $\overline{\alpha}^S$, which corresponds to an $\overline{\varepsilon}^S \leq 0.1$. The maximum number of fluid–

structure–loops is usually 3. Using the FPI, a fluid–structure–loop contains a time step iteration of the fluid code with $\alpha_{nl}^{F} = 10^{-6}$ and a time step iteration of the structural code with $\alpha_{nl}^{S} = 10^{-12}$. Using the Newton–iteration, a fluid–structure–loop is a Newton–step applied to the tightly coupled fluid–structure equations. Here $\overline{\varepsilon}_{l}^{FS} = 10^{-2}$ is used for the linear solver. In the transonic flutter case presented in Sec. 6.2.1 below, this results in 5 GMRes iterations at CFL = 7 and 10 GMRes iterations at CFL = 15. For the number of fluid–structure–loops actually needed, see Sec. 6.3.

6.2.1 Transonic flutter at $M_\infty = 1$

The physical data of this case is given by an aluminium panel, i.e. the material constants given in Sec. 2.1.2, and a panel thickness of $h_{rel} = 0.004537$. The infinity state of the fluid is determined through $\mu = 0.1$, $\lambda = 260$ and $M_\infty = 1$, compare (2.15). After an initial transient phase, the system falls into a limit cycle oscillation. In Fig. 6.3 the panel mid–point deflection is shown over two cycles of the limit cycle oscillation, resulting in a reduced frequency of $k = 0.02$. The periodic panel deflection has evolved in interaction with the fluid, which exhibits a periodic shock movement in the limit cycle. The shock movement along the panel is shown over one cycle in Fig. 6.6.

The result shown in Fig. 6.3 was obtained with a fluid CFL number of 15, which is equivalent to 260 time steps per flutter period. A higher time step size seemed impossible to be achieved with the code. Two facts may indicate why from the physical time scales present, higher time step sizes would not make sense: First, in Fig. 6.4 we see that there are higher harmonics present in the panel, which are visualized by the panel deflections at 25% and 75% chord. Secondly, we wonder how the shock velocity relates to the space–time–grid: The visualization in Fig. 6.6 was obtained with a CFL number of 7; rotating the visualization, such that we look onto the tx–plane, we can see how the shock moves across the space–time–grid in Fig. 6.7. The spacing Δt shown in the figure corresponds to one time step and the spacing Δx corresponds to one edge length of a fluid cell on the panel. We can observe that at the given CFL number it takes five time steps to advance the shock by Δx. This suggests a possible connection between the shock speed and the time step restrictions.

An example showing the convergence history during a single time step in the fluid is given in Fig. 6.5. The slow convergence with the low order Jacobian and the acceleration with the high order Jacobian is clearly seen.

Convergence in Δt

In the upper picture of Fig. 6.8 we see how the time accuracy is lost in the initial transient, when increasing the time step size for the loose coupling. With the tight coupling, here performed via Newton–iteration, this does not happen. A result for the tight coupling is shown with CFL=15. All results obtained with the tight coupling and smaller CFL–numbers do not leave the thick line drawn for CFL=15. At later times, see the lower picture, this fact still holds for the tight coupling. The loose coupling already fails for

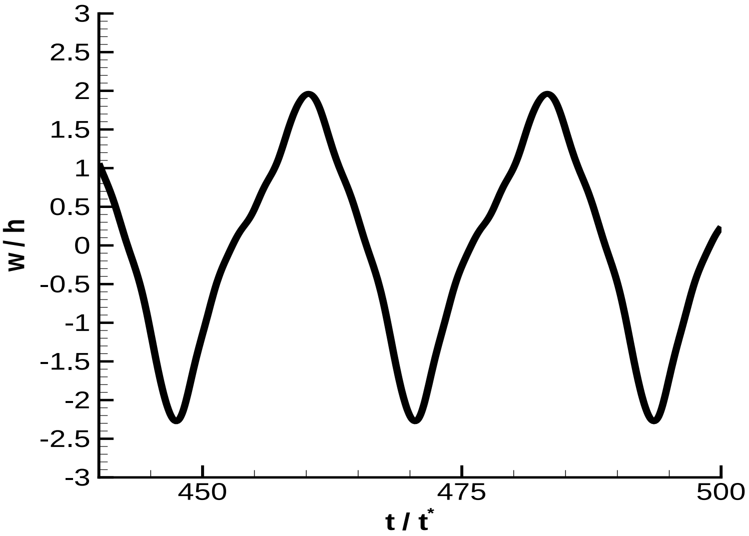

Figure 6.3: $M_\infty = 1$; the panel mid–point deflection is shown over two periods of the limit cycle.

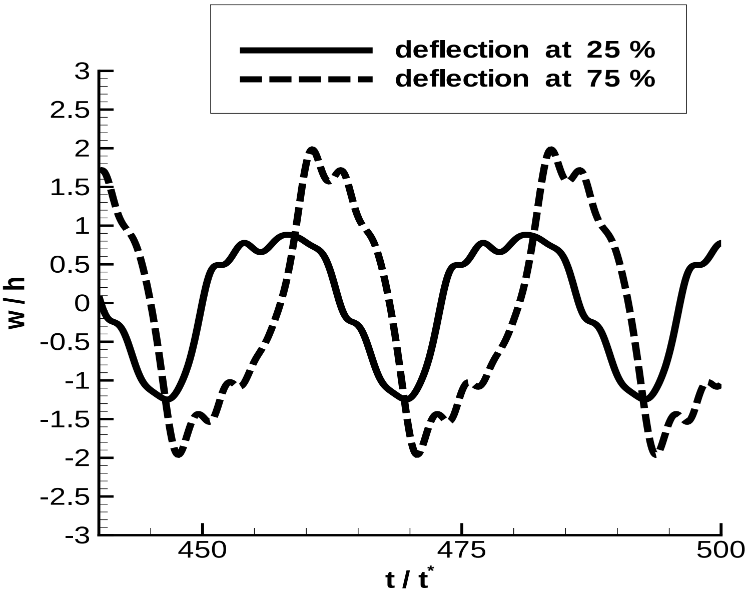

Figure 6.4: $M_\infty = 1$; the panel deflection at 25% and 75% chord is shown, revealing the presence of higher harmonics in the panel.

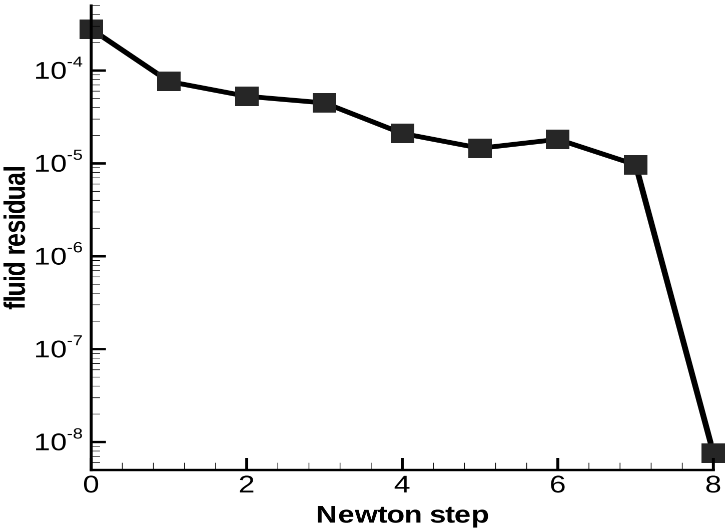

Figure 6.5: $M_\infty = 1$; a typical convergence history for a single time step in the fluid solver at CFL = 7 is shown. We have an initial residual $> 10^{-4}$, then 7 Newton iterations with (5.3) follow, each taking only 1 GMRes–iteration until the residual reaches 10^{-5} and finally a single Newton step of type (5.4) with 7 GMRes–iterations reduces the residual below 10^{-8}.

CFL=7 at some point and thus this solution does not appear in the lower picture. Nevertheless, we can look at the obtained limit cycles, and see how their prediction behaves for different schemes and different Δt. Let us characterize the limit cycle by the deflection amplitude and the flutter period T_F. Convergence in these quantities, measured around $t/t^* = 500$, is shown in Fig. 6.9. It can be observed that the loose coupling and the tight coupling converge practically to the same limit cycle.

6.2.2 Supersonic flutter at $M_\infty = 1.2$

Here we consider an aluminium panel with $h_{rel} = 0.004$, a flow with $M_\infty = 1.2$, and ρ_∞, p_∞ are obtained from the conditions at 20000 feet altitude [36]. In the long time behaviour the system flutters with the panel mid–point deflection as presented in Fig. 6.12. The reduced frequency of the solution is $k = 0.07$. Higher harmonics are less activated in the panel, compared to the transonic case, as seen in Fig. 6.14. Further, the fluid states along the panel remain smooth, which is visualized in Fig. 6.10, where the Mach–number distribution on the panel over a complete flutter cycle can be seen. At the trailing edge a lambda–shock periodically builds up, its feet bend downstream and its head finally swims downstream, until the shock is completely dissolved and then the lambda–shock, shown in Fig. 6.11, builds up again.

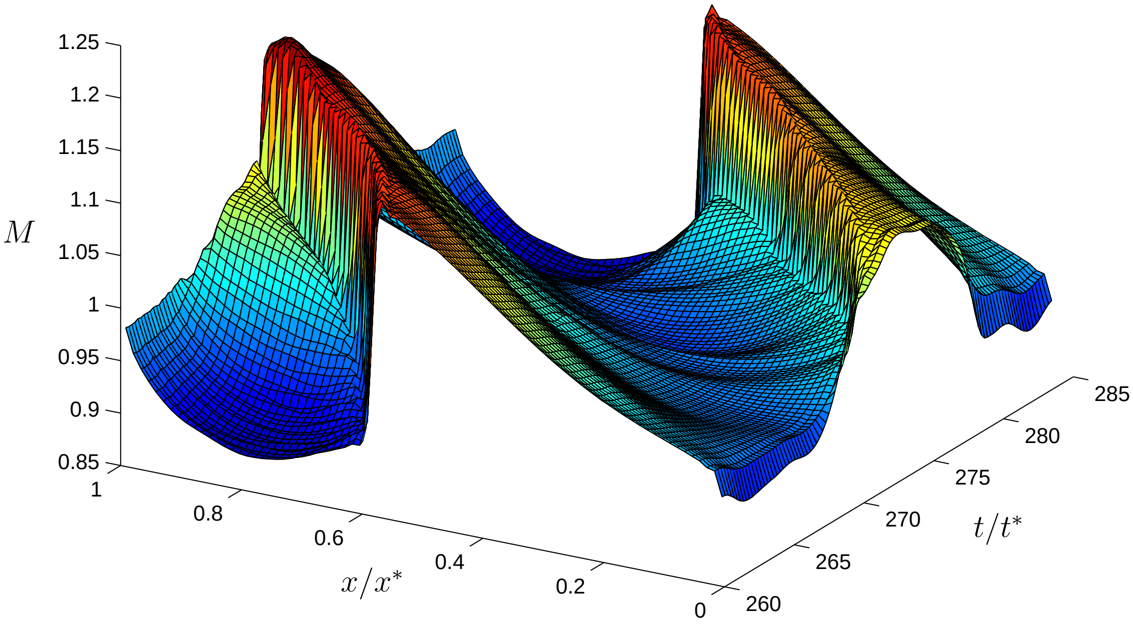

Figure 6.6: $M_\infty = 1$; the evolution of the Mach number along the panel during one period of the limit cycle is seen, showing the shock movement.

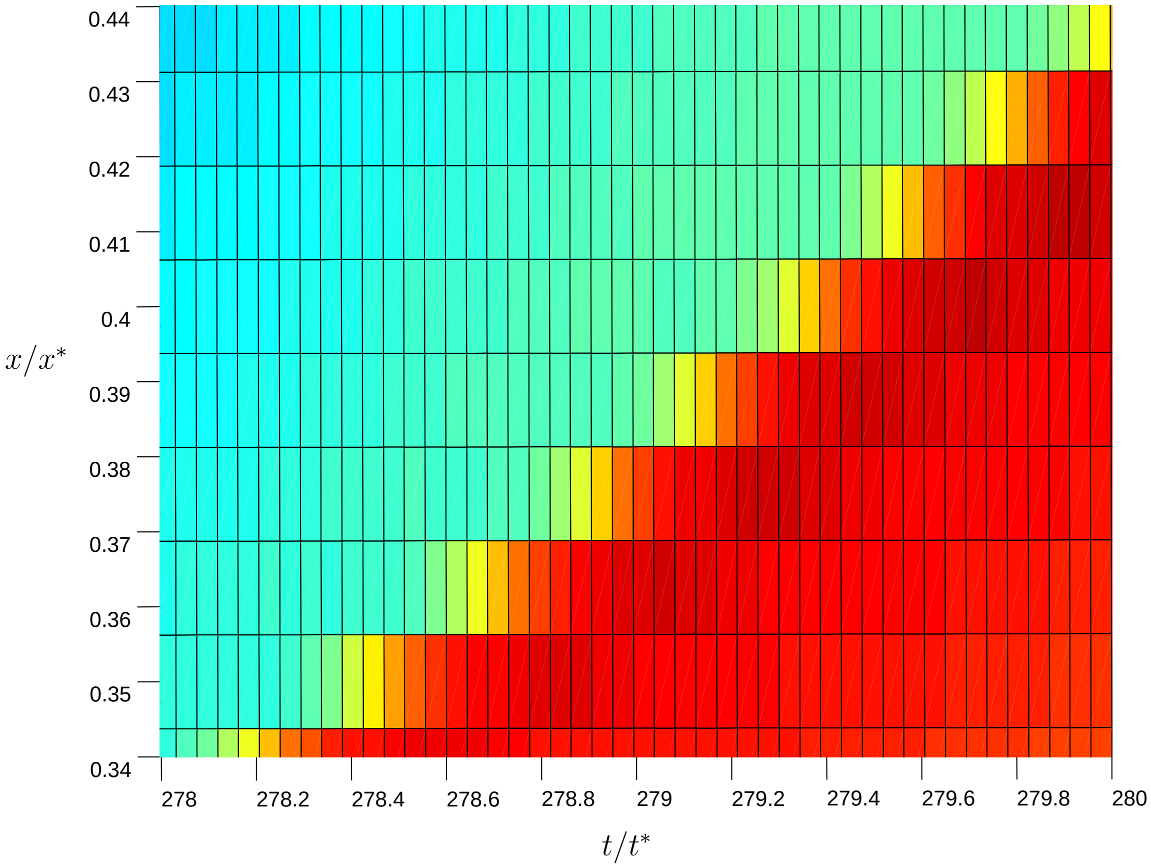

Figure 6.7: $M_\infty = 1$; the shock movement in the limit cycle across the tx–grid is shown. The gray–scale plot gives the Mach–number distribution on the panel between 34% and 44% chord, where the shock reaches its highest velocity. The position of the shock is clearly located, where the sudden change in gray–scale occurs. The grid spacing uses a Δx that corresponds to 80 fluid cells on the panel and a Δt that corresponds to a CFL–number of 7. We can read off that 5 time steps are needed to advance the shock by Δx.

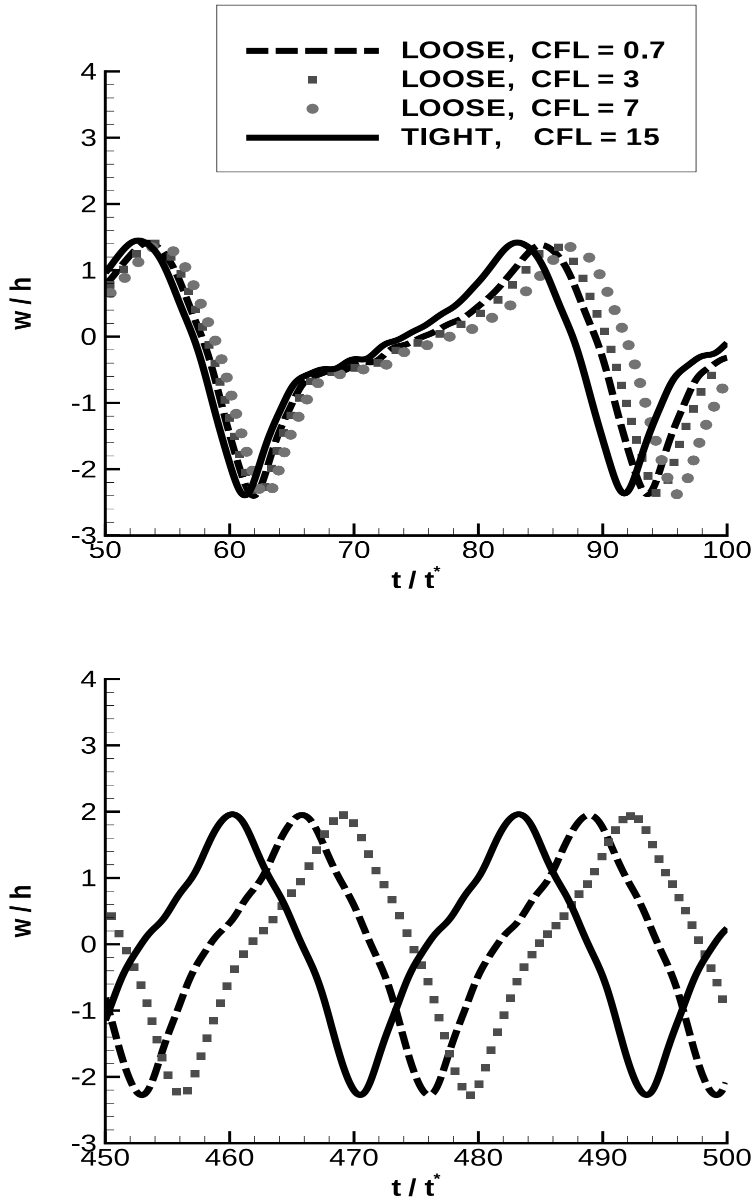

Figure 6.8: The loose and the tight coupling via Newton–iteration were run with different CFL number for the transonic flutter case at $M_\infty = 1$. The panel mid–point deflection is shown for the initial transient in the upper picture and in the lower picture we see a time interval at which the limit cycle oscillation has been reached. The results with the tight coupling for CFL < 15 cannot be distinguished from the one shown with CFL=15. The loose coupling with CFL=7 failed at an earlier time step and is thus not seen in the lower picture.

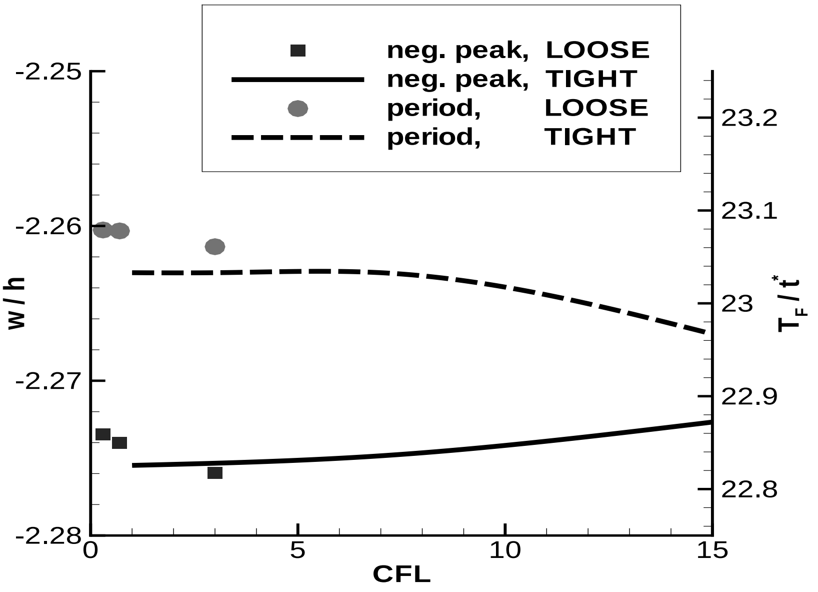

Figure 6.9: $M_\infty = 1$; the convergence with respect to Δt is shown, comparing the loose and the tight coupling via Newton–iteration. The observed quantities are those specifying the limit cycle oscillation. These are the negative peak of the panel mid–point oscillation and the flutter periode.

Convergence in Δt

The mid–point deflections of Fig. 6.12 were obtained with the staggered scheme and different CFL numbers. Below CFL=0.7 the solution does not change anymore. A convergence in the time–accurate solution from CFL=40 to CFL=0.7 is clearly visible. Details on the chosen threshold are given in the comments of the figure. In Fig. 6.13 the convergence in flutter period T_F and the flutter amplitude are shown. But even the rather coarse time resolution of 27 time steps per flutter period, which corresponds to CFL=40, delivered acceptable results and did not interfere with the performance of the algorithm. At this CFL–number the calculations took 2–3 Newton–iterations in the fluid, each with 15 GMRes iterations.

So far we have used only the staggered scheme in this flutter case. In Fig. 6.15 we see that the tightly coupled solutions converge faster with respect to Δt, and that in the limit the same result is obtained as with the staggered coupling. The tightly coupled solutions shown, were obtained with the Newton–iteration, and the FPI brought exactly the same solutions.

6.2.3 Supersonic flutter near the stability boundary

We show another supersonic flutter case for an aluminium panel with $h_{rel} = 0.004537$ and $\mu = 0.1$, $\lambda = 21$ and $M_\infty = 1.1$. This case is situated just above the stability boundary. We compare the loose and the tight coupling at various Δt in the same manner as above,

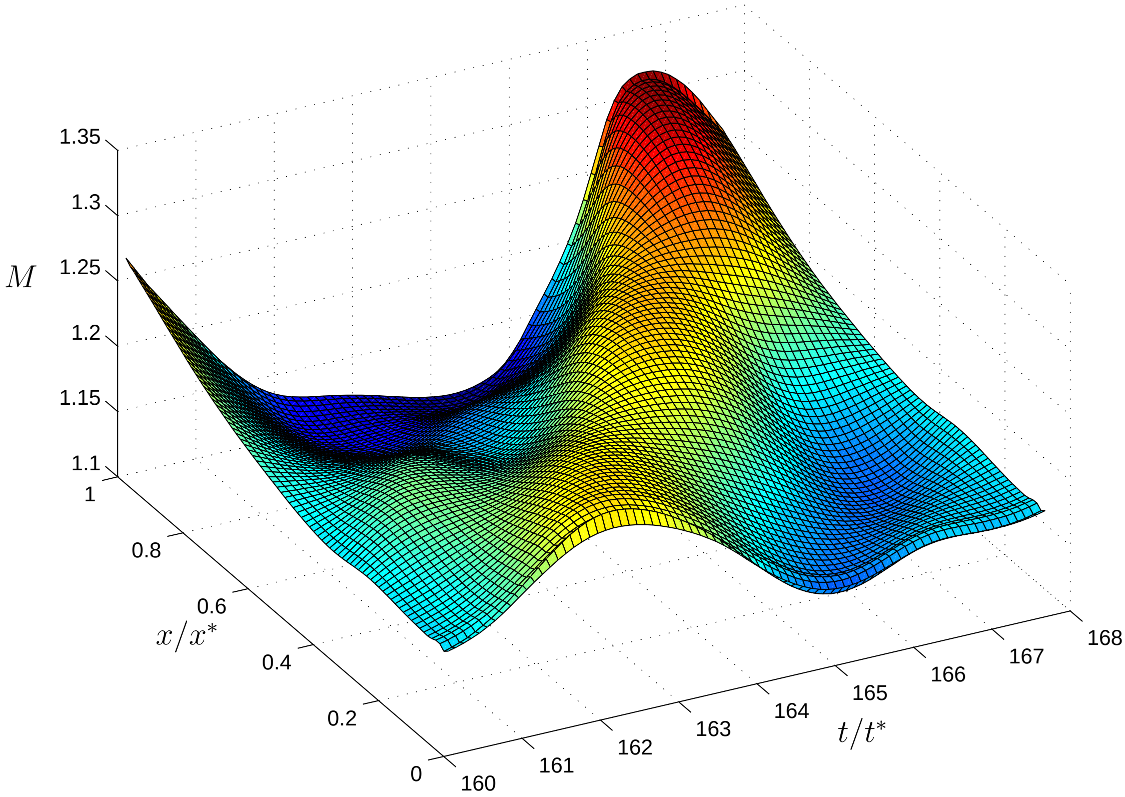

Figure 6.10: $M_\infty = 1.2$; the evolution of the Mach number along the panel in the supersonic flutter case is shown over a full period of the limit cycle oscillation.

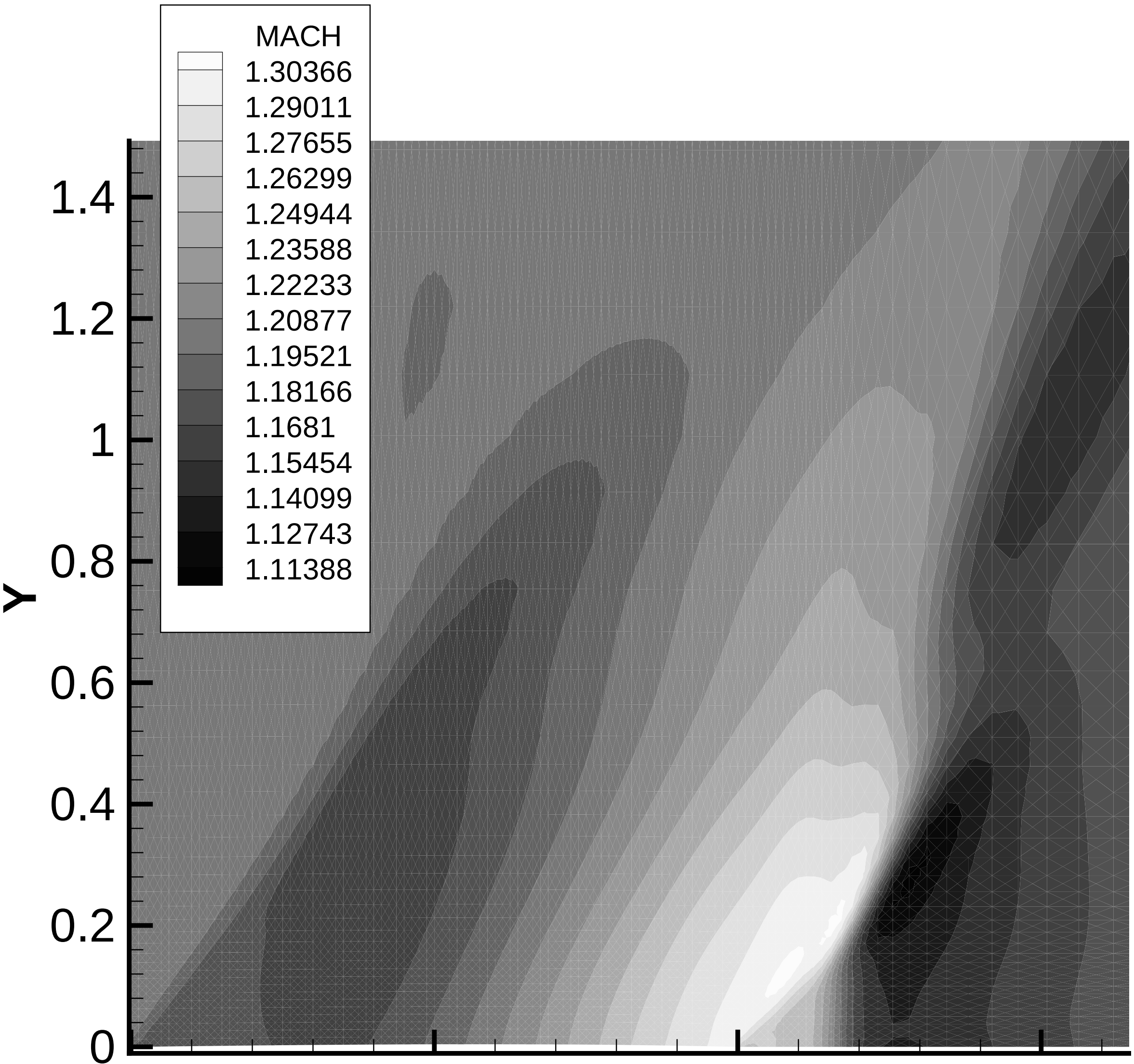

Figure 6.11: $M_\infty = 1.2$; the instantanious Mach number distribution above the panel is shown. The panel is simply supported at $x = 0$ and $x = 1$. The calculation was made with CFL = 40.

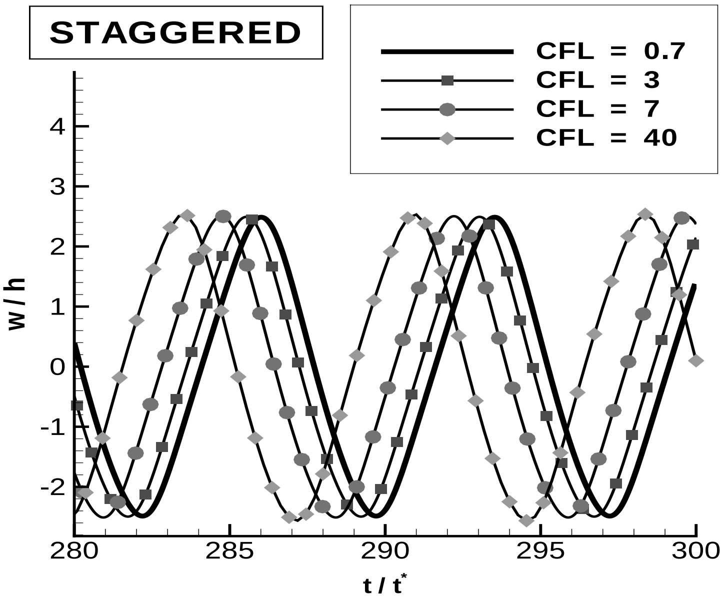

Figure 6.12: $M_\infty = 1.2$; the panel mid–point deflection, calculated with the staggered scheme and various CFL numbers is shown. Below CFL = 0.7 the solutions do not change. Here, CFL = 40 $\iff$ $27\,\Delta t \approx T_F$. As residual threshold we chose $\alpha_{nl}^F = 10^{-6}$, $\varepsilon_l^F = 10^{-3}$, which took 2–3 Newton iterations, each with 15 GMRes iterations

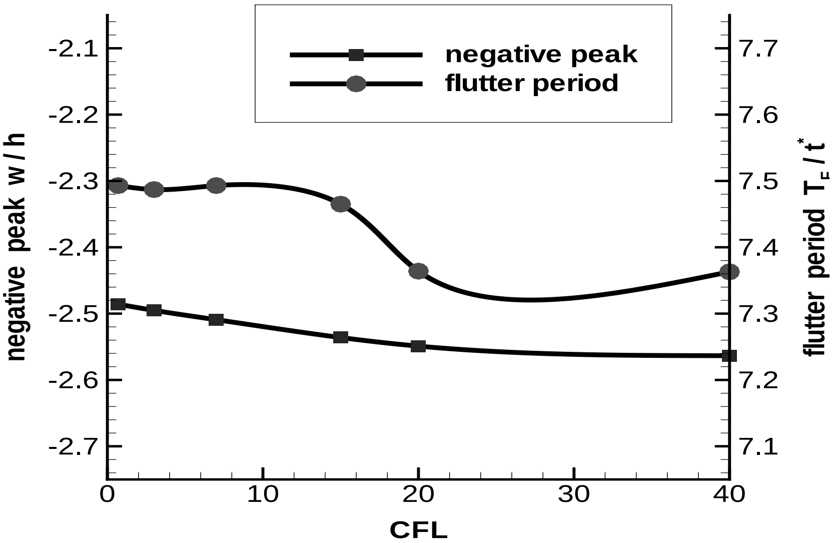

Figure 6.13: $M_\infty = 1.2$; the convergence of the staggered scheme in the quantities characterizing the limit cycle is shown.

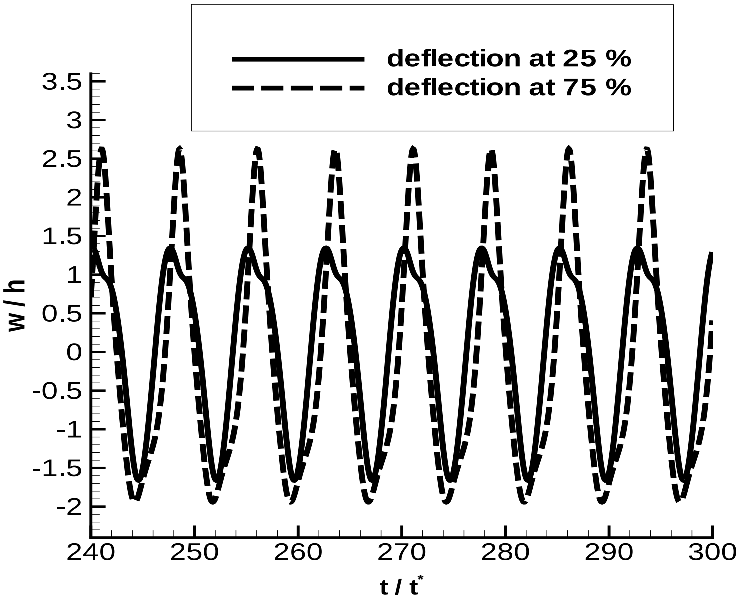

Figure 6.14: $M_\infty = 1.2$; the panel deflection at 25% and 75% chord from the staggered calculation with CFL = 0.7 is shown.

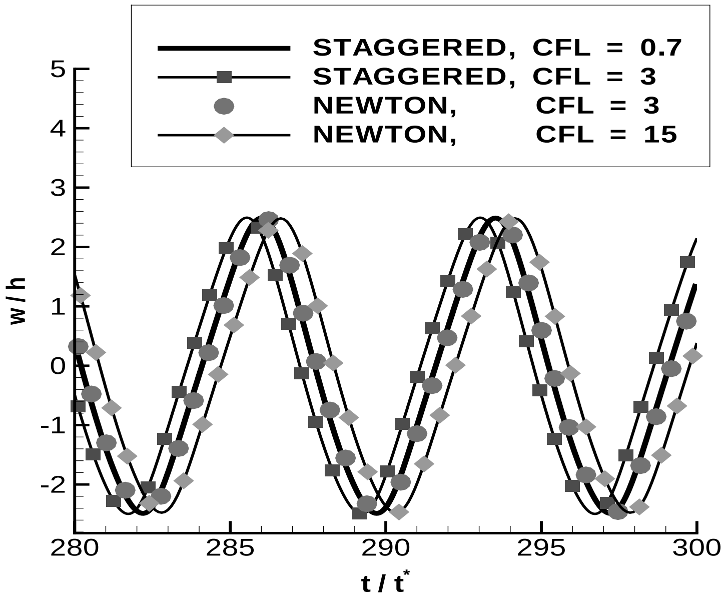

Figure 6.15: $M_\infty = 1.2$; a comparison of the tight coupling with Newton–iteration and the staggered coupling is shown. We see that the solution obtained with tight coupling and CFL = 3 coincides with the one obtained with the staggered coupling and CFL = 0.7. Compared with these solutions, the tightly coupled solution at CFL = 15 and the staggered solution at CFL = 3 deviate by roughly the same amount. As expected, the tight coupling converges faster with respect to Δt. The tight coupling iterarting with FPI brought exactly the same results as the Newton–iteration.

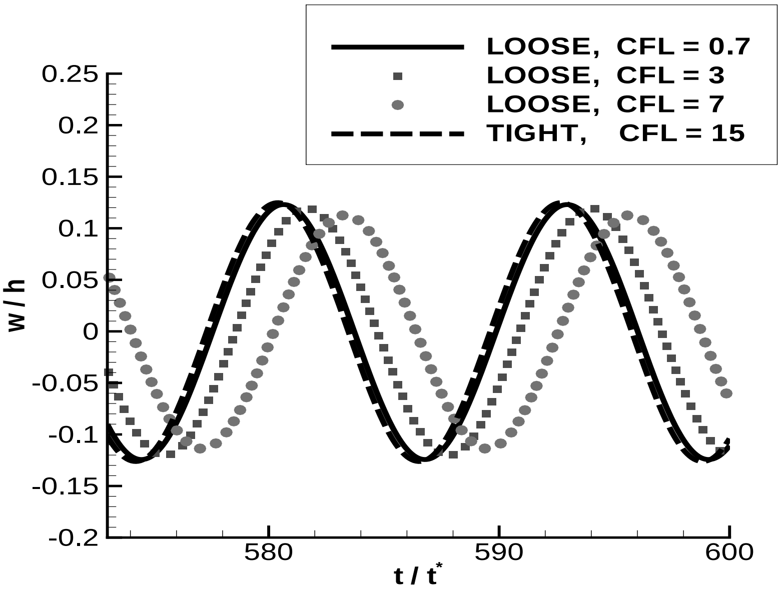

Figure 6.16: $M_\infty = 1.1$; the panel mid–point deflection obtained for various CFL–numbers with the loose coupling and the tight coupling via Newton–iteration. Results for the tight coupling with smaller CFL are not shown, since they reproduce the result obtained with CFL = 15.

looking at the panel deflections in Fig. 6.16 and at the convergence in the amplitude. The behaviour is as before, but quantitatively this case is more drastic, since the amplitudes vary by 10% when reducing the CFL number for the loose coupling from 7 to 0.7. At CFL = 7 the negative deflection peak is $w/h = -0.114$, whereas for CFL = 0.7 it is $w/h = -0.124$. The tight coupling via Newton–iteration is practically converged at CFL = 15. The loose coupling failed at that CFL number.

6.3 Convergence of tight coupling algorithms

In this section we compare the convergence properties of the implemented tight coupling algorithms. One such algorithm is a *fixed point iteration* (FPI), see Sec. 4.3, which has also been implemented by other authors [33], [46]. The second algorithm is the *matrix-free Newton-GMRes* applied at each time step to the coupled set of discrete fluid–structure equations, see Sec. 5.3, which has been newly developed in the course of this thesis. The performance of the two algorithms is compared by considering the convergence history in each time step. As initial guess for both algorithms we take a loose coupling step, which additionally quantifies the improvements of the tight coupling over the loose coupling. The behaviour of the two algorithms is seen to depend on the parameters of the aeroelastic problem, and we find that the FPI works quite well for supersonic flutter cases, but not very satisfactory in transonic flutter cases. The Newton–iteration is seen to be more robust. We look again at the supersonic flutter case from

Sec. 6.2.2, at the transonic flutter case from Sec. 6.2.1 and at another transonic flutter case at $M_\infty = 0.95$.

Note again, as discussed in Sec. 5.4, that we expect to observe a drop in the structural residual of the tightly coupled equations, since in the initial guess another residual was reduced, namely the one corresponding to the loose coupling. On the other hand, the initial guess reduced the right residual in the fluid, but using the wrong structural deflection. Thus, a stagnation in the fluid residual can be accepted.

The computing times were not strictly compared. One can say that the two algorithms take roughly the same computing times, and that in the transonic flutter cases, where the FPI took more iteration steps, its computing times were higher than the ones needed when employing the Newton–iteration.

6.3.1 Supersonic flutter

This is the case with $M_\infty = 1.2$ from Sec. 6.2.2. It was seen to be numerically less challenging than the transonic flutter cases and CFL–numbers of up to 40 produced rather good results.

In Fig. 6.17 the convergence histories in the structural residual at two different CFL–numbers are shown. For each time step, the residual of the initial guess and the ones obtained after each iteration are indicated by symbols. The symbols are connected by lines, in particular connecting the last residual obtained in a time step with the residual of the initial guess from the following time step. If this line departs from the lowest residual value of a time step, then we know that the residual was actually diminished in this time step.

The FPI converges faster than the Newton–iteration in most time steps. This is very obvious at CFL = 15 in the lower picture of Fig. 6.17. But at CFL = 3, in the upper picture, at certain time steps the FPI fails to reach the convergence criterion within the assigned maximum number of 3 FPI–loops. This situation repeats regularly throughout the computation. Compare further the comments of the figures.

6.3.2 Transonic flutter at $M_\infty = 0.95$

An aluminium panel with $h_{rel} = 0.002$ and a flow with $M_\infty = 0.95$ and $\mu = 0.1$, $\lambda = 2900$ constitute this flutter case. A large amplitude in the panel mid–point deflection with a negative peak of $w \approx -6.5h$, a positive peak of $w \approx 7h$ and a moving shock on the panel characterize the limit cycle. Computations were run with CFL = 7 and the Newton–iteration is seen to be clearly superior to the FPI.

To get an overview of the coupling iterations performed in each time step, we first show the residual histories over 2000 time steps in Fig. 6.18 and Fig. 6.19. A closer look in Fig. 6.20 reveals what actually happens. Typically, we can observe a very regular performance of the Newton–iteration in contrast to the FPI. The Newton–iteration reduces the structural residual in one step by about two orders of magnitudes, over the whole range of 2000 time steps shown in Fig. 6.18. The FPI very often takes several iterations

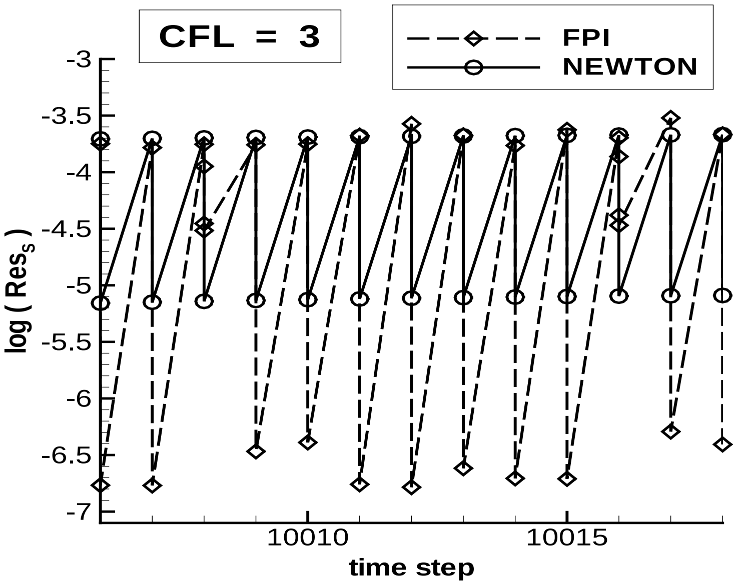

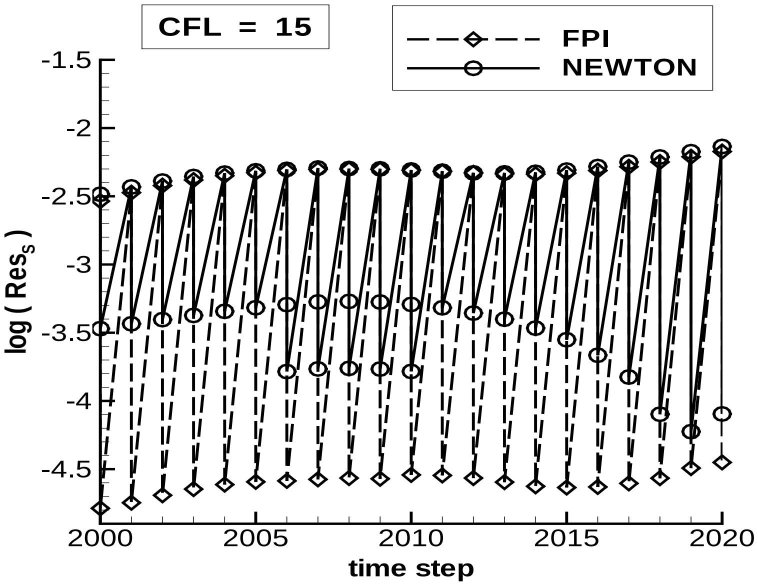

Figure 6.17: Convergence histories in the tightly coupled structural equations for the flutter case at $M_\infty = 1.2$, with CFL = 3 and CFL = 15. For CFL = 3 the Newton–iteration reaches the threshold $\overline{\alpha}^S = 10^{-5}$ or $\overline{\varepsilon}^S = 10^{-1}$ with one iteration, whereas the FPI reduces in many time steps the residual much better but regularly fails to reach the threshold within the assigned 3 iterations. This picture is very representative for the complete computation. At CFL =15 the FPI is better than the Newton–iteration, throughout the computation. The problems seen with CFL = 3 are not present here for the FPI; occasionally the Newton–iteration needs two iterations, as in the picture, to reach the threshold $\overline{\alpha}^S = 5 \cdot 10^{-4}$ or $\overline{\varepsilon}^S = 10^{-1}$.

or fails to reach the convergence criterion in the assigned maximum number of 3 fluid–structure–loops. This behaviour can be observed for selected time steps in the upper picture of Fig. 6.20. In particular, we see in this picture, that the residual of the FPI increases in time step 3204, which can be noted since the dotted line, that connects time step 3204 and 3205, does not leave from the lowest residual value obtained in time step 3204.

The convergence histories in the fluid are depicted in Fig. 6.19. As discussed before, a stagnation of this residual can be accepted, and actually a stagnation of the fluid residual can be observed in the close up view in the bottom picture of Fig. 6.20. The most important step seems to be, to obtain a good residual value in the initial guess. As we see, this inital residual varies by orders of magnitude, due to convergence problems in the separate fluid solver. This is not satisfactory. But this seemed not to have an adverse effect on the obtained results, as all the results presented are reconfirmed by calculations with lower time step sizes.

Varying the residual threshold

Here we demonstrate that the choice $\overline{\alpha}^S = 5 \cdot 10^{-4}$, which corresponds to $\overline{\varepsilon}^S = 0.1$, suffices. We use a tight coupling with the Newton–iteration. The largest CFL number, at which the calculation terminates successfully, is 15. With CFL = 18 the algorithm failed. The CFL number was varied between 3 and 15 and there is almost no variation in the solution; also the residual threshold for the coupled equations in the Newton–iteration was lowered down to $\overline{\alpha}^S = 5 \cdot 10^{-6}$ without any notable effect. In the upper picture of Fig. 6.21, no differences in the solutions can be noted and only an enlargement in the lower picture, reveals that there are differences at all.

6.3.3 Transonic flutter at $M_\infty = 1$

In this transonic flutter case, that was already discussed in Sec. 6.2.1, we can make the same observations as in the case just discussed with $M_\infty = 0.95$. Fig. 6.22 shows the convergence histories in the tightly coupled structural residual that are representative for the full computation. We chose CFL = 7 and CFL = 3, and we see again that the FPI often fails to converge and that the Newton–iteration converges regularly with one iteration step.

6.4 Bifurcations depending on coupling schemes

As seen in Sec. 6.2 and 6.3, the coupling schemes have different convergence properties. The effect of these on the aeroelastic solutions is presented in this section. Usually the stability characteristics of the aeroelastic system are exposed in a stability chart by identifying bifurcations of the aeroelastic system in parameter space. The classical parameter space in our context is the $M_\infty\lambda$–space introduced in Sec. 2.4. In each of the following two experiments we keep the inflow Mach–number M_∞ fixed and vary the nondimensional

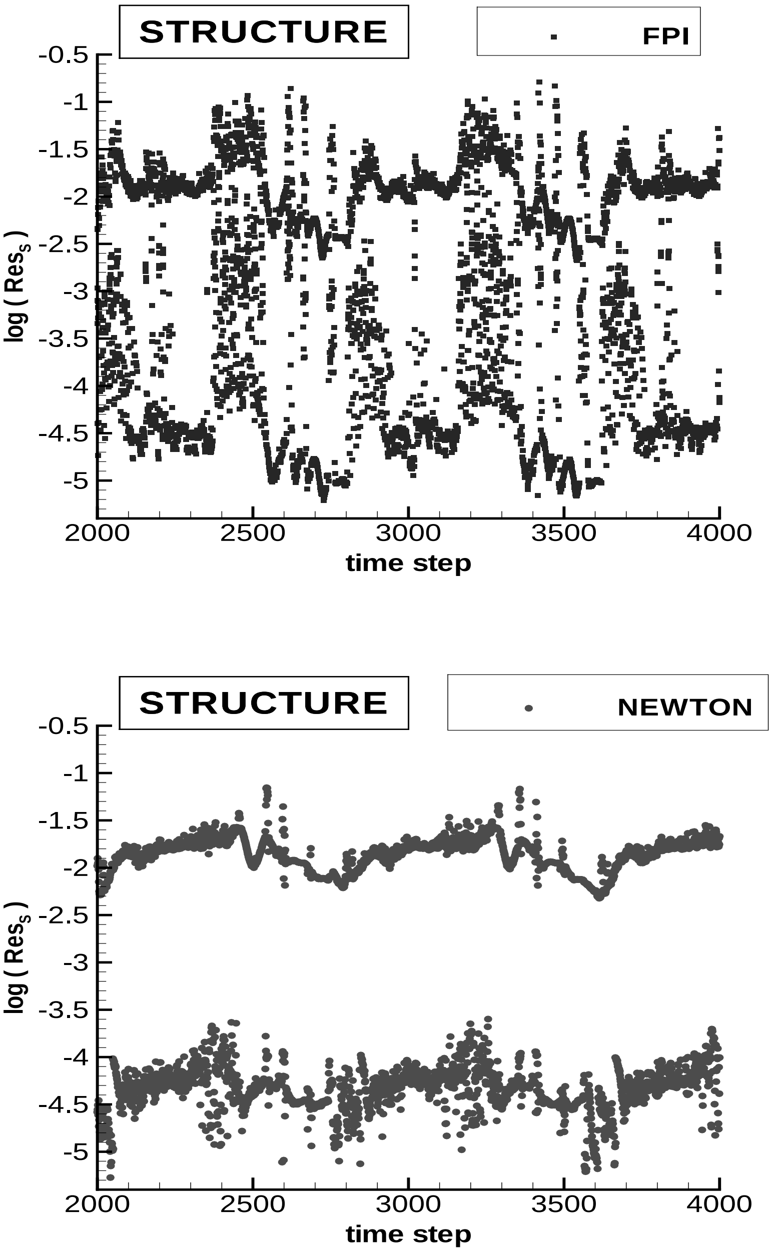

Figure 6.18: Global view of the residual histories in the structure, over 2000 time steps, for the transonic flutter case at $M_\infty = 0.95$. The computations were run with CFL = 7 and the very regular convergence of the Newton–iteration can be observed, in contrast to the FPI. A typical enlargement is given in the upper picture of Fig. 6.20, where the details of the convergence histories can be seen.

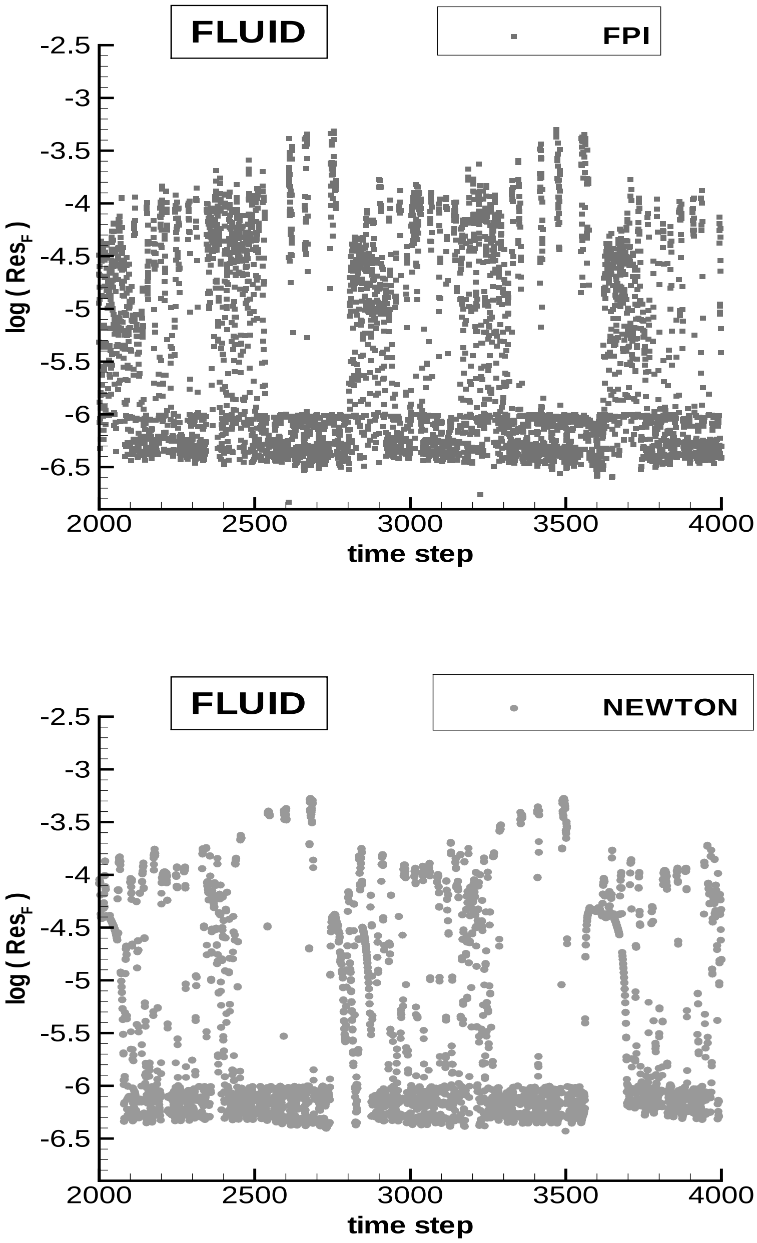

Figure 6.19: Global view of the residual histories in the fluid, over 2000 time steps, for the transonic flutter case at $M_\infty = 0.95$. It can only be interpreted with the typical enlargement given in the lower picture of Fig. 6.20 (CFL = 7).

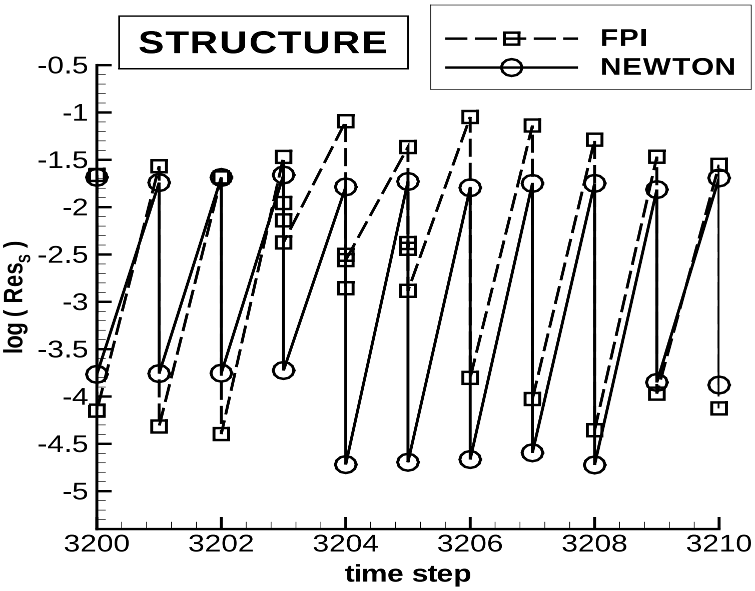

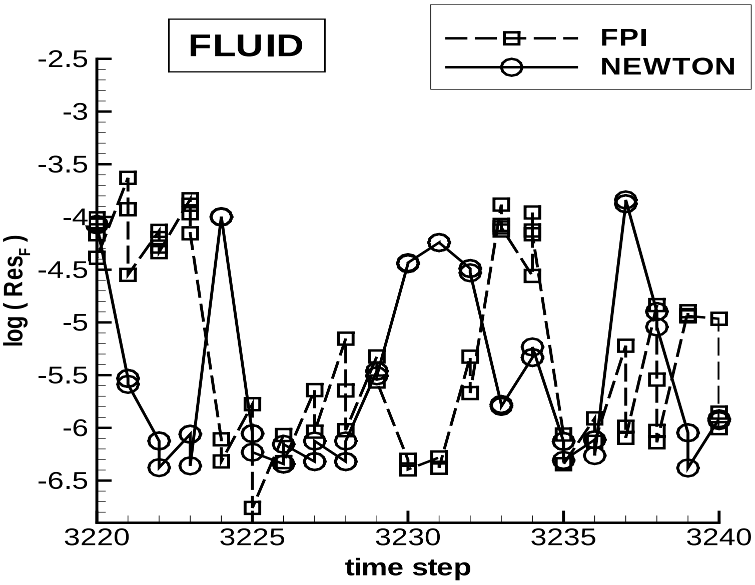

Figure 6.20: $M_\infty = 0.95$; an enlarged view of Fig. 6.18 and Fig. 6.19 is shown, revealing the superiority of the Newton–iteration over the FPI, as red off from the structural residual histories. In the history of the fluid residual we see the expected stagnation in each time step. Further, the variations in orders of magnitude in the residual of the initial guess can be observed, which is not satisfactory (CFL = 7).

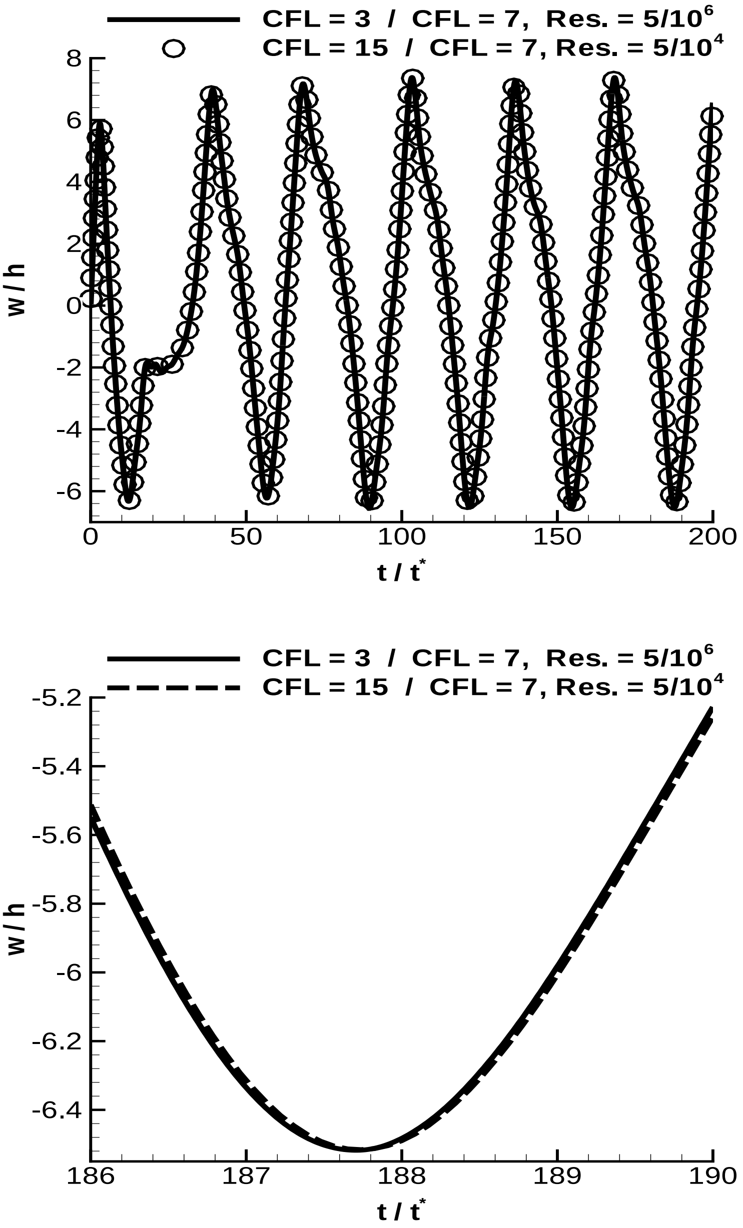

Figure 6.21: $M_\infty = 0.95$; we see results of four computations with different CFL numbers and different residual thrshold $\overline{\alpha}^S$. The results cannot be distingished in the upper picture and only an enlargement in the lower picture makes differences visible. Since the results using CFL=3, $\overline{\alpha}^S = 5 \cdot 10^{-4}$ and CFL=7, $\overline{\alpha}^S = 5 \cdot 10^{-6}$ cannnot be distinguished, they are represented by one line, as is also the case with results obtained with CFL=15, $\overline{\alpha}^S = 5 \cdot 10^{-4}$ and CFL=7, $\overline{\alpha}^S = 5 \cdot 10^{-4}$.

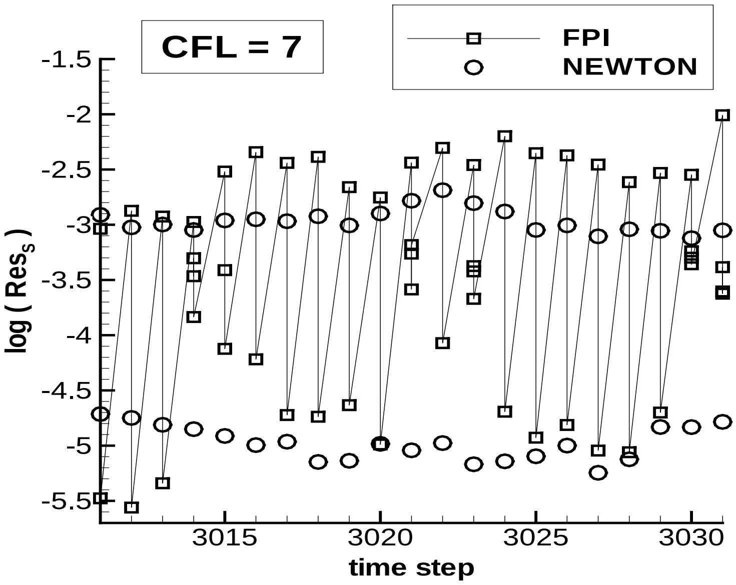

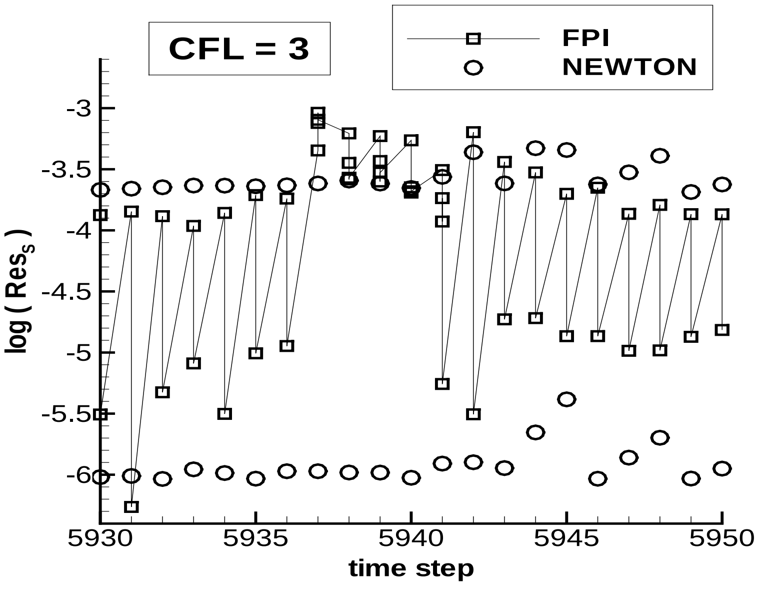

Figure 6.22: Convergence histories in the tightly coupled structural equations for the flutter case at $M_\infty = 1$, with CFL = 7 and CFL = 3. In both cases we have $\overline{\varepsilon}^S = 0.1$ which corresponds with CFL = 7 to $\overline{\alpha}^S = 10^{-4}$ and with CFL = 3 to $\overline{\alpha}^S = 2 \cdot 10^{-5}$.

dynamic pressure λ in ranges where a bifurcation was detected. Here, the bifurcations are qualitative changes in the solution from divergence to flutter and will be shown to occur at different λ for different coupling schemes. In the case of Sec. 6.4.2 the bifurcation point varies in λ by roughly 10%, depending on the coupling scheme. These results are independent of the chosen time step size, since all results were reconfirmed with lower Δt. Unfortunately, a definite reference solution is not available. But looking at the results of sections Sec. 6.2 and 6.3, we know the improvements of the tight coupling over other coupling schemes and further, the superiority of the Newton–iteration over the FPI in transonic flutter cases. These observations are particularly relevant for the experiments in this section, since here we look at flutter cases with the same or similar data.

6.4.1 A bifurcation at $M_\infty = 1$

Here we keep the inflow Mach number constant at $M_\infty = 1$, and vary the nondimensional dynamic pressure in the range $160 \leq \lambda \leq 180$, where the aeroelastic behaviour changes from divergence to flutter. Depending on the coupling scheme, this change occurs at different λ. Note that in Sec. 6.2.1 we were clearly in the flutter region with $\lambda = 260$. Here we chose the reasonable CFL number of 7 and the loose coupling and the tight coupling schemes with FPI and Newton–iteration to perform computations at $\lambda = 160, 170, 180$. All schemes predicted divergence at $\lambda = 160$ and flutter at $\lambda = 180$, see Fig. 6.23 and Fig. 6.25. At $\lambda = 170$ the FPI failed to terminate the computation successfully, so that it was run with CFL = 3. It predicted flutter. The Newton–iteration predicted flutter as–well, using CFL = 7. The loose coupling predicted divergence at CFL = 7, and the loose coupling was also run at CFL = 3, predicting divergence again. The results are shown in Fig. 6.24.

6.4.2 A bifurcation at $M_\infty = 0.95$

Again, the inflow Mach number is held constant, now at $M_\infty = 0.95$, and the nondimensional dynamic pressure is varied in the range $2500 \leq \lambda \leq 2900$. I.e. the case studied in Sec. 6.3.2 is included. The qualitative results obtained are shown in the table of Fig. 6.26 and reveal a variation of the bifurcation point depending on the coupling scheme by roughly 10% in dynamic pressure. All the results obtained with CFL = 7 were reconfirmed with CFL = 3. In particular the bad performance of the FPI compared to the Newton–iteration, which was observed in the convergence histories of Sec. 6.3.2, seems to have a rather big influence on the location of the bifurcation point. Note also, that using a tight coupling scheme, the change to flutter is detected at $\lambda = 2500$ in [27].

6.5 Stability chart

The stability boundary of a simply supported aluminium panel of thickness $h_{rel} = 0.004537$ and with a mass ratio between fluid and structure of $\mu = 0.1$ was determined in [14] and reconfirmed in [33], as we have seen in Fig. 2.3. Here we compare the stability

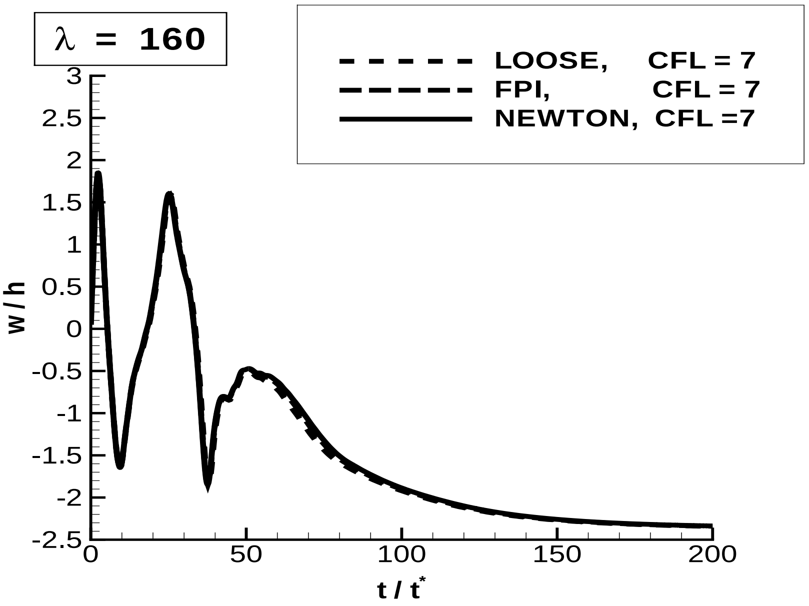

Figure 6.23: $M_\infty = 1$, $\lambda = 160$: All schemes predict divergence, the mid–point deflections almost coincide.

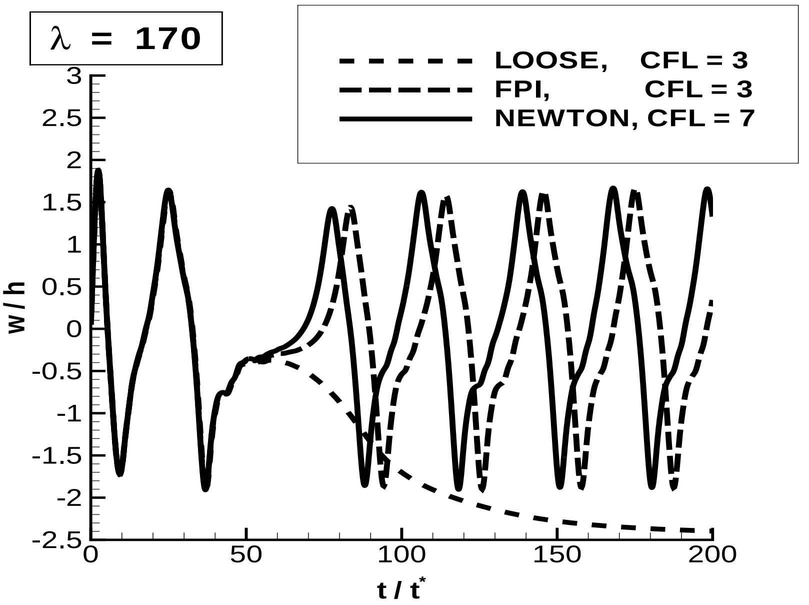

Figure 6.24: $M_\infty = 1$, $\lambda = 170$: Only the loose coupling predicts divergence. The FPI and the Newton–iteration predict flutter. The calculation of the FPI failed with CFL = 7, but terminated successfully with CFL = 3. The loose coupling brought divergence at CFL = 7, as–well.

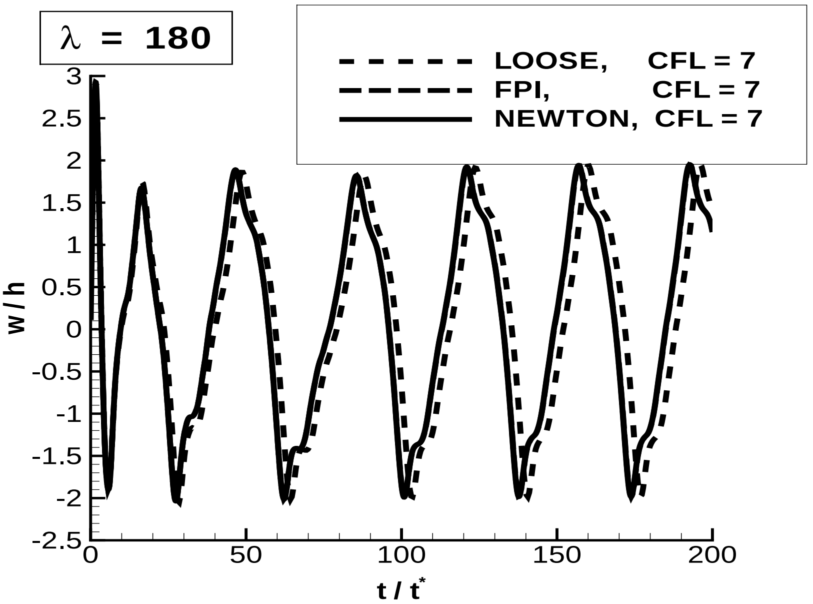

Figure 6.25: $M_\infty = 1,\ \lambda = 180$: All schemes predict flutter, the mid–point deflections of the FPI and the Newton–iteration coincide, the loose coupling gets very close to it.

λ	A CFL = 7	B (St.) CFL = 0.7	B (St.) CFL = 7	C (FPI) CFL = 7	C (Newton) CFL = 7
2900	F	F	F	F	F
2800	D	F	D	F	F
2700	D	D	D	D	F
2600	D	D	D	D	F
2500	D	D	D	D	D

Figure 6.26: Bifurcation at $M_\infty = 0.95$ with respect to λ from divergence (D) to flutter (F) using different coupling schemes.

boundary of Davis and Bendiksen [14] with the one we have obtained with the tight coupling via Newton–iteration at a CFL–number of 7. The stability boundary is produced in $M_\infty\lambda$–space. At a given Mach number the deflection amplitudes of the calculated long time behaviours increase gradually with λ. We have chosen an amplitude value in the panel mid–point deflection of $w = 0.01\,h$ to mark the stability boundary; for smaller amplitudes the system was defined as stable, for larger amplitudes as unstable. For $M_\infty < 1$ and $M_\infty > 1$ the change from stable to unstable is rather sharp. Here the amplitudes of the results just above the stability boundary show divergence or flutter amplitudes of $w \approx 0.1\,h$. Just below the stability boundary, at a dimensionless time of 1000, the panel deflections are either by orders of magnitudes below $w \approx 0.01\,h$ or around $w \approx 0.01\,h$ with the clear tendency to fall. At $M_\infty = 1$ the increase in amplitudes is rather slow; the development at $M_\infty = 1$ over a larger λ–range is discussed below, see Fig. 6.28.

These observations show that the panel deflections are rather small in the neighbourhood of the stability boundary. Our algorithm performed perfectly well in this situation, reducing *all* residuals as required. The results coincide very well with [14] for $M_\infty < 1.15$. The difference at $M_\infty = 1$ may be due to the amplitude value that defines the stability boundary, as discussed above. Small divergence amplitudes at $M_\infty = 1$ for very small λ are also obtained in [33]. The mismatch for $M_\infty > 1.15$ cannot be addressed to this fact. The main difference between our code and the codes of [14] and [33] is the way in which numerical diffusion is implemented in the fluid code. Both [14] and [33] use a central differencing in space with artificial viscosity added, whereas we use flux differencing with reconstruction and limitation. But no significant shocks can be observed in the calculations around the stability boundary, so that these differences in the discretization should not have an effect. A difference attributed to the coupling scheme should be tested by implementing the coupling of [14] in our code.

In Fig. 6.28 the development at $M_\infty = 1$ is visualized. The amplitudes in the long time behaviour are plotted against λ, showing a sudden change from positively deflected divergence to negatively deflected divergence at $\lambda \approx 30$ and a change from divergence to flutter at $\lambda \approx 165$. The latter result was obtained in Sect. 6.4.1.

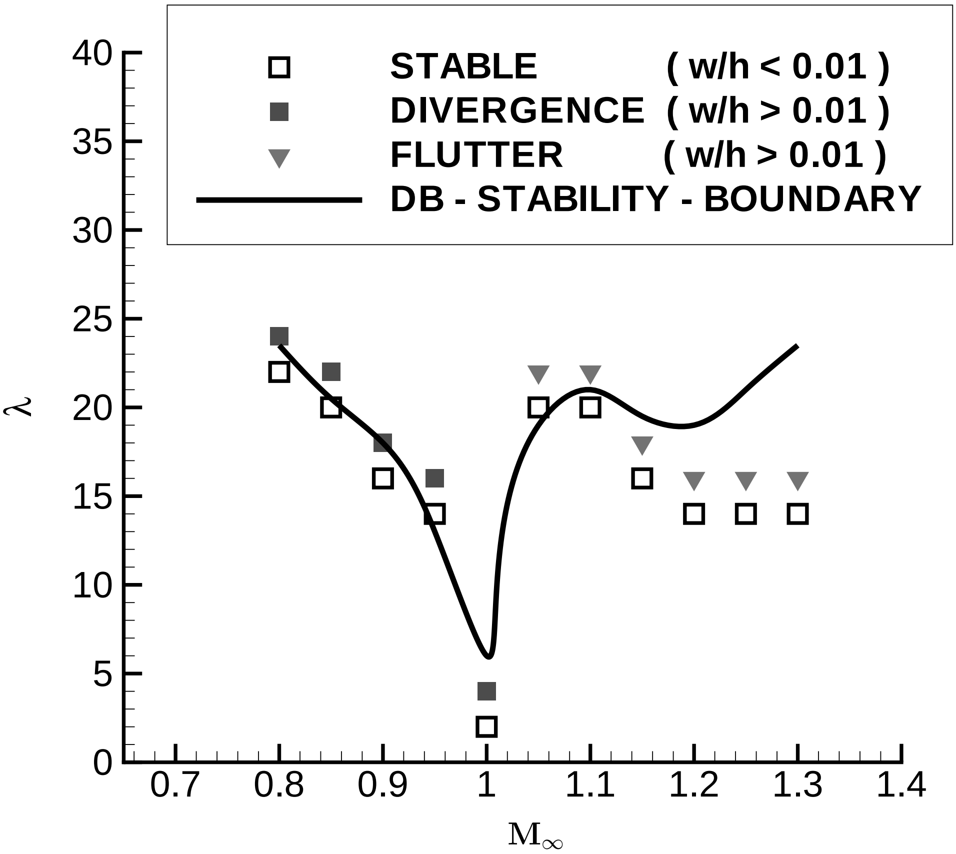

Figure 6.27: The stability boundary of a simply supported aluminium panel with $h_{rel} = 0.004537$ and $\mu = 0.1$, compared with the stability–boundary obtained by Davis and Bendiksen [14].

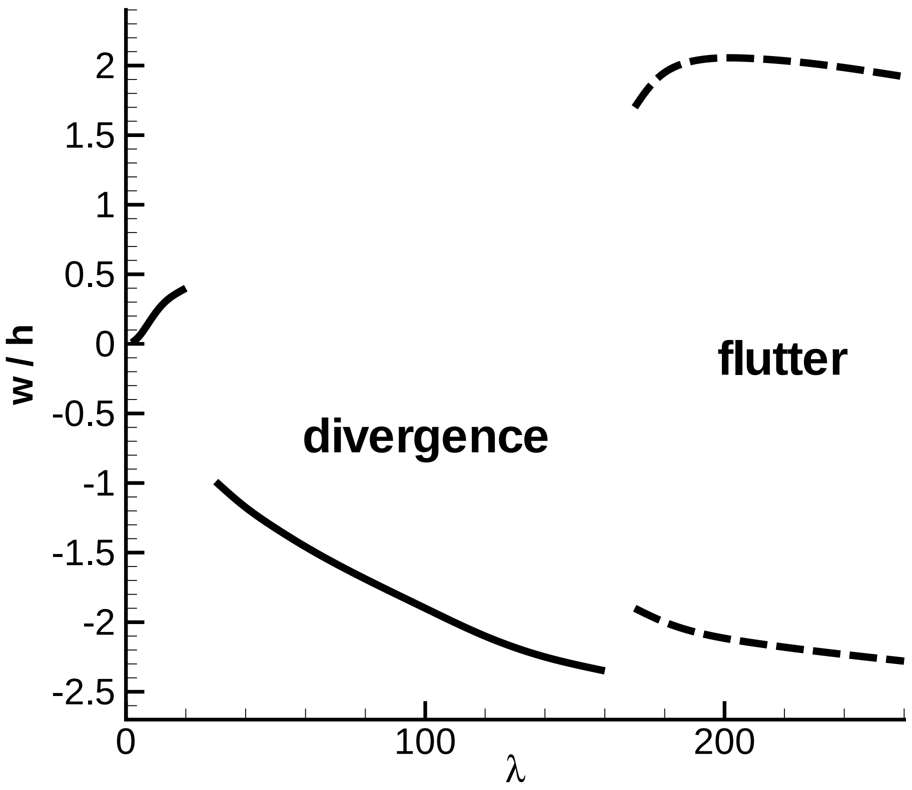

Figure 6.28: A simply supported aluminium panel with $h_{rel} = 0.004537$, $\mu = 0.1$; the development of the panel mid–point amplitudes are shown at $M_\infty = 1$ for various λ. First we have the slight increase in divergence amplitude, which defines the location of the stability boundary of Fig. 6.27 at $M_\infty = 1$. Then the divergence amplitude suddenly changes its sign and remains negative up to $\lambda = 160$. From $\lambda = 170$ on, flutter solutions occur. From the corresponding limit cycles, the negative and positive deflection peaks are plotted with dashed lines.

Chapter 7

Summary

In order to investigate analytical and numerical issues appearing in aeroelastic problems with structural nonlinearities and transonic flow nonlinearities, we have considered the panel flutter problem.

A first step concerning the question of well–posedness for the initial boundary value problem describing panel flutter was made by proving a uniqueness theorem. The prescribed initial boundary value problem uses a purely Lagrangian viewpoint in the fluid; a generalization of the uniqueness result to the case of an Arbitrary–Lagrangian–Eulerian formulation in the fluid is still missing, also an existence result is not available yet.

Further, numerical schemes for aeroelasticity were implemented for the panel flutter problem. In particular, a new coupling algorithm achieving a tight coupling was proposed and successfully implemented. It applies a matrix–free Newton–GMRes iteration to the discrete fluid–structure system. The implementation can be considered as a base version, which may be optimized and improved in various ways. We have compared this tight coupling with other coupling strategies, in particular with a fixed–point–iteration that also aims to achieve a tight coupling. We can observe the superiority of the tight coupling schemes over simpler coupling schemes for large time step sizes; the tight coupling schemes seem to allow higher time step sizes also from a stability point of view. Nevertheless the loose or staggered coupling schemes yield very good results in many cases. The superiority of the Newton–iteration over the fixed–point–iteration to achieve a tight coupling was found for transonic flutter cases, which also resulted in improved computing times. An example that showed a severe influence of the coupling scheme was the determination of a bifurcation from divergence to flutter in the transonic regime, where the bifurcation point varied by 10% in terms of dynamic pressure, depending on the coupling scheme. A notable difference between the tight coupling via Newton–iteration and the tight coupling via fixed–point–iteration can also be observed in this example. A deviation from a stability boundary of the literature is observed in the supersonic regime. These deviations should be investigated further by implementing the coupling scheme used in the literature.

Further improvements should be made in the unsteady fluid code. Together with an optimized version of the tight coupling via Newton–iteration more complex applications may be tackled.

Bibliography

[1] W. Aftosmis, D. Gaitonde, T. Tavares, *Behaviour of Linear Reconstruction Techniques on Unstructured Meshes.* AIAA-Journal, Vol. 33, No. 11, pg. 2038-2049 (1995)

[2] J.J. Alonso, A. Jameson, *Fully–Implicit Time–Marching Aeroelastic Solutions.* AIAA-Paper 94-0056 (1994)

[3] W. Anderson, J. Thomas, C. Rumsey, *Extension and Applications of Flux-Vector Splitting to Unsteady Calculations on Dynamic Meshes.* AIAA-Paper 87-1152 (1987)

[4] H. Ashley, *Role of Shocks in the "Sub-Transonic" Flutter Phenomenon.* Journal of Aircraft, Vol. 17, No. 3 (1980)

[5] O. Axelsson, V. Barker, *Finite Element Solution of Boundary Value Problems.* Academic Press (1984)

[6] R. Bisplinghoff, H. Ashley, *Principles of Aeroelasticity.* Dover Publications (1975)

[7] O. Bendiksen, *A new approach to Computational Aeroelasticity.* AIAA-Paper 91-0939-CP (1991)

[8] O. Bendiksen, G. Davis, *Nonlinear Travelling Wave Flutter of Panels in Transonic Flow.* AIAA-Paper (1995)

[9] R. Blevins, *Flow–Induced Vibrations.* Van Nostrand Reinhold (1990)

[10] Blom, *A Monolithical Fluid–Structure–Interaction Algorithm Applied to the Piston Problem.* Comput. Methods Appl. Mech. Engrg., 167, pg. 369-391 (1998)

[11] J. R. Cebral, R. Löhner, *Conservative Load Projection and Tracking for Fluid-Structure Problems.* AIAA-Journal, Vol. 35, No. 4, pg. 678-692(1997)

[12] R. Dautray, J.-L. Lions, *Mathematical Analysis and Numerical Methods for Science and Technology, Vol. II.* Springer-Verlag, Berlin (1988)

[13] R. Dautray, J.-L. Lions, *Mathematical Analysis and Numerical Methods for Science and Technology, Vol. V.* Springer-Verlag, Berlin (1988).

[14] G. Davis, O. Bendiksen, *Transonic Panel Flutter.* AIAA-Paper 93-1476 (1993)

[15] E.H. Dowell, *Nonlinear Oscillations of a Fluttering Plate.* AIAA Journal, Vol. 4, No. 7, pg. 1267-1275 (1966)

[16] E.H. Dowell, *Nonlinear Oscillations of a Fluttering Plate II.* AIAA Journal, Vol. 5, No. 10, pg. 1856-1862 (1967)

[17] E.H. Dowell, *Panel Flutter: A Review of the Aeroelastic Stability of Plates and Shells.* AIAA Journal, Vol. 8, No. 3, pg. 385-399 (1970)

[18] E.H. Dowell, *Aeroelasticity of Plates and Shells.* Noordhoff International Publishing (1975)

[19] E.H. Dowell, *Flutter of a Buckled Plate as an Example of Chaotic Motion of a Deterministic Autonomous System.* Journal of Sound and Vibration, 85,3, pg. 333-344 (1982)

[20] J. Edwards, J. Malone, *Current Status of Computational Methods for Transonic Unsteady Aerodynamics and Aeroelastic Applications.* AGARD CP-507: Transonic Unsteady Aerodynamics and Aeroelasticity, Paper No.1, 1991

[21] V. Elling, *Numerical simulation of gas flow in moving domains.* Diplom Thesis, RWTH Aachen (2000)

[22] C. Farhat, P. Geuzaine, C. Grandmont, *The Discrete Geometric Conservation Law and the Nonlinear Stability of ALE Schemes for the Solution of Flow Problems on Moving Grids.* Journal of Computational Physics, 2001, 174, pg. 669-694

[23] C. Farhat, M. Lesoinne, *On the Accuracy, Stability, and Performance of the Three-Dimensional Nonlinear Transient Aeroelastic Problems by Partitioned Procedures.* AIAA-Paper 96-1388-CP, 1996

[24] C. Farhat, M. Lesoinne, P. LeTallec, *Load and motion transfer algorithms for fluid/structure interaction problems with non—matching discrete interfaces: Momentum and energy conservation, optimal discretization and application to aeroelasticity.* Comput. Methods Appl. Mech. Engrg., 157, pg. 95-114 (1998)

[25] Y.C Fung, *An Introduction to the Theory of Aeroelasticity.* Dover Publications (1969)

[26] E. Godlewski, P.-A. Raviart, *Numerical Approximation of Hyperbolic Systems of Conservation Laws.* Springer Verlag, 1996

[27] R.E. Gordnier, M.R. Visbal, *Development of a three-dimensional viscous aeroelastic solver for nonlinear panel flutter.* AIAA-Paper 2000-2337 (2000)

[28] M. E. Gurtin, *An Introduction to Continuum Mechanics.* Academic Press, 1981.

[29] G. Guruswamy, *Coupled Finite–Difference/Finite–Element Approach for Wing–Body Aeroelasticity.* AIAA-Paper 92-4680-CP (1992)

[30] Hairer, Norsett, Wanner, *Solving Ordinary Differential Equations.* Springer, 1993

[31] C. Hirsch, *Numerical Computation of internal and external flows, Volume II.* Wiley & Sons (1995)

[32] I. Hlaváček, J. Nečas, *Mathematical Theory of Elastic and Elastico-Plastic Bodies: An Introduction.* Elsevier, Amsterdam (1981)

[33] J. Hurka, *Numerische Untersuchung zur Aeroelastik duenner Platten.* Ph.D. Thesis, RWTH Aachen (2002)

[34] J. Hurka, J. Ballmann. *Elastic Panels in Transonic Flow*, AIAA-Paper 2001-2722 (2001)

[35] K. Isogai, *Transonic Dip Mechanism of Flutter of a Sweptback Wing: Part II.* AIAA-Journal, Vol.19, No.9, pg. 1240-1242 (1981)

[36] Ilan Kroo, *http://aero.stanford.edu/StdAtm.html*

[37] H. Kuchling, *Taschenbuch der Physik.* 16. Auflage, Fachbuchverlag Leipzig (1999)

[38] M. Lesoinne, C. Farhat, *Geometric conservation laws for flow problems with moving boundaries, and their impact on aeroelastic computaions.* Comput. Methods Appl. Mech. Engrg., 134, pg. 71-80 (1996)

[39] J.-L. Lions, *Quelques méthodes de résolution des problèmes aux limites non linéaires.* Dunod, Paris (1969)

[40] J.-L. Lions, E. Magenes, *Non-Homogeneous Boundary Value Problems and Applications, Vol. I.* Springer-Verlag, Berlin (1972)

[41] B. Lee, S. Price, Y. Wong, *Nonlinear aeroelastic analysis of airfoils: bifurcation and chaos.* Progress in Aerospace Sciences, 35, pg. 205-334 (1999)

[42] R. LeVeque, *Numerical Methods for Conservation Laws.* Birkhäuser Verlag (1992)

[43] H. Luo, J. Baum, R. Löhner, *A Fast, Matrix-free Implicit Method for Compressible Flow on Unstructured Grids.* Journal of Computational Physics, 146, pg. 664-690 (1998)

[44] H. Luo, J. Baum, R. Löhner, *An Accurate, Fast, Matrix-Free Implicit Method for Computing Unsteady Flows on Unstructured Grids.* AIAA-Paper 99-0937 (1999)

[45] R. Massjung, *Uniqueness Results for Aeroelasticity – Lagrangian Approach.* Internal Report 172, IGPM, RWTH Aachen (1999)

[46] S. Morton, R. Melville, M. Visbal, *Accuracy and Coupling Issues of Aeroelastic Navier–Stokes Solutions on Deforming Meshes.* Journal of Aircraft, Vol. 35, No.5, pg. 798-805 (1998)

[47] N.F. Morozov, *Nonlinear vibrations of thin plates with allowance for rotational inertia.* Soviet Math., Vol.8, pg. 1137-1141 (1967)

[48] A. Nayfeh, D. Mook, *Nonlinear Oscillations.* John Wiley & Son, New York (1979)

[49] S. Osher, F. Solomon, *Upwind difference schemes for hyperbolic systems of conservation laws.* Math. Comput., 38, pg. 339-374 (1982)

[50] G.V. Parkinson, J.D. Smith, *The square prism as an aeroelastic non-linear oscillator.* Quart. Journ. Mech. and Applied Math., Vol. 17, pg. 225-239 (1964)

[51] L.E. Payne, H.F. Weinberger, *On Korn's Inequality.* Arch. Rational Mech. Anal., 8, pg. 89-98 (1961)

[52] S. Piperno, *Explicit/Implicit Fluid/Structure Staggered Procedures with a Structural Predictor and Fluid Subcycling for 2D Inviscid Aeroelastic Simulations.* Int. J. Num. Meth. Fluids, 25, pg. 1207-1226 (1997)

[53] N. Qin, D. Ludlow, S. Shaw, *A matrix-free preconditioned Newton/GMRES method for unsteady Navier-Stokes solutions.* Int. J. Num. Meth. Fluids, 33, pg. 223-248 (2000)

[54] Y. Saad, *Iterative methods for sparse linear systems.* PWS Publishing, New York (1996)

[55] P. Secchi, A. Valli, *A free boundary problem for compressible viscous fluids.* Journal für reine und angewandte Mathematik, 341, pg. 1-31 (1983)

[56] R. Selvam, M. Visbal, S. Morton, *Computation of Nonlinear Viscous Panel Flutter Using a Fully-Implicit Aeroelastic Solver.* AIAA-paper 98-1844 (1998)

[57] J. Steger, R. Warming, *Flux Vector Splitting of the Inviscid Gasdynamic Equations with Application to Finite-Difference Methods.* Journal of Computational Physics, 40 pg. 263-293 (1981)

[58] J. Serrin, *Mathematical Principles of classical fluid dynamics.* In: S.Flügge (ed.): Handbuch der Physik, Vol. VIII/1, pg. 125-263, Springer-Verlag, Berlin (1959)

[59] J. Serrin, *On the Uniqueness of Compressible Fluid Motions.* Arch. Rat. Mech. Ana., 3, pg. 271-288 (1959)

[60] J.T.M. Thompson, *Instabilities and Catastrophes in Science and Engineering.* Springer–Verlag (1982)

[61] K. Thompson, *Time Dependent Boundary Conditions for Hyperbolic Systems.* Journal of Computational Physics, 68, pg. 1-24 (1987)

[62] H. Tijdeman, R. Seebass, *Transonic Flow Past Oscillating Airfoils.* Ann. Rev. Fluid Mechanics, 12, pg. 181-222 (1980)

[63] B. Van Leer, *Flux Vector Splitting for the Euler equations.* Proc. of the eighth International Conference on Numerical Methods in Fluid Dynamics, pg. 507-512 (1982)

[64] V. Venkatakrishnan, *Covergence to Steady State Solutions of the Euler Equations on Unstructured Grids with Limiters.* Journal of Computational Physics, 118, pg. 120-130 (1995)

[65] V. Venkatakrishnan, D. Mavriplis, *Implicit solvers for unstructured meshes.* Journal of Computational Physics, 105 pg. 83-91 (1993)

[66] V. Venkatakrishnan, D. Mavriplis, *Implicit Method for the Computation of Unsteady Flows on Unstructured Grids.* Journal of Computational Physics, 127, pg. 380-397 (1996)

[67] W. Walter, *Analysis II.* Springer-Verlag, Berlin (1990)

[68] J. Wloka, *Partielle Differentialgleichungen.* Teubner, Stuttgart (1982)

Lebenslauf

Name		Ralf Massjung
Geburtsdatum		29. November 1969
Geburtsort		Rastatt
Schulbildung	1976 – 1980	Karl–Schule Rastatt
	1980 – 1989	Ludwig–Wilhelm–Gymnasium Rastatt
Wehrdienst	1989 – 1990	in Roth (Nürnberg) und Karlsruhe
Studium	1990 – 1993	Studium der Mathematik mit Nebenfach Strömungsmechanik an der Universität Karlsruhe
	1993 – 1994	Studienaufenthalt am University College Cork (Irland)
	1994 – 1996	Fortsetzung des Studiums in Karlsruhe und Abschluss mit dem Diplom
Beruf	seit 1/97	Wissenschaftlicher Angestellter am Institut für Geometrie und Praktische Mathematik an der RWTH Aachen und Mitarbeiter im Sonderforschungsbereich Strömungsbeeinflussung und Strömungs–Struktur–Wechselwirkung an Tragflügeln